UNIVERSITÀ DEGLI STUDI DI MILANO

Scuola di Dottorato in Fisica, Astrofisica e Fisica Applicata
Dipartimento di Fisica

Corso di Dottorato in Fisica, Astrofisica e Fisica Applicata
Ciclo XXVIII

Theoretical physics modeling of neurological problems

Settore Scientifico Disciplinare FIS/02

Supervisore Interno: Professor Guido TIANA

Supervisore Esterno: Professor Massimo VERGASSOLA

Tesi di Dottorato di:
Alessandro SANZENI

Contents

Overview of the thesis

In this thesis we approach different problems in neurobiology using methods from theoretical physics.

The first topic that we studied is the mechanoelectrical transduction at the basis of touch sensation, i.e. the process by which a mechanical signal conveyed during touch is transformed into an electric signal that is then interpreted by other parts of the neural system. A general introduction to the subject is given in Chapter 1. In Chapter 2 we investigate how the neural response is generated in the worm *C. elegans* and propose a channel gating mechanism to explain the activation of touch receptor neurons by mechanical stimuli. In Chapter 3 we analyze the mechanics of the worm body, this is a preliminary work aiming to describe how the mechanics of the body affects the neural response.

Our ability of orient ourself and navigate in space is based on a specific neural system. In the last forty years, this system has been extensively characterized in rats, where the activity of different types of neurons has been found to be correlated with the spatial position of the animal. Grid cells in the rat entorhinal cortex are part of this "neural map" of space; they form regular triangular lattices whose geometrical properties have a modular distribution among the population of neurons. In Chapter 4 we show that some of the features observed in the system may be explained by assuming that grid cells provide an efficient representation of space. Importantly, our model predicts a testable scaling relation connecting the number of neurons within a module and the spatial period of the associated grids.

The last problem discussed in this thesis concerns the neurodegenerative Parkinson's disease. Limb tremor and other debilitating symptoms caused by the disease are currently treated by administering drugs and by fixed-frequency deep brain stimulation. The latter interferes directly with the brain dynamics by delivering electrical impulses to neurons in the subthalamic nucleus. In Chapter 5 we develop a theory to describe the onset of anomalous oscillations in the neural activity of the basal ganglia that are at the origin of the characteristic tremor. On the basis of the results obtained from the model, we propose a new feedback-controlled stimulation procedure and show that it could outperform the standard protocol.

Some of the ideas contained in this thesis have appeared in the following publications:

- Eastwood, A. L., Sanzeni, A., Petzold, B. C., Park, S.-J., Vergassola, M., Pruitt, B. L., & Goodman, M. B. (2015). *Tissue mechanics govern the rapidly adapting and symmetrical response to touch.* Proceedings of the National Academy of Sciences of the United States of America, 112(50), E6955-63.

- Sanzeni, A., Celani, A., Tiana, G. & Vergassola (2016). *Theory of feedback controlled brain stimulations for Parkinson's disease.* Physica A: Statistical Mechanics and its Applications 441, 121-130.

CHAPTER 1

Introduction

1.1 Brief overview of mechanosensation

Touch is based on somatosensory neurons, which turn the mechanical energy of external stimuli on the skin into electrical signals within the nervous system. Mammalian skin is invaded by a multitude of mechanoreceptor neurons that vary in their sensitivity to mechanical loads, their response dynamics, and their structure [1, 2]. This diversification makes touch sensation robust, but it also complicates efforts to decipher its biophysical, genetic, and molecular basis. In particular, little is currently understood about how external mechanical loads activate sensory mechanoelectrical transduction (MeT) channels in any animal. Even less is known about how skin transmits and filters mechanical energy. In this thesis we approach these problems through theoretical modeling in the case of the nematode Caenorhabditis elegans. The main motivation of our choice is the availability of quantitative measurements, indeed the experimental advantages of the nematode *C. elegans* (see next Section) made this animal a model organism to investigate touch sensation.

Adult *C. elegans* hermaphrodites are known to have five classes of mechanoreceptor neurons that exhibit surprisingly similar patterns of rapidly adapting and nearly symmetrical on and off MeT currents in response to applied mechanical loads (see [3] for a review). Genetic dissection of these mechanoreceptors showed that no single class of proteins is responsible for forming sensory MeT channels. Moreover the same kinds of ion channels also contribute to touch and pain sensation in Drosophila larvae. Collectively, these observations suggest that the properties of rapid adaptation and symmetrical on and off responses are not uniquely linked to a single class of channel proteins.

The earliest insight into mechanisms of rapid adaptation and symmetrical on and off response emerged from works on the mammalian Pacinian corpuscle in the 1960s [4, 5, 6] which linked their responses to the onion-like lamellar capsule that encases its specialized nerve ending. This multi-layered accessory structure has been shown to function as a mechanical filter and to be crucial for the response dynamics. However, rapidly adapting and symmetrical on and off MeT currents are found in other mammalian sensory afferents such as those thought to innervate Meissner's corpuscles and hair follicles [3, 7]. Moreover, all of the mechanoreceptor neurons in *C. elegans* lack accessory structures analogous to the Pacinian corpuscle, yet they still exhibit rapid adaptation and symmetric response. Thus, rapidly adapting and symmetric neural responses do not hinge on specialized accessory structures.

In Chapter 2 we propose a gating mechanism to explain how the response to mechanical stimulations in these receptors are generated. Even though the mechanism will be explained using a specific structure, the derived equations correspond to different molecular realizations, hence the model provides a general mechanism for mechanosensation that could be applied to different types of receptors. The key elements of the model are: the viscoelastic interaction between ionic channels and the surrounding tissues; the possibility to describe the tissues containing the receptors as thin shells. These two ingredients provide adaptation and symmetry in the response, respectively. A crucial role in the model is played by the mechanics of the worm body; in Chapter 3 we describe ongoing work aiming to investigate this aspect in more detail. Specifically, we derive a model describing the worm body mechanics and discuss how it could be used to investigate the fine structure of the channel gating mechanism.

The theory described here has been tested experimentally using measurements obtained on *C. elegans* by the group of professor Miriam Goodman at Stanford University. In the remaining part of this Chapter we describe the properties of *C. elegans* touch receptor neurons and the experimental setup that has been used to analyze them.

1.2 Touch sensation in *C. elegans*

In response to mechanical stimulations *C. elegans* show an escape behavior that is easy to characterize and to assay: if the worm is touched in the anterior part, it will start moving backward, if it is touched in the posterior part it will speed up in the forward direction. This behavior, combined with standard molecular biology tools that are well developed in this system, made *C. elegans* a model organism to study touch sensation. Using this behavioral assay, molecular biologists have characterized the mechanosensitive neurons founding the six touch receptor neurons (TRN), sketched in Fig. 1.1, responsible for the response to gentle touch (forces in the order of 10μN). In what follows we concentrate on these TRN because we have access to experimental results obtained on them (see next Section). For completeness we mention that there are other 16 mechanoreceptor neurons in the worm Hermaphrodite of which two are related to response to harsh stimuli (forces in the order of 100μN) whilst the remaining neurons are localized close to the mouth of the animal and are used for foraging. In the male nematode there are additional 46 MRNs, all of which are needed for mating [8].

By looking at mutants and at the behavioral assay the complex of proteins forming ionic channels (called MEC-4) has been discovered together with a series of proteins providing accessory structure [9]. The ionic channels have been extensively characterized; they are sodium channels which are ameliorate sensitive [9], the distance between the channels follows a log-normal distribution [10] with mean inter-channel distance of $1.39\,\mu$m (see Fig. 1.1). As we said before, the activation mechanism of the channels and the role played by the accessory proteins are not understood yet. Understanding this process is the main goal of the first part of this thesis.

1.3 Experimental results on *C. elegans* touch response

In this Section we describe the experimental setup and a series of experimental results that has been used to investigate the response generated by touch receptor neurons to mechanical stimulations.

In the experiments the worm is glued on a plate and it is stimulated mechanically on its top surface with a glass microsphere attached to the tip of an electronically controlled cantilever (see Fig. 1.2). The device can operate either in displacement clamp, delivering defined displacements while measuring applied force, or in force clamp, delivering defined forces while measuring applied displacement. During the stimulations the mem-

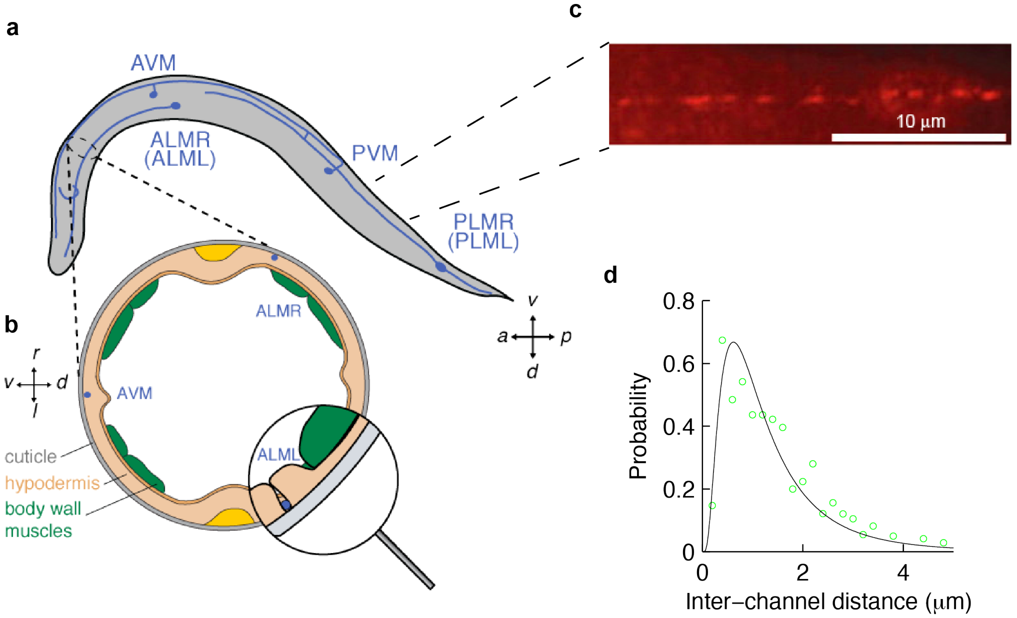

Figure 1.1: Structure of touch receptor neurons in *C. elegans***.** Schematic of *C. elegans* touch receptor neurons along the longitudinal direction (**a**) and in a cross-section (**b**) of the worm body. Each neurons has several ionic channels that are gated by mechanical stimuli. (**c**) Positions of the channels visualized through indirect immunofluorescence [10]. (**d**) Experimental inter-channel distance from [10] (green circles) are well described by a log-normal distribution $P(x) = 1/x\sigma\sqrt{2\pi}\,\exp\left(-(\log x - \mu)^2/2\sigma^2\right)$, with $\mu = 0.06\mu$m and $\sigma = 0.74\mu$m (black line). The mean and standard deviation of the inter-channel distance are 1.39 μm and 1.40 μm.

brane current in touch receptor neurons is measured in parallel under conditions that maintained the integrity of the entire touch-sensing system. This setup allows to deliver very well controlled stimuli and, at the same time, measure the neural response.

As shown in Fig. 1.2, mechanical loads evoke rapidly adapting on and off MeT current. In order to understand how adaptation is affected by variations in the mechanics of the worm's body, worms have been prepared using two dissection procedures. The first procedure releases a portion of the gonad and intestines to reduce internal pressure and ease successful dissection of neuronal cell bodies [11, 12]. The second dissection procedure better preserves the physical integrity of the nematode by exposing only the neuronal cell body of interest [13, 14, 15]. The first dissection procedure results in worms that are approximately 60 to 90% softer than those prepared with the second procedure, which had an average effective stiffness of 1.1 ± 0.3 N/m. Because of this observation we refer to the worms prepared by the first procedure as "soft" and those prepared by the second procedure as "stiff". Regardless of the dissection method and body stiffness or of whether stimuli were delivered under force clamp or displacement clamp, MeT currents adapt rapidly and activate in response to the application and withdrawal of mechanical loads (Fig. 1.2).

The channel gating mechanism proposed in Chapter 2 is derived starting from these experimental observations; the model is further validated by comparing its predictions with experimental results on the response to different types of mechanical stimuli.

As shown in Fig. 1.2, the stiff mechanical regime shifts the midpoint of Current-Force (I-F) curves to higher forces ($F_h = 3.0\mu$N and 0.38μN for stiff and soft worms, respectively) and also significantly decreases sensitivity to force. (The slopes, F_s, of the fitted I-F curves were 0.21μN and 1.55μN in soft and stiff worms, respectively.) In contrast, the midpoint and slope for Current-Indentation (I-z) curves were indistinguishable between the two mechanical regimes. (The midpoints, z_h, of the fitted functions were 2.4 μm and 2.9 μm in stiff and soft worms, respectively, and the slopes, z_s, were 1.4μm and 1.3μm for soft and stiff worms, respectively.) Thus, MeT current amplitude increases in proportion to body indentation and not the applied force.

In Chapter 3 we show that this fact reflects the structure of the deformation induced in the worm body by mechanical stimulations.

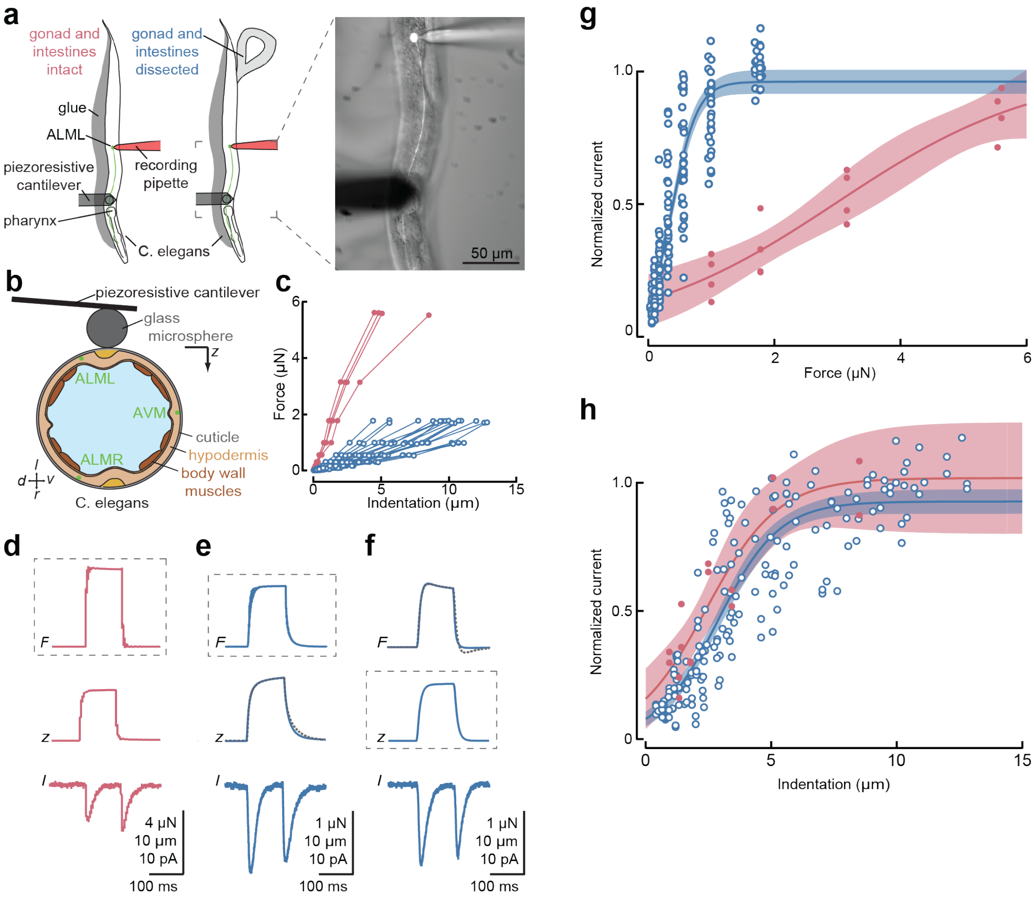

Figure 1.2: MeT current response to mechanical stimuli in *C. elegans***.** (**a**) The experimental preparation and integration with the system for simultaneous feedback-controlled mechanical stimulation and patchclamp recording. Two worm preparations were used: a minimal dissection that exposes only the anterior touch receptor neuron (ALM) cell body (Left), and a preparation that exposes the gonad, intestines, and ALM cell body (Center). A micrograph shows the position of the microcantilever with respect to the ALM cell body (Right). (**b**) Schematic drawing of a cross-section of the worm's body and position of the TRNs with respect to the cuticle, epidermis, and body wall muscle and the microcantilever. (**c**) Curves show the relationship between force and indentation for individual worms, body stiffness depends on the dissection procedure. (**d-f**) Representative force (F), indentation (z), and membrane current (I) traces for recordings in a stiff worm evoked by a force-clamped single-step protocol (**d**) and in a soft worm evoked by a force-clamped (**e**) and displacement-clamped single-step protocol (**f**). (**g**) Peak current increases in proportion to force, but the apparent force dependence differs in soft and stiff worms. (**h**) Peak current increases in proportion to indentation in both soft (blue) and stiff (red) worms. Smooth lines in (**g**) and (**h**) are Boltzmann functions fit to the data; shaded area shows the 95% confidence interval for the fit. Fitting coefficients for force dependence in (**h**) are F_h, the force required for half-maximal activation, and F_s, the slope of the curve, and have the following values: F_h = 0.38 μN and F_s= 2.13 for soft worms; F_h = 3.0 μN and F_s = 1.55 for stiff worms. Fitting coefficients for indentation in (**g**) are z_h, the indentation required for half-maximal activation, and z_s, the slope of the curve, and have the following values: z_h= 2.9 μm and z_s= 1.40 for soft worms; z_h= 2.4 μm and z_s= 1.25 for stiff worms.

CHAPTER 2

A gating mechanism for mechano-electrical transduction channels

In the previous Chapter we described the phenomenology of touch receptor neurons (TRNs) showing that in different types of receptors touch elicits symmetric activation followed by rapid adaptation. In Caenorhabditis elegans, many of the protein partners that form native mechano-electrical transduction (MeT) channels in these and other types of somatosensory neurons have been identified. Yet, the biophysical mechanism driving the response to mechanical stimulation has eluded understanding for decades. In this Chapter we propose a theoretical model that links external loads to activation of MeT channels in *C. elegans* touch receptor neurons. The model reproduces the experimental findings, predicts that the TRNs function as a band-pass mechanical filter, and provides a general mechanism for symmetrical and rapidly adapting MeT channel activation relevant to somatosensory neurons across phyla and submodalities.

2.1 Description of the model

In *C. elegans* the application of mechanical loads to the skin generates time-dependent strain within the viscoelastic tissues that engulf the TRNs. In this Section we introduce a model in which a hypothetical gating element links MeT channels to these viscoelastic tissues. For convenience we refer to the gating element as a filament and note that the role played by this filament could also be fulfilled by interactions between the MeT channel and the phospholipid bilayer. Differential displacements between MeT channels and their filaments result in an elongation of the filaments that is proportional to the velocity of indentation, and such elongation favors channel opening. Once the MeT channels open, the model asserts that elastic and viscous (friction) forces act to return the connected filaments to their relaxed conformation, closing the channels and accounting for rapid adaptation. The dependence of the open probability on the distance between the channels and the stimulus site is treated by a mean-field approximation as discussed below.

2.1.1 Dynamics of the channel-anchor filament

We posit that each MeT channel is connected through an elastic filament to a mechanical unit that we refer to as an “anchor”. Applying a force to the surface of *C. elegans* produces an indentation of depth $\zeta(t)$ and deforms its cuticle, which we treat as a viscoelastic medium (Fig. 2.1a). Given that the cuticle is a thin shell, it follows that the dominant component of the elastic stress arises in the plane orthogonal to the indentation for moderate deformations [16]. For larger deformations, the dominant component of the stress remains localized to the plane locally tangential to the surface of the worm, which changes though as one moves along the surface [17, 18] (Fig. 2.1a). We expect that MeT channels and their anchors be displaced relative to one another as a result of their different viscoelastic properties (Fig. 2.1b). The elastic filaments connecting MeT channels to the anchor elongate, which we hypothesize increases the probability that channels will enter their open (conducting) conformation and result in significant mechanoreceptor currents, as described below.

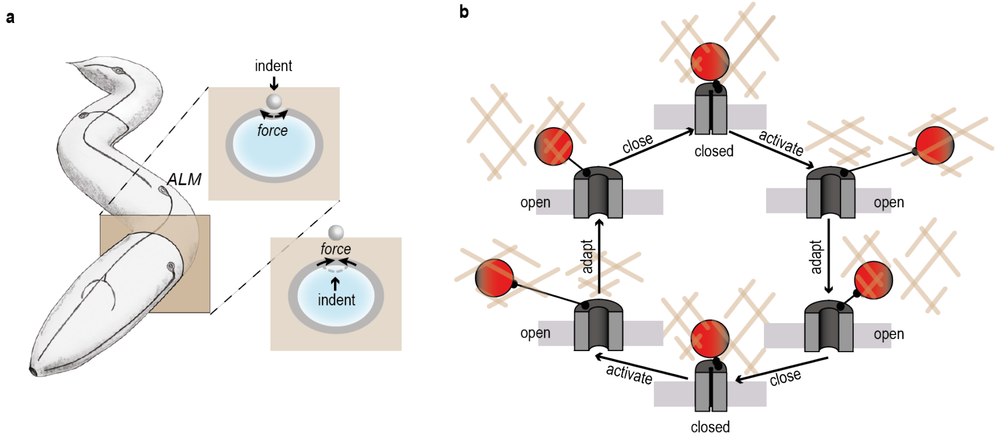

Figure 2.1: Model of ionic channel gating by mechanical stimulations. (**a**) Schematic showing forces orthogonal to the axis of indentation. (**b**) Schematic showing one possible embodiment of the model: an MeT channel linked through an elastic filament to an anchor (red ball) that can move through a viscous extracellular matrix. The system is at rest and the MeT channel is closed in the top and bottom panels. Moving from the top in a clockwise manner: internal forces generated from an external deformation induce a lateral shift between the extracellular matrix and anchor, stretching the filament and activating the channel; viscoelastic forces return the filament to its relaxed conformation, resulting in MeT channel adaptation and then closure; internal forces generated from releasing the external deformation induce a lateral shift in the extracellular matrix and anchor, stretching the filament and activating the channel; finally, viscoelastic forces conclude the cycle symmetrically.

Specifically, we use $\boldsymbol{X}_{c,a}$ to denote the position of the channel and the anchor in the absence of any deformation, $\boldsymbol{x}_{c,a}(t)$ to indicate their respective displacements (which depend on the original positions $\boldsymbol{X}_{c,a}$) and $\boldsymbol{S}(\boldsymbol{X},t)$ to indicate the displacement of a generic point $\boldsymbol{X}$ in the viscoelastic medium in which the anchor is embedded. The anchor is subject to the action of the elastic filament connecting it to the channel. A general expression of the corresponding potential $V(x)$ is

$$V(x) = \frac{k}{2}\,x^2 + \frac{k_4}{4}\,x^4 + \dots\,, \tag{2.1}$$

where $x = x_a - x_c$ is the projection along the direction $\hat{\boldsymbol{n}}$ of the separation between the channel and the anchor, which is assumed to be constant throughout the cycle of stimulation. If the direction were to change rapidly, which will not the case hereafter, a multidimensional description of the dynamics would be required. In the description that follows, only the first term in the expansion of Eqn. 2.1 is sufficient, *i.e.* the spring is Hookean and the elastic force is proportional to the elongation. We have considered nonlinear terms in Eqn. 2.1 and they do not substantially affect the results presented below.

The action of the spring will move the anchor with respect to the viscoelastic medium in which it is embedded. Their relative motion is opposed by a friction force $\mathcal{F}$, which in the simplest approximation takes the form

$$\mathcal{F} = -\gamma \frac{d\,(x_a - S(\boldsymbol{X}', t))}{dt} \simeq -\gamma \frac{d\,(x_a - S(\boldsymbol{X}_a, t))}{dt} \,. \tag{2.2}$$

Here, $\boldsymbol{X}_a + \boldsymbol{x}_a = \boldsymbol{X}' + \boldsymbol{S}(\boldsymbol{X}', t)$, *i.e.* $\boldsymbol{X}'$ is the undeformed position of that point in the viscoelastic medium which is at the current location of the anchor $\boldsymbol{X}_a + \boldsymbol{x}_a(t)$. For the second approximate equality, we assume that the differential displacement between the channel and the anchor is small compared to the typical length scale of variation of S. The order of magnitude of the latter is expected to be similar to the radius of the indenting ball and the thickness of the cuticle, that is micrometers for the situation considered here. The difference in the Eqn. 2.2 above is rewritten as

$$x_a(t) - x_c(t) + x_c(t) - S(X_a, t) \simeq x(t) - \chi(X_a)\zeta(t) \,, \tag{2.3}$$

where $x = x_a - x_c$, the differential displacement $S(X_a, t) - x_c(t)$ is dimensionally proportional to the indentation $\zeta(t)$ and the function $\chi(X_a)$ depends on the position at rest X_a (properly non-dimensionalized). To simplify notation, we omit additional dependencies of χ on fixed parameters such as the size and the shape of the indenting body, the internal pressure of the undeformed worm, viscoelastic parameters, etc., and we suppose for Eqn. 2.4 below that the main component of the time-dependence is well captured by the linear $\zeta(t)$ term.

Effects of inertia are usually negligible in the microscopic molecular world and the overdamped approximation generally holds [19], which entails equating to zero the sum of the forces. By using Eqns. 2.1, 2.2 and 2.3, we thus finally obtain the equation for the elongation $x = x_a - x_c$:

$$\frac{dx}{dt} + \frac{1}{\tau} x = \chi \frac{d\zeta(t)}{dt} \,, \tag{2.4}$$

where $\tau = \gamma/k$. The left-hand side in Eqn. 2.4 describes the action of a spring in parallel with a dashpot, which is known as Kelvin viscoelastic module [20, 21]. This simple module is already sufficient to capture two main features of the experimental data presented before (i.e. symmetry and adaptation). First, an external indentation forces an extension of the filament proportional to $\frac{d\zeta(t)}{dt}$, *i.e.* to the time-derivative of the indentation. A constant indentation will thus fail to extend the filament while an abrupt change in indentation will extend the filament, which will then relax due to the viscoelastic combined action of the spring and the friction term in Eqn. 2.4. Since the opening of the channels is controlled by the extension of the filament (see next section) the model naturally leads to the property of adaptation. Furthermore, when force is applied to the surface of *C. elegans* or relieved, the indentation $\frac{d\zeta(t)}{dt}$ will be reversed and $x(t)$ will change sign, but its modulus will be roughly the same. As we discuss in detail in the next section, that property constitutes the basis for the symmetry in the response to the rapid application and removal of mechanical loads. Finally, we show in Section 2.2 that the simple model Eqn. 2.4 (in conjunction with the dynamics of the channels discussed in the next section) goes beyond qualitative aspects of the response and it does capture main quantitative aspects as well.

2.1.2 Dynamics of MeT channel gating

The purpose of this Section is to develop the relationship between the elongation x in Eqn. 2.4 and the probability that channels occupy open (conducting) states. Single-channel recording shows that the MEC-4-dependent channels responsible for mechanoreceptor currents in touch receptors can occupy closed, fully open, and intermediate or sub-conducting states [22]. We use here one sub-conducting state only, the agreement with experimental data being already excellent and generalizations to multiple states being straightforward. We denote by P_c, P_s and P_o the probabilities for the channel to be in the closed, sub-conductance or open state, respectively; R_{ji} is the transition rate from state j to state i. The dynamics of the conformation of the channel is then given by

$$\begin{cases} \frac{dP_c}{dt} &= -P_c\,R_{cs} + P_s\,R_{sc}\,, \\ \frac{dP_s}{dt} &= P_c\,R_{cs} - P_s\,(R_{sc}+R_{so}) + P_o\,R_{os}\,, \\ \frac{dP_o}{dt} &= P_s\,R_{so} - P_o\,R_{os}\,. \end{cases} \tag{2.5}$$

The standard assumption made on the channels is that they conform to the laws of equilibrium statistical physics, *i.e.* the ratio of two probabilities at equilibrium P_i^{eq} and P_j^{eq} is given by the Boltzmann factor $P_i^{eq}/P_j^{eq} = \exp\left[-\beta\Delta G_{ij}\right]$, where $\Delta G_{ij} = G_i - G_j$ is the free energy difference between the states i and j, $\beta = 1/k_BT$, T is the thermodynamic temperature and k_B is the Boltzmann constant (see, *e.g.*, [19]). It follows that the transition rates satisfy the relations:

$$\frac{R_{cs}}{R_{sc}} = e^{-\beta\Delta G_{sc}}\,, \quad \frac{R_{so}}{R_{os}} = e^{-\beta\Delta G_{os}}\,. \tag{2.6}$$

Finally, we obtain for the equilibrium values of the three probabilities P_c, P_s and P_o:

$$P_s^{eq} = \frac{1}{1+e^{-\beta\Delta G_{os}}+e^{-\beta\Delta G_{cs}}}\,, \quad P_o^{eq} = \frac{1}{1+e^{-\beta\Delta G_{co}}+e^{-\beta\Delta G_{so}}}\,, \tag{2.7}$$

with $P_c^{eq} = 1 - P_o^{eq} - P_s^{eq}$. To gather a better sense of the role of the various parameters upon the predictions, we also developed a simpler model in which only two states were considered, open and closed. The equations governing the two populations are analogous to Eqn. 2.5 and the transition rates respect detailed balance as in Eqn. 2.6.

The currents for the various conformations of the channels are as follows. The current in the closed state is supposed to vanish. The contribution to the total current of the neuron by the channels in the sub-conductance and open states is $I_{s,o} = n_{s,o} i_{s,o}$. Here, $n_{s,o}$ and $i_{s,o}$ are the number of channels and the ionic currents through an individual channel in the sub-conductance and open conformations, respectively. For a population of N identical channels the expected number of elements in the open and sub-conductance states, their variances and cross correlation are

$$\begin{gathered} \langle n_s\rangle = N\,P_s,\;\; \langle n_o\rangle = N\,P_o,\;\; \sigma^2_{n_s} = N\,P_s\,(1-P_s)\,, \\ \sigma^2_{n_o} = N\,P_o\,(1-P_o)\,,\;\; \langle(n_s - \langle n_s\rangle)\,(n_o - \langle n_o\rangle)\rangle = -N\,P_oP_s\,. \end{gathered} \tag{2.8}$$

The expected value and the standard deviation of the current for a neuron with N identical channels are then

$$\begin{aligned} &\langle I\rangle = N\left[i_sP_s + i_oP_o\right]\,, \\ &\sigma_I^2 = N\left[i_s^2P_s\,(1-P_s) + i_o^2P_o\,(1-P_o) - 2i_s\,i_oP_sP_o\right]\,. \end{aligned} \tag{2.9}$$

Let us finally discuss how the elongation $x = x_c - x_a$ discussed in the previous Section affects mechanoreceptor currents. The mean current in Eqn. 2.9 has two fixed parameters (i_s and i_o) while its dependence on the mechanical stimulation stems from two effects: the number of channels and their probability of taking the various conformations.

The channels which are distributed sparsely along the neurite are actually not identical, because they differ in their position with respect to the point of stimulation. Experimental data show that channels are localized in puncta distributed along the neurite with no apparent basal/apical bias and a distribution between successive puncta that is approximately lognormal and has an average inter-punctum distance of about $2\mu m$ [10]. It follows that the various channels and their anchors will be subject to different levels of mechanical stimulation, which are reflected in Eqn. 2.4 via the dependence of the function χ on the undeformed position $\boldsymbol{X}_a$.

It remains unknown whether or not the symmetric response to the application and removal of mechanical loads holds at the level of individual MeT channels or is a macroscopic property of the the ensemble of channels that decorate the touch receptor neurons. For the tether sketch in Fig. 2.1, the former situation would for instance be realized if the point of attachment of the filament to the channel could slide along the circumference of the channel. This system would then be essentially analogous to having a trapdoor occluding the channel and sliding laterally under mechanical stimulation. Conversely, if the point of attachment of the filaments were fixed, individual MeT channels would have a preference in their direction of stimulation; the symmetry would be restored only for the whole neuron due to the random orientation of the channels and their filaments along the neurite. At the level of the average neuron's current, the non symmetric case is analogous to a symmetric one with a lower density of channels along the neurite.

The following approximation (of the mean-field type common in statistical physics [16]) allows us to capture both of the situations above and to simplify the model. The dependence of χ on $\boldsymbol{X}_a$ in Eqn. 2.4 is reduced to two possible classes: a set of channels with a unique non-zero value of χ and the rest of them has $\chi = 0$, e.g. because they are too far from the point of indentation. The number of active channels ($\chi \neq 0$) depends on the following factors. Point indentation of an elastic spherical shell leads to profiles of deformation with an extension scaling as a power law of the indentation, see e.g. [16, 23] for the case without or with internal pressure, and a similar behavior holds for a ball indenting a cylinder with internal pressure. The channels within the typical length scale of deformation (micrometers) provide an upper estimate of the number of active channels, which is achieved in response to fast indentations. On the other hand, we physically expect that if the final deformation is produced slowly, the number of active channels will be reduced. The number of active channels is therefore expected to increase as the indentation is varied and decrease over some typical timescales of relaxation comparable to those of the filament dynamics, *i.e.* to have a behavior similar to $|x|$ as defined in the previous Section. This remark suggests that, rather than introducing an independent dynamics with a set of supplementary parameters, we could parsimoniously use $|x|$ as a proxy for the number of active channels and introduce a logarithmic term to the free energy difference between closed and open conformations of the channels:

$$\beta \Delta G_{oc} = \frac{x_h - \mid x \mid}{x_s} - p \log\left(\mid x \mid\right), \tag{2.10}$$

with the (positive) exponent p left as a fitting parameter. The logarithmic term in Eqn. 2.10 introduces a dependence $|x|^p$ in the ratio P_o/P_c, i.e. it increases the depletion of the channels in the open state and leaves them closed for weak elongations (small $|x|$). The first term on the right-hand side of Eqn. 2.10 is a standard Boltzmann form that favors the opening of the channel linearly as the filament gets elongated. The two constants x_h and x_s are free parameters that absorb also the term that makes the logarithm non-dimensional. The dependence of the Boltzmann form is on $|x|$ for the reasons discussed above, *i.e.* that we are describing the current of the whole neuron, but we iterate that the on-off symmetry at the single-channel level is an open issue.

We note that this approach has dramatically reduced the complexity of the problem : a population of many channels has been replaced by a single typical one, which responds to the stimuli encoded by the elongation of its attached filament by the effective potential Eqn. 2.10 that subsumes properties of individual channels and of their entire ensemble.

Finally, the free energy of the sub-conductance state might *a priori* have a functional dependence and/or parameters differing from Eqn. 2.10 but, again in order to minimize free parameters, we make the assumption that its free energy is intermediate between the closed and the open state

$$\Delta G_{os} = a\Delta G_{oc}\,; \quad \Delta G_{sc} = (1-a)\,\Delta G_{oc}\,, \tag{2.11}$$

with the only parameter $0 \leq a \leq 1$.

2.1.3 Additional viscoelastic models

To improve the quality of theoretical predictions, we present two additional models of the viscoelastic interaction between body deformation and channel activation. These models are concerned with fast changes in external loads that should probe the fine structure of the viscoelastic dynamics. In brief, we find that while refined viscoelastic models do improve the description of the experimental data, the simpler Kelvin model already captures the main behaviors.

The friction term introduced in Eqn. 2.2 supposes an instantaneous response of the medium. In reality, a finite time is usually required and the simplest model capturing this effect is

$$\mathcal{F}\left(v(t)\right) = -\gamma \int_{-\infty}^{t} K\left(t-u\right)\, v(u) du\,, \tag{2.12}$$

where K is the friction kernel and $v(t)$ is the relative velocity of an object moving within the viscoelastic medium. We show below that a kernel of the form

$$K\left(t\right) = \frac{1}{\eta} e^{-\frac{t}{\eta}}\,, \tag{2.13}$$

leads to the viscoelastic standard linear model [20, 21] and agrees with our experimental data. If the memory of the kernel is negligible with respect to the characteristic time of variation of v, then the friction Eqn. 2.12 reduces to Eqn. 2.2.

With the friction term Eqn. 2.12, Eqn. 2.4 for the elongation $x = x_a - x_c$ becomes

$$\int_{-\infty}^{t} K\left(t-u\right)\, \frac{dx(u)}{du} du + \frac{1}{\tau} x = \chi \int_{-\infty}^{t} K\left(t-u\right)\, \frac{d\zeta(u)}{du} du\,, \tag{2.14}$$

where $\tau = \gamma/k$, χ is taken constant as discussed in Section 2.1.2 and the kernel $K\left(t\right)$ is given by Eqn. 2.13. Note that the Laplace transform of the left-hand side in Eqn. 2.14 is $\left(\frac{s}{1+s\eta} + \frac{1}{\tau}\right) \hat{x}(s)$, where s is the argument of the Laplace transform $\hat{x}(s)$ of $x(t)$. That is the expression for the Standard Linear Solid model (also known as generalized Maxwell-Wiechert model, in the simplest version with two elements, a spring in parallel with a Maxwell module, *i.e.* another spring in series with a dashpot) [20, 21]. As discussed above, the Standard Linear Solid model reduces to a dashpot in parallel to a spring, i.e. a Kelvin module, when the memory of the friction term is negligible [20, 21].

The integral Eqn. 2.14 is solved by introducing the auxiliary variable $m(t) = \int_{-\infty}^{t} K(t-u)\ [x(u) - \chi\ \zeta(u)]\, du$, integrating by parts and using the exponential form Eqn. 2.13 to obtain the differential equations

$$\begin{cases} \frac{dm(t)}{dt} = -\frac{1}{\tau+\eta}\,[m(t) + \chi\,\zeta(t)]\ , \\ x(t) = \frac{\tau}{\tau+\eta}\,[m(t) + \chi\,\zeta(t)]\ . \end{cases} \tag{2.15}$$

It is verified that the property of adaptation and the on-off symmetry of the response that were discussed in Section 2.1.1 for Eqn. 2.4 hold for the Linear Solid model Eqn. 2.14 as well.

Viscoelastic models more complex than the Kelvin module and the Linear Solid model involve rational functions of higher order in the Laplace variable and generally probe higher-order time derivatives [20, 21]. As discussed, we also expect that differential displacements and the function χ in Eqn. 2.3 feature some dependence on the speed of indentation. Predictions could be strongly affected by those additional terms, *e.g.* for protocols of stimulation that involve extreme time-variations. In order to gauge those effects and the robustness of our predictions, we wrote down (and compared results to previous models) the following general viscoelastic model:

$$\sigma_1 \frac{d^2x}{dt^2} + \frac{dx}{dt} + \frac{1}{\tau}x = \chi\left(\frac{d\zeta(t)}{dt} + \sigma_2\frac{d^2\zeta(t)}{dt^2}\right)\ , \tag{2.16}$$

which contains time-derivatives up to the second order. The parameters τ, σ_1 and σ_2 in Eqn. 2.16 are three independent time constants. This structure of the Eqn. 2.16 can be obtained by modeling the viscoelastic interaction between the anchor and the medium by a dashpot in series with a Kelvin module [20, 21] and replacing Eqn. 2.3 by $x_a(t) - S(X_a, t) \sim x(t) - \left(\chi(X_a)\zeta(t) + \chi_1(X_a)\frac{d\zeta(t)}{dt} + \ldots\right)$, which takes into account possible viscoelastic dependencies on the history of the external stimulation. Equation 2.16 is then obtained using the overdamped approximation, keeping time derivatives up to the second order and rescaling out the constant of the first derivative.

To conclude, we anticipate from the comparison between the models of Eqn. 2.4, Eqn. 2.14 and Eqn. 2.16 that any corrections or improvements to the model would be relatively minor at least for the stimulation profiles currently available. Thus, it is premature to consider higher-order and nonlinear effects, which explains the nature of the model Eqn. 2.16.

2.2 Comparison with experimental data

We evaluated the ability of theoretical models to reconstruct MeT current response dynamics as follows. We obtained model predictions by optimizing parameters over the entire ensemble of stimulations as described below. We then tested the robustness of the predictions by varying model and parameters, e.g. we asked how well model parameters derived from the response to indentation pulses could reproduce the response to ramp-and-hold stimuli and sinusoidal stimulation. The most rigorous comparison was made for two recordings (identified by their laboratory indices 169 and 173) in which a complete data set was obtained including the response to a series of indentation pulses, sinusoidal stimuli, and ramp-and-hold stimuli. Thus, we focus on these two data sets and demonstrate below that the model is sufficiently robust that the parameters derived from one recording are sufficient to capture the main features of another recording.

2.2.1 Inference of the parameters of the models

For all the viscoelastic models introduced above, the parameter χ can be set to unity by rescaling x and redefining the parameters x_h and x_s appearing in Eqn. 2.10. As for the rates of conformational transitions, a parsimonious form respecting the detailed balance constraints Eqns. 2.6 and 2.11 is

$$\begin{aligned} R_{sc} &= r_{cs} e^{(1+b)(1-a)\beta\Delta G_{oc}} \,; \quad R_{cs} = r_{cs} e^{b(1-a)\beta\Delta G_{oc}} \,; \\ R_{os} &= r_{so} e^{(1+d)a\beta\Delta G_{oc}} \,; \quad R_{so} = r_{so} e^{da\beta\Delta G_{oc}} \,. \end{aligned} \tag{2.17}$$

Here, r_{cs} (r_{so}) controls the speed of the transitions between the closed and the sub-conductance states (the sub-conductance and the open states) and the parameters b and d control their global shift with respect to variations of the free energy difference. Since the probability of opening the channels is expected to grow with $\mid x \mid$, the parameters b, d are limited to the range $-1 \leq b \leq 0$.

The parameters of the models are inferred from the comparison with experimental curves by using a nonlinear least usare fit. The optimization finds the parameters that best reproduce the data, viz. yield the least-squares distance between the predicted and the observed current profiles. This procedure gave for the parameters of the various models the values shown in Tables 2.1 and 2.2 for the recording 169 and 173, respectively.

2.2.2 Results

Predictions for the Standard Linear Solid model Eqn. 2.14 are shown in Figs. 2.2 and 2.3 for the recordings 169 and 173, respectively. A single set of parameters is used to fit the ensemble of the curves, i.e. ramps, steps and sinusoids, for each one of the two recordings. The optimal parameters of the model differ between the two recordings, as expected from the diversity of the response and of the mechanical properties among individuals. It is important, though, that no fine tuning is needed and the two sets of parameters are quite close. In view of the multidimensional nature of the set of parameters, the best demonstration is provided by Fig. 2.3, where we computed the response of the recording 173 using the optimal parameters for the recording 169, and compared the result to the experimental curves for the recording 173. Even though some discrepancy is detectible, the overall agreement is very good and confirms the consistency of the two sets of parameters.

A relevant remark on the curves in Figs. 2.2 and 2.3 is the saturation of the response at high frequencies, i.e. the fact that the response does not follow the stimulation and sets to a constant level. That is mainly due to the inertia of the channels as the switches among the different conformations cannot follow the stimulation when its oscillations are too rapid. The populations in the conformational states of the channels settle then to roughly constant values (with noise).

In Fig. 2.4, we show how model parameters derived from the response to indentation pulses only, could reproduce the response to ramp-and-hold stimuli and sinusoidal stimulation (for the same recording). In other words, we optimize the parameters on a subset

τ (ms)	η (ms)	σ_1 (ms)	σ_2 (ms)	x_h (μm)	x_s (μm)	p	I_o (pA)	I_s (pA)	$1/r_{co}$ (ms)	$1/r_{cs}$ (ms)	$1/r_{so}$ (ms)	a	b	d
1.9	/	/	/	0.009	1.20	1.14	-23.2	/	36	/	/	/	-0.98	/
1.3	/	/	/	0.042	1.14	1.32	-37.6	-13.3	/	118	71	0.06	-0.98	-0.58
1.2	0.001	/	/	0.062	1.09	1.35	-49.5	-9.2	/	142	71	0.06	-0.98	-0.59
1.3	/	0.04	0.1	0.045	1.15	1.33	-23.9	-7.3	/	73.5	200	0.06	-0.98	-0.58

Table 2.1: The optimal parameters obtained by fitting experimental data of the recording 169 to the various viscoelastic models presented in the text. The models correspond to different rows : the first and the second to the Kelvin model Eqn. 2.2 with two and three conformational states of the channels, respectively; the third to the Linear Solid model Eqn. 2.14; finally, the fourth row corresponds to the second-order model Eqn. 2.16. The parameters of the channels are defined in Eqns. 2.10 and 2.17. The symbol / indicates that the corresponding parameter does not appear in the model.

τ (ms)	η (ms)	σ_1 (ms)	σ_2 (ms)	x_h (μm)	x_s (μm)	p	I_o (pA)	I_s (pA)	$1/r_{co}$ (ms)	$1/r_{cs}$ (ms)	$1/r_{so}$ (ms)	a	b	d
1.7	/	/	/	0.017	0.36	1.40	-14.7	/	35	/	/	/	-0.98	/
1.3	/	/	/	0.10	0.24	1.38	-28.0	-1.52	/	58	121	0.05	-0.98	-0.56
1.4	0.065	/	/	0.20	0.21	1.37	-30.0	-2.35	/	70	88	0.05	-0.98	-0.57
0.8	/	0.06	0.1	0.83	0.44	0.52	-28.9	-2.38	/	238	151	0.06	-0.98	-0.56

Table 2.2: The optimal parameters obtained by fitting experimental data of the recording 173 to the various viscoelastic models presented in the text. The structure of the rows and the notation are as in Table 2.1.

of experimental data and then compare the predicted current for the rest of experimental stimuli. Even though the global optimization gives a better description, predictions are clearly compatible with experiments.

We next compare the quality of the predictions for the different models Eqns. 2.2, 2.14 and 2.16. We find that in both recordings the performance of the models are similar and differences can only be seen in the fine structure of the curves. Some representative plots are shown in Figs. 2.5 for the recording 169. For clarity we report the SLS results only, as Kelvin and SLS models in Eqns. 2.2 and 2.14 yield almost identical results. That is consistent with the fact that the inferred memory time η is of the order of 10^{-5}s, i.e. about two order of magnitude faster than any timescale of the experimental stimulations. The general second-order model Eqn. 2.16 slightly improves the quality of the predictions. In particular, we observe that the response to steps better captures abrupt changes in the stimulation and is closer to the experimental results as compared to the other models. However, differences are relatively minor and not quite sufficient to characterize quantitatively the nature of the corrections to the basic models Eqns. 2.4 and 2.14. That will require the next-generation experimental set up which is currently under development, with a more extended dataset for a single recording, higher frequencies of stimulations and reduced instrumentation noise so as to precisely measure the weak currents generated by slow stimulations.

Finally, we compare in Figs. 2.6 and 2.7 the results for the Kelvin model with two or three conformational states. For both recordings 169 and 173, the predictions with three states give a slightly better fit but the main behavior is already captured by the two-states model (with less parameters). The bottomline is that the behavior for the various viscoelastic models is relatively similar and the resulting predictions for the available profiles of stimulation are robust with respect to details of the models.

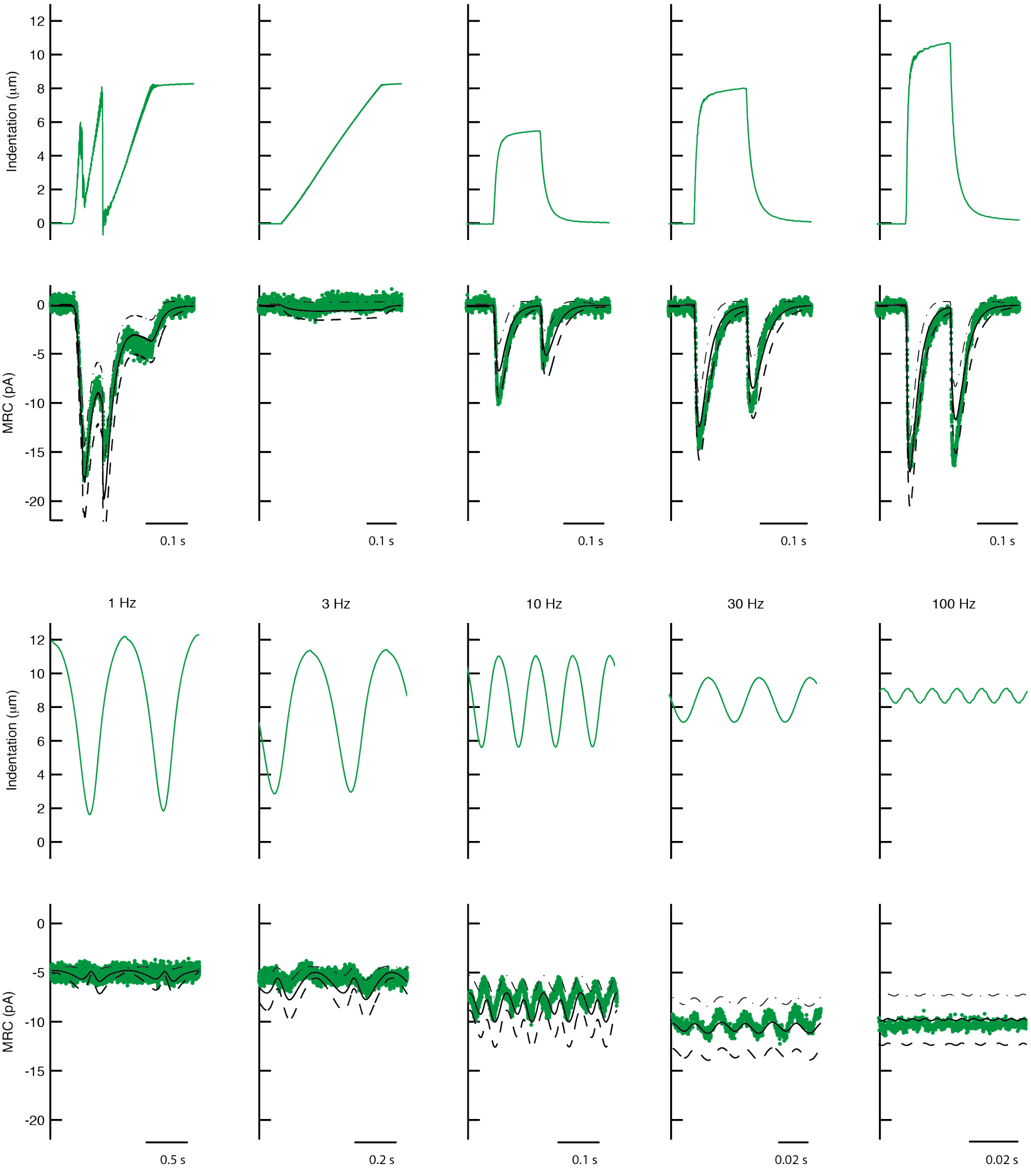

Figure 2.2: Responses of the recording 169 to an ensemble of diverse stimuli. The first and the third rows show the time course of the indentation applied to the recording. The second and the fourth rows show the ionic current : Green, the experimental curve; Solid black: the theoretical prediction from the Standard Linear Solid model Eqn. 2.14; Dashed lines: the expected upper and lower limits for the predicted current, based on one standard deviation estimated via Eqn. 2.9 and a typical number of 25 activated channels [9].

2.2.3 TRNs function as a band-pass mechanical filter

General considerations on passive viscoelastic materials suggest that the force needed to generate a fixed-amplitude indentation of the cuticle should increase with frequency

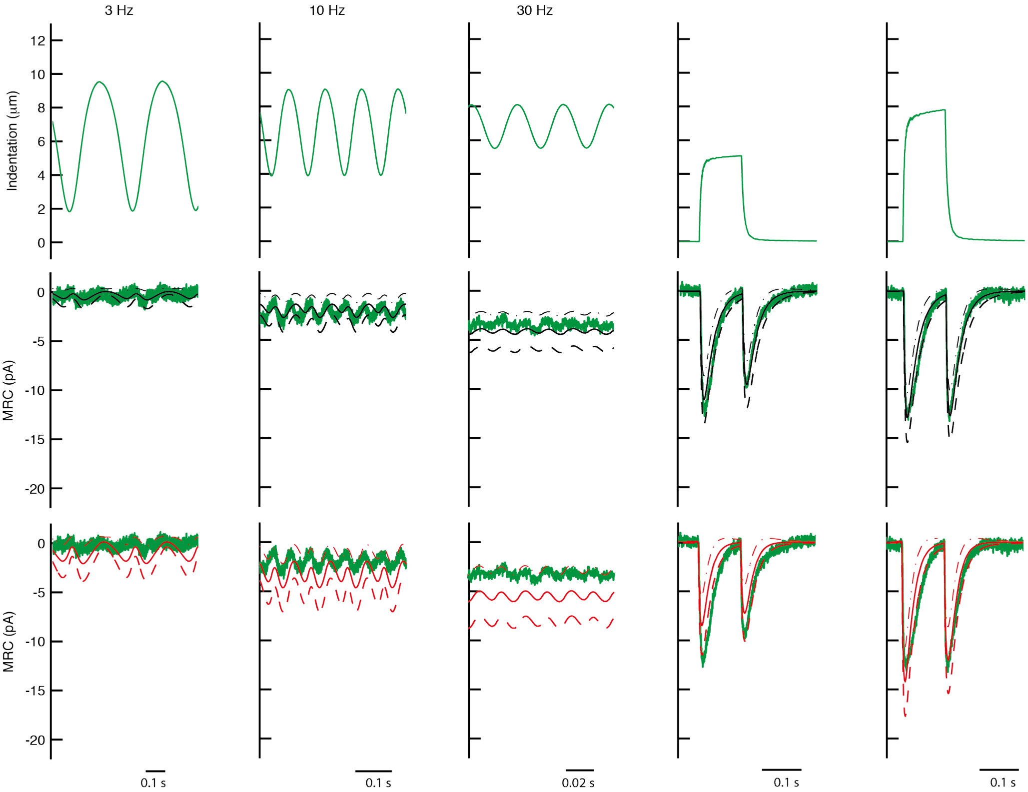

Figure 2.3: Diversity of the modeling parameters between different recordings. We show the experimental stimulation in the first row, the experimental responses of the recording 173 (green) in the other two rows and compare them to the predictions of the Standard Linear Solid model Eqn. 2.14 using the optimal parameters for the recording 173 itself (black, second row) and those for the recording 169 (red, third row), which were used to generate the predictions for Fig. 2.2. Predictions in the second row (with optimal parameters for the recording 173 itself) are clearly of better quality, namely the behavior at high frequency is better captured, yet the overall behavior is consistent even with the parameters optimized for the different recording 169.

at high frequencies [21]. In this scenario the amplitude of the resulting indentations would be expected to decrease as their frequency increases. This decrease in indentation amplitude, in combination with the failure of slowly moving stimuli to activate currents, would produce a band-pass filter response.

Figure 2.8a shows the experimental results together with simulations based on this scenario. Limitations in the bandwidth of the experimental set up that has been used to investigate the model predictions prevented a full experimental exploration of the frequency response range of *C. elegans* TRNs and an experimental testing of whether the entire system behaves more like a high-pass or band-pass mechanical filter. We investigated numerically how the entire mechanical system operates under conditions in which the applied peak-to-peak force is independent of the stimulus frequency. As shown in Fig. 2.8b, this analysis reveals that indentation decreases with frequency and that peak current and sensitivity reach maximal values at 150 and 725 Hz, respectively. The simulation also reveals that current fluctuates at twice the input frequency and that the am-

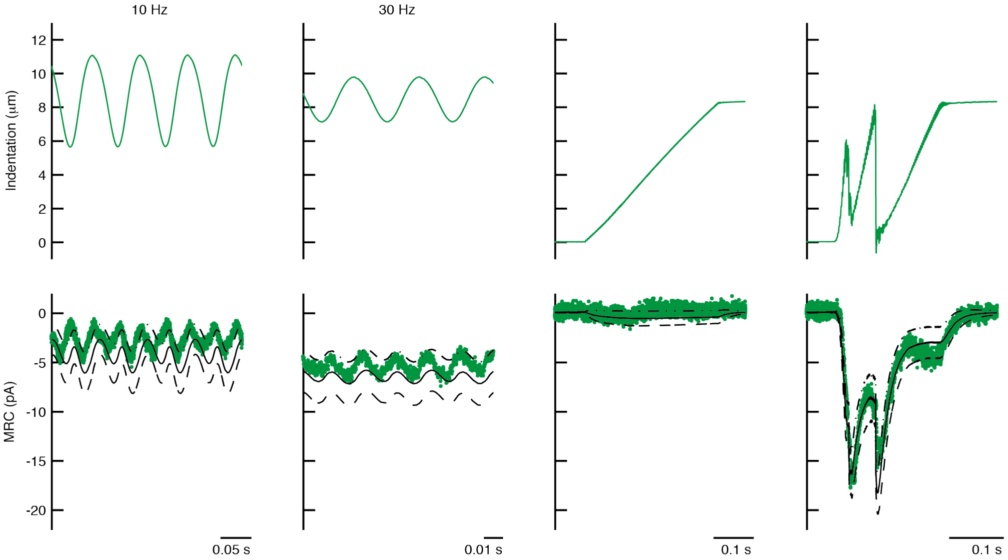

Figure 2.4: Predictions with model parameters derived from the response to indentation pulses reproduce the response to other profiles of stimulation. We optimized parameters of the Standard Linear Solid model to reproduce the response to indentation pulses for the recording 169 and then compared the predictions (with that set of parameters) of the model to experimental data for the response to ramp-and-hold stimuli and sinusoidal stimulation (for the same recording 169).

plitude of such fluctuations declines with frequency (Fig. 2.8c). One model to explain this observation is that at high frequencies the channels dwell in open states and rarely visit the closed states.

We note that these speculations about mechanical filtering in soft animals do not take into account active mechanisms for modulating body stiffness during touch stimuli, which have been observed in other animals (e.g. Ref. [24]) and which would provide organism-level mechanisms for regulating the frequency-dependence of touch sensation.

2.3 Discussion

The response dynamics presented here are shared by other rapidly adapting mechanosensory neurons, including C. elegans and Drosophila nociceptors [9, 25, 26, 27, 28] and the neurons that innervate Pacinian and Meissner corpuscles and hair follicles in mammals (reviewed in Refs. [7, 29]). The fact that similar response dynamics are found across phyla and in sensory neurons that diverge radically in their morphology strongly suggests that this property arises from a common physical mechanism. Importantly, the model presented and validated here only requires a channel that responds and adapts to its environment through viscoelastic dynamics. Several molecular embodiments are compatible with our model, such as a single or multiple elastic filaments tethered directly to the MeT channel or to a structure that occludes the ion permeation pathway that is pushed aside laterally by deformations of the skin. Furthermore, such filaments might be anchored to the extracellular matrix or to the cytoskeleton. Presently, experimental data make a direct linkage between the MeT channel and the microtubule cytoskeleton

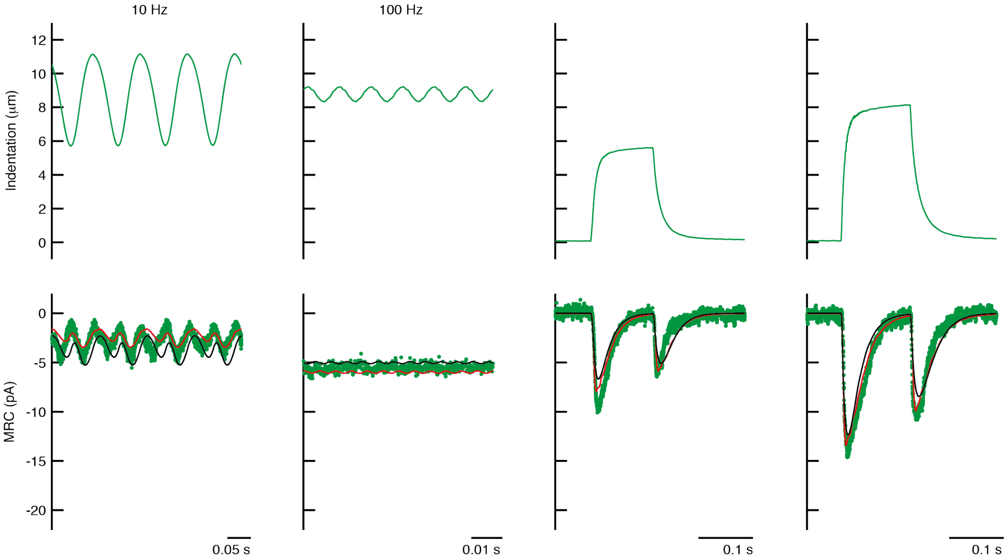

Figure 2.5: Comparison between the currents for the recording 169 predicted by different models. We show the responses to a set of stimulations and compare them to the predictions of the three viscoelastic models discussed in the text. The predictions obtained by using the Standard Linear Solid model Eqn. 2.14 (black lines) (which essentially coincide with those of the Kelvin model, data not shown) only slightly differ from the prediction given by Eqn. 2.16 (red line) that gives the best fit. As explained in the text this comes from the inclusion of higher-order derivatives of the indentation that better capture rapid variations in the dynamics.

in TRNs unlikely [10, 30]. However, such a connection has been proposed and characterized for campaniform sensilla in Drosophila adults and multidendritic nociceptors in larvae [31, 32]. Finally, the viscoelastic dynamics we propose might arise from the plasma membrane itself, which suggests a proteinaceous tether to the MeT channel may not be a required element for gating under physiological conditions. Identifying the microscopic and molecular nature of the mechanical unit will require targeted experiments to identify the viscoelastic elements and determine how such elements interact with MeT channels in situ. The findings and methods reported here provide the tools to manipulate key proteins and observe their effects on mechanics and adaptation. The mechanism that we propose establishes an unexpected connection between two different mechanical senses: touch and hearing. The elastic filament system is reminiscent of similar models originally proposed for hair cells [33], though with one major difference. Fast adapting afferents respond symmetrically to touch, at both the onset and offset of a stimulus. Conversely, the response of hair cells is asymmetric with respect to the application of force, e.g. responses are only seen at the onset of stimulations pointing toward the kinocilium of the hair bundle. The asymmetry is due to the controlled geometry of the tip links and less pronounced in immature hair cells when multiple tip links are present and their directions are still randomly oriented [34]. The symmetry observed in C. elegans TRNs relates to the thinness of the worm cuticle and the ensuing strain in the filaments that occurs at both the onset and offset of stimulation in opposite directions yet with comparable amplitudes. However, whether symmetry holds at the level of individual MeT channels or whether it is only retained at the level of the whole mechanorecep-

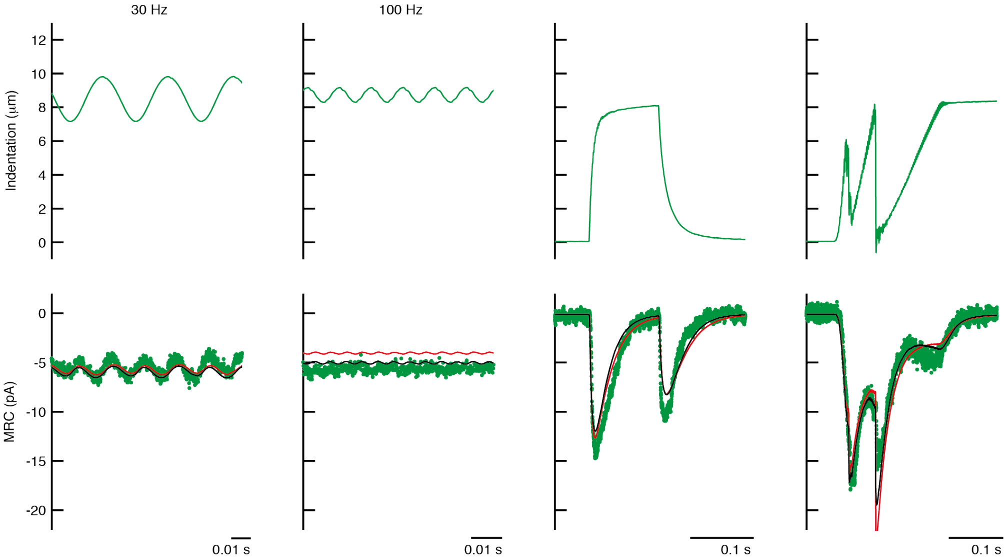

Figure 2.6: The comparison between the Kelvin model Eqn. 2.2 with two *vs.* three conformational states of the channels. The curves for the two-state (open and closed, with no transitional state) model are shown in red while the predictions for the three-state model are in black. The curves refer to experiments on the recording 169.

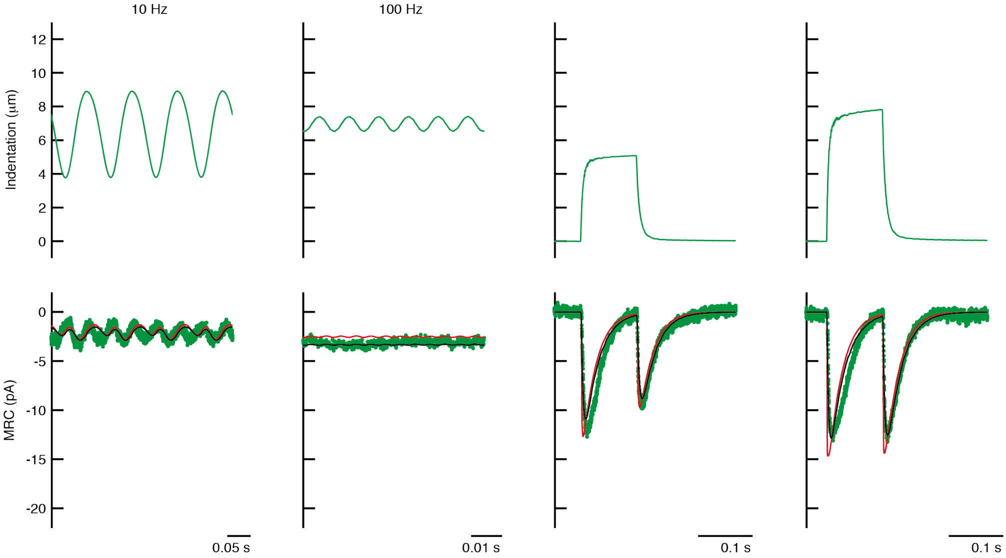

Figure 2.7: The comparison between the Kelvin model Eqn. 2.2 with two and three conformational states of the channels. The colors and the curves are as in Fig. 2.6 but refer to experimental data obtained for the recording 173.

tor neuron remains an open question. For the schema shown in Figure 2.1, individual MeT channels would show symmetric on-off responses if, for instance, the attachment

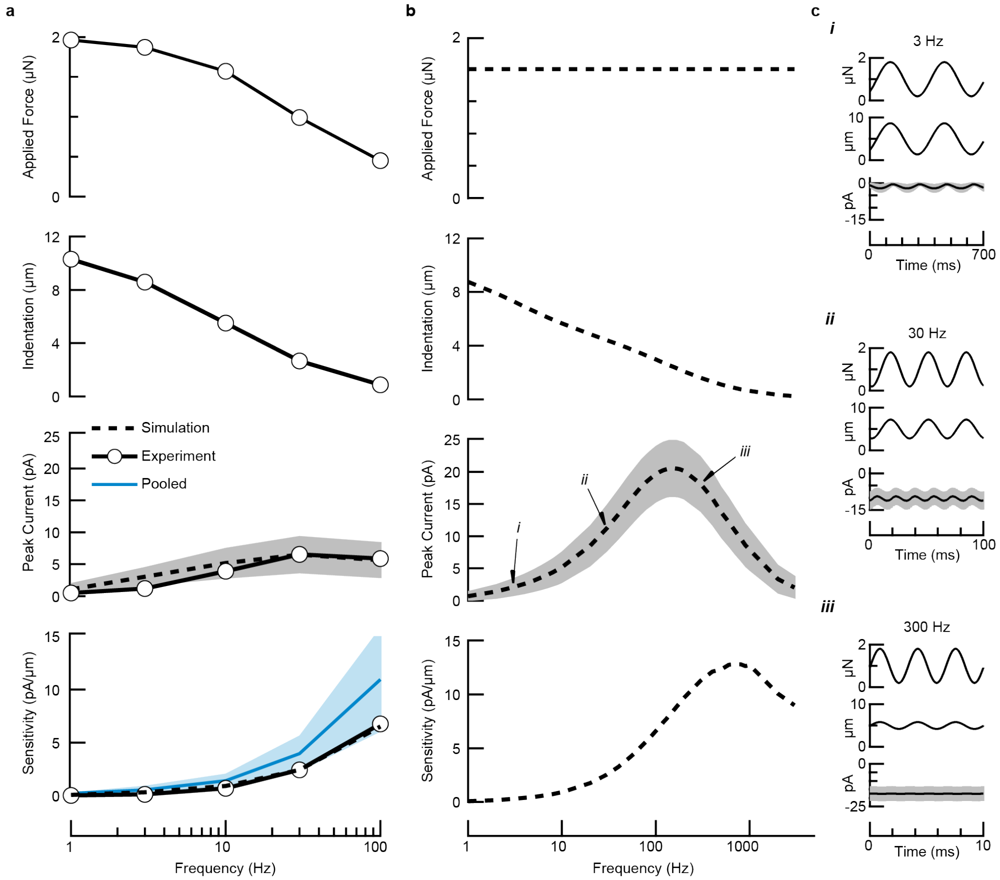

Figure 2.8: Experimental and computational study of the frequency response of tactile sensation in soft animals. (A) Simulations using parameters optimized to fit responses to mechanical stimuli reproduce experimental responses to sinusoidal stimuli in a representative recording from a soft worm. Table 2.1 (third row) lists the parameters for the SLS model. Shown are (top to bottom) applied force (peak-to-peak), resulting indentation (peak-to-peak), peak current, and sensitivity (pA/μm). Solid black lines show experimental results from a representative recording; solid blue lines show results pooled across four recordings; dashed black lines show simulations; and shaded areas indicate the errors in measurement and simulation. Applied force declines with frequency due to limitations in the experimental set up. (B) Simulation of the mechanical and physiological response to applied force up to 3 kHz. Model parameters as in A. Shown are (top to bottom) applied force (peak), resulting indentation (peak), peak current, and sensitivity (pA/μm). Indentation declines with frequency as a result of the properties of the mechanical system, despite a constant amplitude of applied force. (C) Simulations of the indentation and currents evoked by sinusoidal force stimuli. Model parameters as in A and B. As found experimentally, the current varies at approximately twice the frequency of the stimulus, except at high frequencies where large current fluctuations decline.

of the filament to the channel could slide along the circumference of the channel. This system would then be essentially analogous to a trapdoor occluding the channel and sliding laterally under mechanical stimulation. Conversely, if the point of attachment of the filaments were fixed, individual MeT channels would have a preference in their direction of stimulation, and on-off symmetry would be a macroscopic property of the whole neuron due to the random position of the channels and their putative filaments along the neurite [10, 30]. Thus, in the absence of symmetry-breaking structures such as those found in vertebrate hair cells, insect bristles or mammalian guard hairs [35, 36], we expect that systems characterized by somatosensory neurons embedded within thin tissues will generally feature on-off symmetry in their touch responses. How might C. elegans use sensitivity to strain, velocity, and vibration? It has long been known that C. elegans TRNs are involved in sensing both gentle touch to the body and non-localized mechanical taps (reviewed in Ref. [37]). Worms reverse in response to anterior touch, an avoidance behavior that allows them to escape from predatory fungi [12]. Our results suggest that a robust response from C. elegans TRNs requires a brief contact of sufficient indentation depth. This temporal and spatial threshold may ensure that TRNs do not interpret small particles like bacteria as aversive and back away from a potential food source. Filtering low frequencies may also enable TRNs to ignore body movements, which involve undulation frequencies on the order of 0.5 Hz when crawling on standard growth plates in the absence of food (e.g. Ref. [13, 15]). Thus, the fine-tuning of the system may help TRNs focus on responding to aversive mechanical stimuli, while leaving stimuli such as those produced by substrate texture and self-movement to other mechanoreceptor neurons.

CHAPTER 3

The mechanics of *C. elegans* body

In the previous Chapter, we proposed that the gating of channels in *C. elegans* touch receptor neurons is driven by local deformations in the nematode body. In order to obtain predictions on the current response to mechanical stimulations, we used an effective description for the extension and the intensity of the stimulation produced by the indentation of the body. The scope of this Chapter is to describe preliminary work aimed at going beyond that mean-field description and at quantitatively characterizing body deformations in mechanical stimulation experiments.

3.1 Definition of the model and its parameters

In this Section we characterize the mechanical response of the body of *C. elegans* in terms of a model of pressurized thin shell. We show that the model quantitatively accounts for the experimentally observed force-indentation relation and the deformation profiles. Furthermore, the analysis provides an estimate of the internal pressure and the bulk modulus, both of them in agreement with previous measurements appeared in the literature.

C. elegans body consists of an outer tube separated from an inner tube by a fluid-filled pseudocoelom. The cuticle, hypodermis, excretory system, neurons, and longitudinal muscles comprise the outer tube or shell, and the pharynx, intestine, and gonad form the inner tube. Because of this structure, we shall describe the worm as a cylindrical elastic shell with internal pressure, as previous works in the literature [38]. The observation that the interior of a nematode is under pressure was first documented for *Ascaris* in Ref. [39]. The model accounts for the common observation that a healthy *C. elegans* worm bursts when the cuticle is punctured. The elasticity of the shell is meant to provide an effective description of the mechanical properties of the different elements in the nematode outer tube. The pressure is effectively generated by the internal organs and by the fluid-filled pseudocoelom.

Typical experimental conditions feature a worm glued upon a plate and a spherical bead of radius $\sim 5\mu m$ indenting the body of the worm down to a maximum depth of $\sim 10\mu m$ (see Fig. 3.1). The maximum experimental indentation can therefore be almost half of the radius of the shell, and is comparable and even bigger than the shell thickness, whose value is $\sim 1\mu m$. The qualitative consequence of these remarks is that the displacements of material points in the shell are not *a priori* small. However, the strain within the material is not necessarily large and the simplest assumption is to account for large displacements but still maintain a Hookean, i.e. linear, relation between stress and strain [16, 17, 18]. In other words, the strain in the material is still small yet deformations of the material are not. The most conspicuous consequence is that the linear expression of the strain is not appropriate and must be replaced by the nonlinear Green-Lagrange expression. That leads to the appearance of nonlinear terms in the equations, which are usually neglected in the simpler linear theory where both strain and deformations are small [16, 17, 18].

A general mathematical description of the dynamics described above is provided by the equations of three-dimensional (3D) elasticity [16, 17, 18]. The equations are:

$$\partial_j \left[\sigma_{ij} + \sigma_{kj} \frac{\partial u_i}{\partial x_k} \right] = 0 \,, \tag{3.1}$$

where ∂_j denotes the partial derivative with respect to the spatial coordinate x_j (with $j = 1, 2, 3$), the tensor σ_{ij} is the stress tensor (Piola-Kirchoff of the second type), u_i is the i-th component of the displacement and the convention of the sum over repeated indices is used. As it will be discussed below, the equation (3.1) is supplemented by the boundary conditions expressing the action of the internal pressure p and of the external forces, namely by the structures within the internal tube of *C. elegans* and by the indenting ball for mechanical experiments.

The stress tensor σ_{ij} in (3.1) is energy conjugate to the Green-Lagrange strain tensor $2\varepsilon_{ij} = (\partial_i u_j + \partial_j u_i) + \partial_i u_k \partial_j u_k$, i.e. the variation of the elastic energy $\delta\mathcal{E}_{el}$ upon a deformation is given by $\delta\mathcal{E}_{el} = \int \sigma_{ij}\, \delta\varepsilon_{ij}\, dV$. Note that the equations above are appropriate for large deformations, as witnessed by the second nonlinear term appearing in (3.1) and by the quadratic term in the Green-Lagrange strain tensor. The relevant parameters of the elastic model are: the radius of the middle surface of the shell R, the length L of the worm, the thickness t of the shell, the internal pressure p, the Young's modulus E and the Poisson's ratio ν of the shell. A schematic representation is given in Fig. 3.1 and typical known values for the length and the external radius are $L \simeq 1\,mm$ and $R + t/2 \simeq 25\mu m$, respectively.

The elastic parameters E and t are effective quantities that subsume the different elements in the nematode outer tube. They enter the dynamics via the relation between stress and strain tensors: $\sigma_{ij} = \frac{E}{1+\nu} \left(\varepsilon_{ij} + \frac{\nu}{1-2\nu} \varepsilon_{kk} \delta_{ij} \right)$. Diverse estimates of those parameters (and the pressure p) are present in the literature, which will be discussed in Section 3.2.2. Our approach to determine the value of those parameters will be to combine modeling with data from indentation experiments.

A notable limit of the three-dimensional equations of elasticity (3.1) is provided by the shallow thin shell equations [17, 18]:

$$\begin{cases} B\nabla^4 w + \nabla_k^2 \phi - [\phi, w] = p - F(x, z) \,, \\ \frac{1}{S} \nabla^4 \phi - \nabla_k^2 w = -\frac{1}{2} [w, w] \;, \end{cases} \tag{3.2}$$

which we shall use below for analytical estimates. The brackets and derivatives appearing in (3.2) are defined as

$$[f, g] = \frac{\partial^2 f}{\partial x^2} \frac{\partial^2 g}{\partial z^2} - 2 \frac{\partial^2 f}{\partial x \partial z} \frac{\partial^2 g}{\partial x \partial z} + \frac{\partial^2 g}{\partial x^2} \frac{\partial^2 f}{\partial z^2} \,, \quad \nabla_k^2 = \frac{1}{R} \frac{\partial^2}{\partial z^2} \,.$$

As shown in Fig. 3.1, the variables $y = y(x, z)$ and $w = w(x, z)$ represent the middle surface and the deformation field of the cylindrical shell, respectively. The deformed surface is expressed as $y + w$ and we choose the axes so as to have the plane $y = 0$ tangent to the top of the cylinder. The Airy stress function ϕ is the single scalar function needed for the parametrization of the in-plane components of the stress tensor: $\sigma_{xx} = \partial_{zz}^2 \phi$,

$\sigma_{zz} = \partial^2_{xx}\phi$ and $\sigma_{xz} = -\partial^2_{xz}\phi$. The reduction in the number of independent components is physically due to the thinness of the shell and the resulting smallness of the vertical components of the stress tensor. The parameters $B = Et^3/12(1-\nu^2)$ and $S = Et$ are the bending and stretching stiffness, respectively. Finally, p and F are the internal pressure and the external force applied by the indenter. In the limit where the radius R becomes infinite and the ∇^2_k term can be neglected, the equations (3.2) reduce to the Föppl-von Karman equations for a thin plate [17, 18].

Eqs. (3.2) provide a good approximation of the original full equations (3.1) if the shell is thin and the surface is shallow (see [17, 18]), conditions that are expected *a priori* to be satisfied for the nematode in our experimental conditions. The nonlinear structure of (3.2) reflects the fact that displacements are not small, which was mentioned above. The resulting nonlinear effects are usually called geometric because they relate to the deformation of the shape of the surface and their dynamics has a strong connection with the geometry of surfaces [17, 18].

3.2 Results

3.2.1 Numerical simulations

The nonlinear structure of the 3D nonlinear elasticity equations (3.1) (or its 2D limit (3.2)) makes the problem notoriously difficult for full analytical solutions. Therefore, we decided to attack the problem numerically by finite-element numerical methods (see [40] for an introduction). Numerical simulations of the 3D nonlinear elasticity equations (3.1) were performed using the open-source program *code-aster* [41]. The simulations use conventional hexahedral element with 8 standard nodes (HEXA8), and a mesh sensitivity study was performed to ensure that the results are minimally sensitive to the element size.

As for the boundary conditions, the volume of the glue that attaches the worms onto the plate of the experimental set-up, strongly limits the vertical displacement of the lower half of the body of the worm. To describe this feature in our simulations we chose two different boundary conditions and compared results.

For the first boundary condition, we consider the lower half of the body of the worm as vertically rigid. Specifically, the cylindrical shape of the worm is divided into an upper half and a lower one by a dissecting plane that is parallel to the plate onto which the worm is glued. Upper and lower halves have equal volume. The upper half is free to move while the lower half is allowed to move only parallel to the dissecting plane.

For the second type of boundary condition, we consider that the lower half is completely fixed and is not allowed to move, neither vertically nor laterally.

We checked the dependency on these two boundary conditions and did not find major differences in the results reported below.

We used boundary conditions with the force acting on the two sides equal to zero. The effect of introducing plugs at the lateral sides is discussed in Section 3.2.4.

Finally, for the dynamics of the internal pressure p, we shall make the simplest possible hypothesis that p holds constant when the rigid bead of the cantilever is displaced and the indentation in the body of the worm modifies. Active mechanisms of readjustment of the internal pressure can be accommodated within our formulation of the problem but the agreement reported below does not seem to require them.

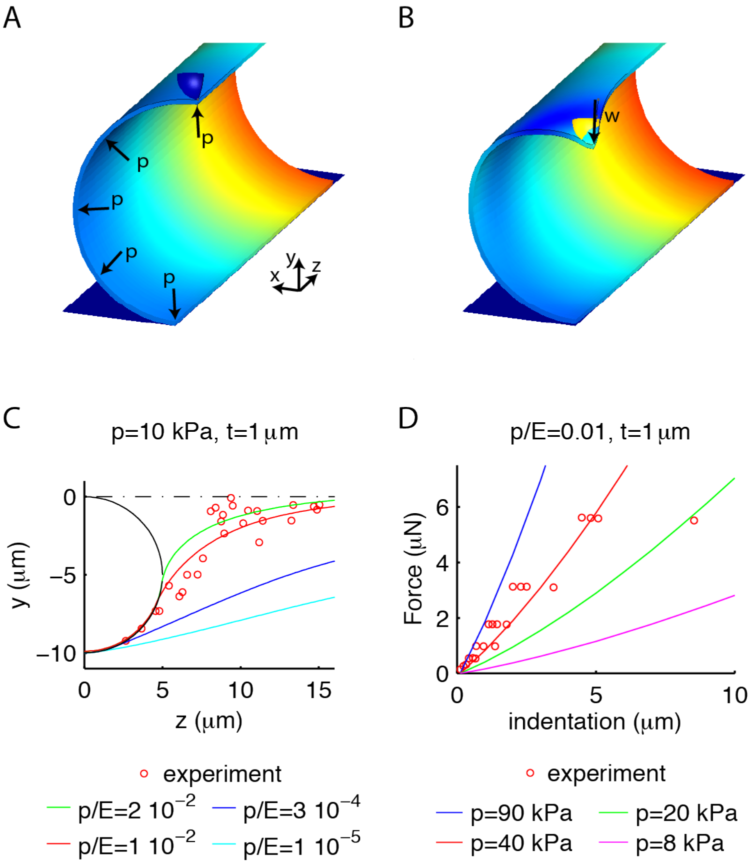

Figure 3.1: Parameters of our elastic model are determined by a comparison between experimental and simulated deformation profiles under indentation. (**A**-**B**) Schematic of an indentation of $10\mu m$ applied at the center of the worm, together with the three-dimensional cross section of the system without (**A**) and with (**B**) indentation. One quarter of the cylinder is shown for clarity. (**C**) The experimental and the numerical deformation profiles of the worm along the longitudinal axis, i.e. the generatrix of the cylinder. (**D**) The experimental and the numerical force-indentation relationships. The best description of the data is obtained by setting $p/E = 0.01$ and $p = 40$kPa. Other parameters in the simulations are $L = 600\mu m$, $\nu = 0.3$. In these simulations, as well as in the following ones, we performed a mesh sensitivity study to ensure that the results were minimally sensitive to the element size of the numerical integration scheme.

3.2.2 Inference of the parameters of the model

An image of the shell prior and after the indentation as obtained from numerical simulations, is shown in Fig. 3.1. Note that the size of the indenter is not negligible with respect to other dimensions of the problem and the region of contact with the cylinder is expected to change with the indentation depth [42]. To simulate the response of a pressurized shell, a uniform internal pressure was first applied to a cylinder with no stress, of appropriate length, thickness and radius. The variation of these quantities upon the application of the internal pressure can be calculated analytically . The resulting formulae are used to choose the initial values that lead to the appropriate sizes of the worm under pressure.

Dimensional analysis dictates that shell deformations for a given indentation depend on p and E only through their ratio p/E. The thickness of the shell t can be rescaled out as discussed below, in Section 3.2.3, and all the other geometrical quantities of the problem are fixed. The resulting prediction for the dependence of the deformation profile on the ratio p/E is shown in Fig. 3.1. The vertical indentation along the longitudinal axis is minimum at the center of indenting ball and decays to zero away from it. The extension of the deformation field decreases with p/E and the best (least squares fit) description of the experimental data is obtained for $p/E = 0.01$.

Using the previous value, we can determine the internal pressure p by analyzing the force-indentation relation and comparing it to the experimental data. The force displacement relation increases roughly linearly with pressure (data not shown). Pressures in the range $p = 32 - 47$kPa provide good agreement with experimental data, with the best fit obtained for $p = 40$kPa. This value of the pressure p is consistent with the value of 2-30 kPa for the hydrostatic pressures that was directly measured in the nematode *Ascaris lumbricoides* [39]. The corresponding value of the Young's modulus is of the order $E \sim 10^2 p = 3 - 5$MPa. This value is about two orders of magnitude smaller than the 380 MPa estimated in [38] but agrees with the 1.3 MPa obtained in [43]. In [38] the value of the Young's modulus was derived from indentation experiments using formulae from the theory of elasticity. However those formulae are meaningful only if the deformations are small compared to the thickness of the shell and our analysis shows that this assumption is not valid in indentation experiments. Conversely, the estimate obtained in [43] is based on measurements of the bending stiffness of the whole nematode.

We conclude this Section by an independent validation of our model. In a recent experiment [44], the mechanical response of *C. elegans* to changes in the external pressure was measured. The nematode shows a uniform change in volume that increases linearly with pressure. The ratio between the relative change in volume $\Delta V/V_0$ and in pressure Δp is called the bulk modulus:

$$\kappa = \frac{\Delta p}{\Delta V} V_0 \,. \tag{3.3}$$

The expected change in volume induced by a change in pressure can be estimated analytically and numerically, as described above. The resulting estimate for the bulk modulus is $\kappa = 150 - 230$kPa, which is in sensible agreement with the experimental value $\kappa = 140 \pm 20$kPa. This agreement is quite significant because the prediction of a global mechanical property like κ was obtained by using parameters inferred from local measurements.

3.2.3 Shell bending is small compared to stretching; stiffness is dominated by internal pressure

The mechanical response of pressurized shells to external stimulations is determined by the interplay between elastic energy (both bending and stretching) of the shell and the internal pressure. In *C. elegans*, contrasting results have been obtain, see [44], and it is unclear at this stage what is the balance among the previous factors in controlling the mechanical response. In this Section we show that the deformation profile observed experimentally is the signature of a shell where the bending energy is globally small with respect to the stretching energy. Furthermore, we show that the indenting ball does most of his work against the internal pressure, i.e. the stiffness of the shell is mostly due to the internal pressure generated within the inner tube of the worm.

To investigate the relative contributions of bending and stretching, we computed numerically the deformation profiles for different values of p/E and t using the approach presented in the previous Section. To quantify the extension of the deformation field we introduce the quantity z_h, defined as the distance along the longitudinal direction from the center of the bead (where the vertical deformation is maximum) to the point where the deformation field reaches half of its maximum value. Fig. 3.2 shows z_h for different values of p/E and t. It is observed that z_h decreases, i.e. the deformation field is more localized, when p/E increases. Conversely, the dependence on the shell thickness t has two different behaviors : the deformation field is wider for thinner shells if $p/E \lesssim 10^{-5}$ but it is narrower if $p/E \gtrsim 10^{-5}$.

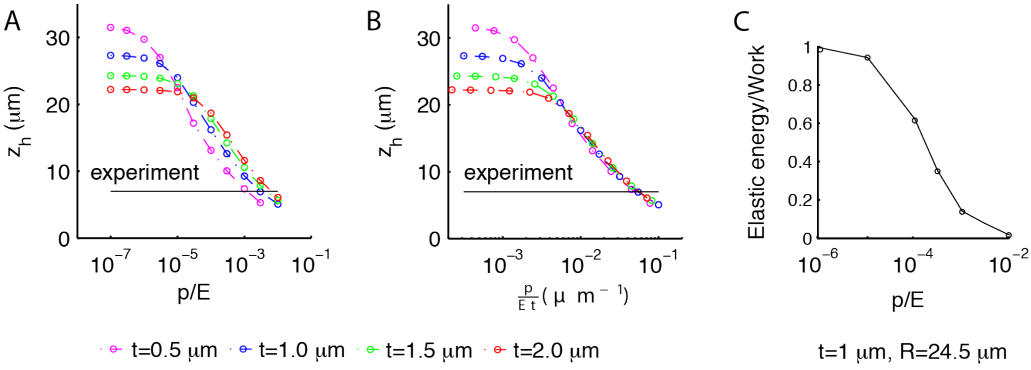

Figure 3.2: The mechanical stiffness of the worm is dominated by the internal pressure. (**A**) z_h *vs* p/E for diverse values of the thickness t, where z_h is defined as the distance from the center of the bead (where the vertical deformation is maximum) to the point where the deformation reaches half of its maximum value. The qualitatively different behaviors at small and large values of p/E are due to the contributions of bending to the elastic energy. (**B**) z_h as a function of p/Et. Curves corresponding to different values of t are expected to collapse if the coefficient of the bending term is small (see the text). In the region $p/Et \gtrsim 10^{-2}\mu m^{-1}$, the collapse of the curves is indeed observed and the value of z_h found experimentally (black line) is well inside that region. (**C**) The ratio between the elastic energy and the work done by the indenter. The ratio reduces as the internal pressure increases and for $p/E \sim 0.01$ (the value relevant for *C. elegans*, see Fig. 3.1), the ratio is of the order of 1%, which shows that the work of the external forces is mostly spent to counter the internal pressure. In the simulations the length of the worm $L = 600\mu m$ and the radius of the indenting bead $R_b = 5\mu m$.

To gain insight on the consequences of the results in Fig. 3.2, we can use the shell equations (3.2). As in the case of spheres [23], it is convenient to rescale variables as $z = \gamma_z \tilde{z}\,, x = \gamma_x \tilde{x}$, etc., where

$$\gamma_w = \frac{pR^2}{S}\,, \quad \gamma_z = \gamma_x = \sqrt{R\gamma_w}\,, \quad \gamma_\phi = S\gamma_w^2\,, \quad \gamma_f = p\,. \tag{3.4}$$

These transformations reduce (3.2) to a non-dimensional form and the bending term proportional to B is multiplied by the factor $1/\tau^2 \equiv E^2t^4/p^2R^4$, where we have used the expressions of S and B given after (3.2). If $\tau \gg 1$, the coefficient of the bending term is small, and (with the possible exception of boundary layer regions) internal pressure and stretching of the shell provide the dominant balance in (3.2). Then, the only dependence on t which is left is via S, i.e. the dependence on E and t is through the combination Et. This observation suggests to plot z_h as a function of p/Et and Fig. 3.2 shows that curves with different t indeed collapse for large values of p/Et, which are those relevant for experiments.

We next analyzed the balance between elastic forces in the shell, the internal pressure and external forces that indent the body of the worm. We measured the elastic energy associated with the deformation generated by the indenter and compared it to the work by the external forces. Results of the simulations are shown in Fig. 3.2C. As intuitively expected, the ratio between the elastic energy of the shell and the work of the external forces reduces as p/E increases. The nontrivial quantitative point is that the ratio reduces quite rapidly : at $p/E = 10^{-2}$, the contribution of the elastic energy is of the order of 1%, showing that the dominant contribution comes from the internal pressure.

3.2.4 Influence of the boundary conditions at the lateral sides of the shell on its mechanical response

In the Section 3.2.2 we showed that the mechanical response of *C. elegans* can be described by modeling the nematode body as a pressurized cylindrical shell with free lateral sides. In this Section we analyze how the previous findings are modified if the lateral sides of the shell are closed with plugs. The goal of this analysis is to understand the role of the stress induced by lateral plugs of the nematode on its mechanical response.

We computed numerically the response of a closed pressurized cylindrical shell to an indentation experiment. The numerical procedure implemented is analogous to the one described in Section 3.2.2. The only difference consists of a different deformation induced by the internal pressure on the cylinder with no stress that can be calculated analytically. The action of the pressure on the plugs produces a longitudinal force on the shell whose magnitude does not depend on their structure (with the exception of a boundary layer next to the lateral sides). Without loss of generality we performed our simulations using semispherical plugs. Results of the simulations are shown in Fig. 3.3.

The introduction of the plugs influences the deformation profile which, for a given value of p/E, is larger with respect to that obtained in the case of cylinder with free lateral sides (Fig. 3.3A). Since the associated change in volume is bigger and the stiffness is dominated by internal pressure, the corresponding mechanical stiffness of the shell is larger (Fig. 3.3B). Our interpretation of these results is that the observed change in the mechanical behavior is produced by the longitudinal stress introduced by the plugs in the shell. In agreement with this interpretation we find that the difference between the response of the closed and the open cylinder decreases with the internal pressure (Fig. 3.3A, B).

The extension of the deformation profile increases with p/E but is wider than the one measured experimentally in all our simulations ($p/E \in [0, 0.02]$). The relative variation in the deformation profile becomes smaller as p/E increases and by extrapolation we exclude that for higher values of p/E the model prediction could match the experimental data. Moreover, even if for very large values of p/E the model could describe the experimental deformation profile, the corresponding prediction of the bulk modulus would be incompatible with data from [44].

The previous point can be shown as follows. If for a larger value of p/E the deformation profile matches the experimental measurements, the corresponding estimate for the internal pressure would be equal to that of Section 3.2.2 because it depends only on two experimentally determined quantities: the deformation profile and on the force indentation relation. Hence for every value of p/E that has not been simulated we derived the corresponding predictions of the Young's modulus and the bulk modulus assuming $p = 40k\text{Pa}$; results of the estimations are shown in Fig. 3.3D. The bulk modulus predicted by the model is always smaller than the experimental value. Since it is a decreasing function of p/E we conclude that also for larger values of p/E the prediction is not compatible with the experiments.

In summary, we showed that the description of the nematode body as an elastic shell with closed lateral sides cannot reproduce experimental results on the mechanics of *C. elegans*. Conversely, the same elastic model without plugs describes well the response of the nematode. Our results suggest that the longitudinal stress generated by the plugs is somehow relaxed in the worm, which most probably can be implemented through the annular structure of the cuticle.

3.2.5 Dependence on the size of the bead

Experimental results obtained in [9] show that the ionic current depends on the size of the indenting bead. This suggests that the bead size should influence the deformation profile. The goal of this Section is to test and validate this hypothesis.

Results for numerical experiments with indenters of different size are shown in Fig. 3.4. The bead size is indeed found to influence both the force-indentation relation (Figs. 3.4A-B) and the deformation profile (Fig. 3.4C) for p/E in the range of parameters relevant for biological experiments. Conversely, the effect of the bead size tends to vanish as p/E reduces, confirming again the crucial role of the internal pressure for the mechanics of the worm. As p/E increases, the relation force *vs* indentation w_0 is well described by a power law $F = f w_0^\alpha$, with $f \approx 0.9$ and $\alpha \approx 1.2$. Notice that this behavior is different from the linear relation found in [45]. The difference stems from the finite size of the indenter and a linear relationship is valid only in the limit of very small bead sizes.

The differences at large and low pressures that are visible in Figs. 3.4B-C are intuited as follows. The curvature of the deformation field at the indentation point increases with p/E until it matches the radius of the indenter. For bigger values of p/E, the shell cannot become any steeper as the bead is rigid : the deformation field adapts to the shape of the bead in the contact region, and the resulting region of contact enlarges with the radius of the ball R_b. The effects are clearly visible in the deformation profiles shown in Fig. 3.1C for different values of p/E. The radius R_b also controls the deformation field outside the contact region, as shown by the various profiles in Fig. 3.4C. In particular, R_b controls the mid-maximum extension of the deformation field, which is indeed found to scale as $z_h \sim R$ as shown in Fig. 3.4D. Conversely, as p/E reduces, the deformation field becomes shallower and shallower at the indentation point and the role of the radius of the ball tends to vanish (see Fig. 3.1C).

The modification of the deformation field that we just discussed is also reflected in the force-indentation relationship. Indeed, Figs. 3.4C-D show that the volume of the body to be deformed increases with the radius of the indenting ball and it takes then more force and work to achieve a given level of maximum indentation w_0. In formulae : the work $F dw_0$ done by the indenter roughly balances the contribution of the internal pressure $-pdV$ (the elastic energy is small, as discussed previously) and the force-indentation relation is then given by $F \propto -pdV/dw_0$. The larger volumes of deformation associated with balls of bigger radius enter the previous relationship and yield the nonlinear dependence shown in Fig. 3.4B.

3.2.6 Mechanics of soft *vs* stiff worms

Experimental investigations of *C. elegans* touch response are performed on dissected animals to reach the body of the touch receptor neurons and measure the ionic currents.

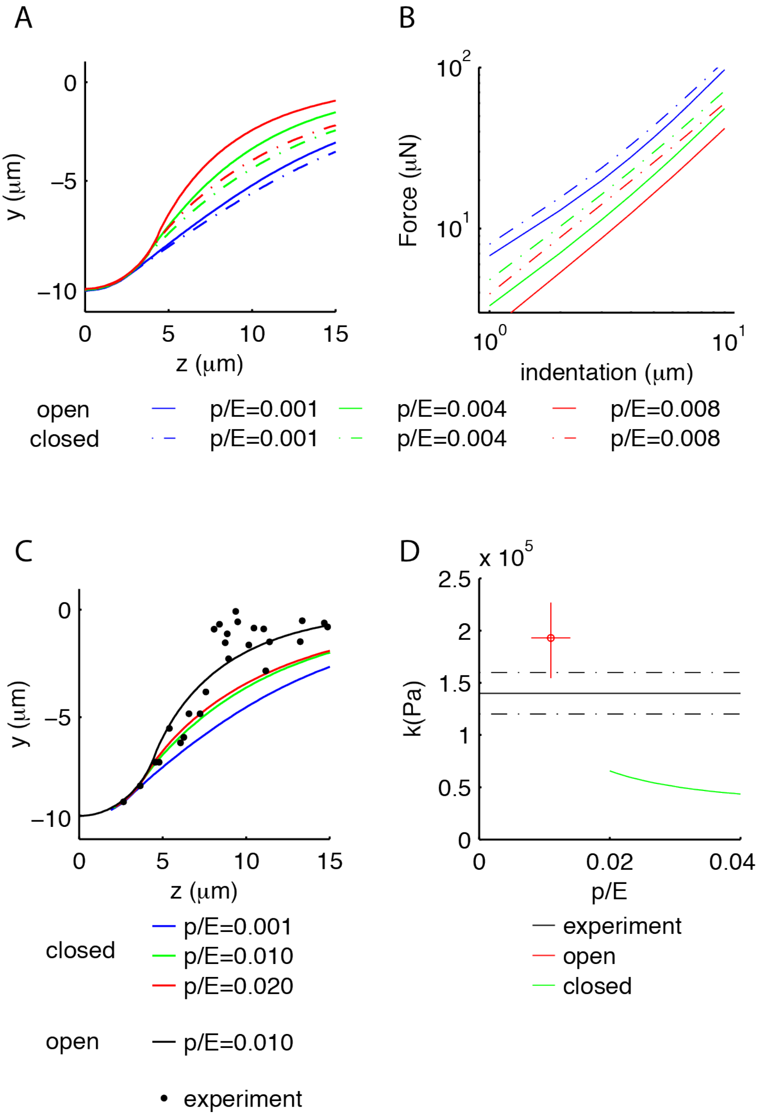

Figure 3.3: Boundary conditions at the lateral sides of the shell influence model predictions. (**A**-**B**) Comparison of the mechanical response of an open (dash-dot line) and closed (continuous line) cylinder. For a given value of p/E the deformation profile is larger (**A**) and the shell more stiff (**B**) if the lateral sides are closed. The difference between the results obtained with the two models increases with p/E. (**C**) Experimental and numerical deformation profiles of the worm along the longitudinal axis. Predictions of the closed cylinder (colored line) are not able to capture the experimental data for all the values of p/E simulated ($p/E \in [0, 0.02]$). (**D**) Experimental and theoretical bulk modulus. The value predicted by the cylinder with closed lateral sides decreases with p/E and is smaller than the experimental value for every p/E for which we did not compute the deformation profile. The results obtained in the case of free later sides for the deformation profile and the bulk modulus are shown for comparison. Parameters of the simulations are as in Fig. 3.1.

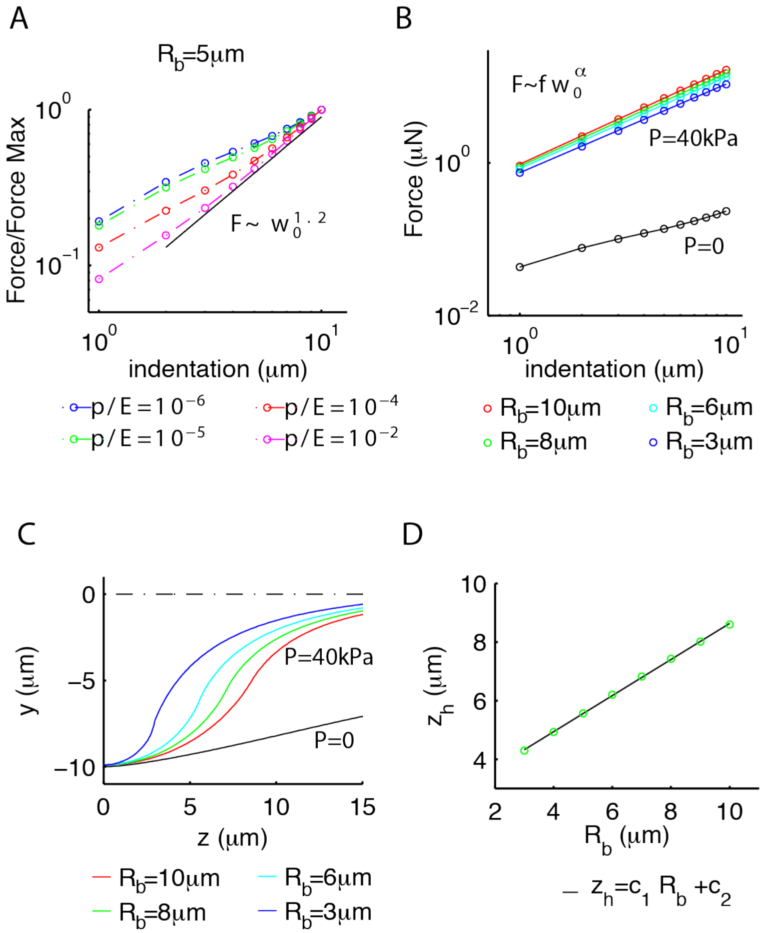

Figure 3.4: The effect of the size of the indenting bead on the mechanical response (**A**) The relation force-indentation for different values of p/E and a fixed size of the bead $R_b = 5\mu m$: as p/E increases, the behavior approaches the asymptotic scaling $F \propto w_0^{1.2}$. (**B**) The relation force-indentation for fixed $p = 40kPa$ and different radii R_b of the indenting beads. In strongly pressurized shells, the relation between the force F and the indentation w_0 (colored dots) follows a power law $F = fw_0^{\alpha}$ (solid lines) with the parameters f and α that depend on the radius of the bead, the internal pressure and the geometry of the shell. The exponent 1.2 in panel (**A**) is obtained for $R_b = 5\mu m$. For shells with no internal pressure, the force-indentation relation does not depend on R_b and the curves for the various R_b all collapse onto a unique curve (black dots). (**C**) Deformation fields produced by beads of different size. In pressurized shells, the deformation profile depends on the size of the bead (colored lines); conversely, in shell with no internal pressure, the deformation is the same for different values of the indenter size (black line). **(D)** The extension of the deformation field, as determined by the parameter z_h defined in the main text and in Fig. 3.2, scales proportionally to R_b.

As discussed in Chapter 2, two different dissection procedures were employed : parts of the gonad and the intestines were either released or not, thus better preserving the integrity of the body. The former dissection procedure yields softer worms in comparison to those produced by the latter procedure, as shown by the force-indentation experimental curves in Fig. 3.5. Worms prepared with the two dissection procedures were therefore called soft and stiff, respectively. The aim of this Section is to analyze the mechanical properties of the two types of worms.

Since the dissection of gonad and intestines in soft worms is performed away from the stimulation point, it is reasonable to assume that the dissection mostly affects the internal pressure and has smaller effects on the properties of the external shell. This suggests to analyze our model by keeping the Young's modulus E and the thickness t fixed and modifying the internal pressure p. Results of the corresponding simulations are shown in Fig. 3.5.

The slope of the force-indentation relation decreases with the internal pressure and the value that better describes experimental data for soft worms is $p = 2$kPa, i.e. pressure is reduced to about 5% of the value found previously for stiff worms. We also observe that the dissection procedure results in a higher level of variability with respect to stiff worms, with a range of pressures going from 0.4 to 8 kPa. Consistently with this observation, fluctuations in the touch receptor currents in stiff worms were indeed found to be weaker than in soft worms (see Chapter 1).

The current in touch receptor neurons is different for soft and stiff worms if expressed as a function of the pulse force yet it is approximatively invariant if expressed in terms of the indentation depth (see Chapter 1). The results of our simulations rationalize this observation in terms of the mechanical stimulation. Indeed, Figs. 3.5B-C show that the deformation profiles produced by a fixed-force pulse changes substantially with the internal pressure whilst variations are much weaker if the indentation depth is fixed.

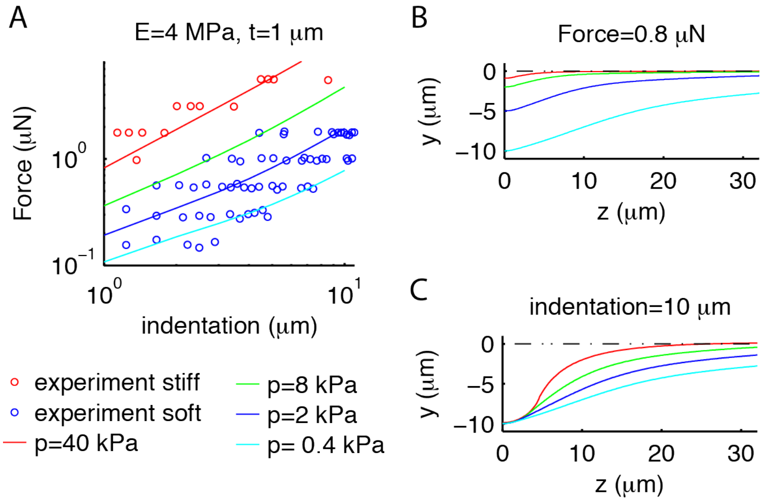

Figure 3.5: Comparison of the mechanical response of stiff and soft worms (**A**) Experimental (dots) and theoretical (lines) force-indentation relations. An internal pressure $p = 2$kPa gives the best description of the pooled data for soft worms. The strong variability in the experimental data corresponds to cylindrical shell with internal pressures that range from 0.4 to 8 kPa. (**B**) and **(C)**: Predicted deformations to stimulations with fixed force and fixed indentation, respectively.

3.2.7 The gluing of the nematode onto the plate influences its mechanical response

The nematode body is glued on a plate during indentation experiments. As mentioned in Section 3.2.1, the volume of the glue strongly limits the displacement of the body in the region in which the glue is applied. In the previous Sections we assumed that the glue was applied to the whole lower half of the body. The goal of this Section is to analyze how measurements on mechanical properties of the worm are modified by changing the way in which the nematode is glued. The corresponding predictions could be tested by indentation experiments.

We consider the case in which only the line of contact with the plate is glued, i.e. the opposite situation with respect to the case previously investigated. In the model this corresponds to a boundary conditions in which only the south pole of the cylinder (the line of contact with the plate when the cylinder is not indented) is clamped. Using this boundary condition we computed numerically the response of the shell to an indentation experiment, results are shown in Fig. 3.6. The shell stiffness is smaller whilst the longitudinal deformation is larger respect to the case where the lower half of the cylinder is clamped. The fact that the stiffness is smaller even if the longitudinal deformation profile is larger can be understood by looking at the deformation along the orthogonal direction (Fig. 3.6C). The shell shows a global deformation that features an expansions of the whole lower half of the body. This mode of deformation is forbidden with previous boundary conditions where the worm was glued over its entire lower half.

The prediction is that the stiffness of the worm should decrease with the region of the nematode body that is glued to the plate.

3.2.8 Mutations in the cuticle effects on the mechanical response of *C. elegans*

Mutations in the cuticle have been used to investigate experimentally its role in the mechanical properties of *C. elegans* [38, 44]. In this Section we use our model to characterize the effects of those mutations and analyze the diverse experimental results that have been reported in the literature.

We shall describe the effects of mutations in the cuticle through variations in the stretching stiffness S, which is the only relevant parameter of the model related to the properties of the external layers of the nematode. We assume that mutations do not affect the internal pressure of the nematode. As pointed out in [38], this is reasonable because the genes involved, e.g. the genes *dpy-5* and *lon-2* discussed below, do not affect transport proteins likely to regulate osmotic pressure. In the model the size of the pressurized shell is obtained by starting from an unpressurized shell that is stretched by the internal pressure. We shall assume that the size of the unpressurized shell is the same for all mutants. In the biological system it is possible that mutations in the cuticle affect the development of the nematode and hence its body structure. In the model this could result in unpressurized shells of different size but we will neglect this effect in these notes.

We analyzed numerically and analytically the dependency on S of different mechanical properties; results are shown in Fig. 3.7.

We first studied the effects of variations in S on the geometry. Mutations change both the length and the radius of the shell; the radius increases whilst the length decreases with S (Fig. 3.7A). This is due to the fact that the internal pressure deforms the shell by increasing (decreasing) its radius (length) with respect to the unpressurized condition and the amplitude of the deformation decreases with the stretching stiffness S. Note that in the case where the lateral sides of the shell are closed with plugs, both the length and

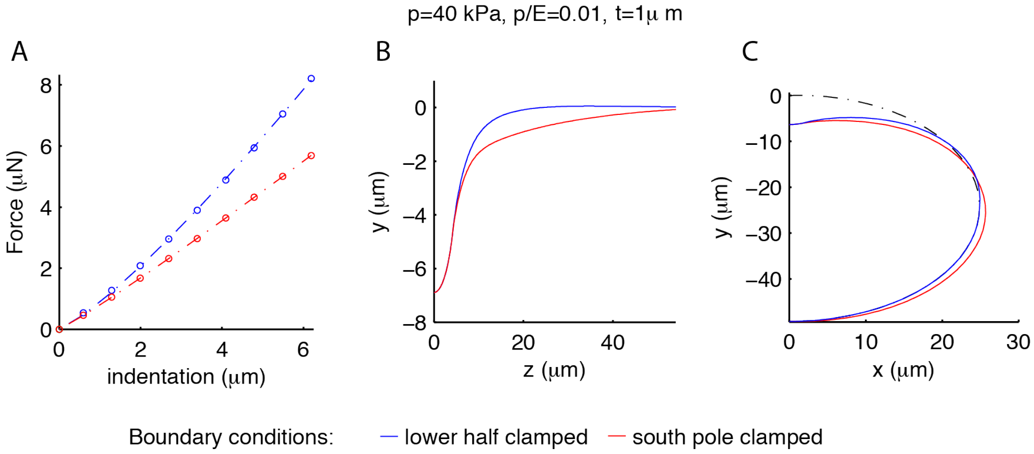

Figure 3.6: Influence of the experimental set up on the mechanical response of the worm. We computed numerically the mechanical response of the shell with two different boundary conditions corresponding to two different way of attaching the nematode onto the plate of the experimental set-up. In the first case (blue) the lower half of the cylinder is clamped whist in the second case (red) only the line of contact with the plate (south pole) is clamped. (**A**) Force indentation relation (empty dots) obtained for the two boundary conditions investigated. The relation follows a power law $F = f w_0^\alpha$ (dash-dotted lines) with best fit parameters $f = 0.89$, $\alpha = 1.21$ (blue), $f = 0.80$, $\alpha = 1.08$ (red). The shell stiffness is greater when the lower half of the shell is constrained. The deformation profiles along the longitudinal (**B**) and orthogonal (**C**) directions are wider when only the south pole of the shell is fixed. Note that in this case also the lower half of the shell is deformed in the orthogonal direction. The undeformed geometry (black dash-dotted line) is shown for comparison.

the radius are increasing functions of S (Fig. 3.7A). This is due to the fact that the force exerted by the internal pressure on the plugs stretches the shell along the longitudinal direction of the cylinder.

Mutations in the cuticle affect the stiffness of the cylinder in response to indentation experiments. Numerical results on the dependency on S of the stiffness parameters f and α (introduced in Section 3.2.5) are shown in Fig. 3.7. It is observed that the stiffness of the shell increases with S. This behavior is due to two contributions which influence the deformation field and hence the change in volume that drives the stiffness. First, if the external radius of the pressurized shell is kept constant the deformation field is wider (see Fig. 3.1C). Second, the radius of the shell becomes smaller as S increases (see Fig. 3.7C) which leads to a larger deformation field.

Finally, we found analytically that the bulk modulus increases with S (Fig. 3.7B).

The parameter S is not measured during the experiments. Hence, in order to compare the model predictions with experimental results, we use the external radius of the pressurized shell as a proxy to differentiate mutants. In this formulation the model predicts that every mutation in the cuticle which increases the worm radius decreases its length, stiffness and bulk modulus. This features are in qualitative agreement with what has been observed experimentally [38, 44]. We point out that if the lateral sides of the shell are closed with plugs, the length of the shell is an increasing function of its radius; this qualitative discrepancy provides another evidence that the stress induced by the lateral sides of the cylinder on its external layer must somehow be relaxed in the real worm.

It is observed that the deformation measured in the length of the mutants in [38] is always larger than our prediction. This quantitative discrepancy could be explained by taking into account that in the biological system the Young's modulus is likely not isotropic; in particular because of the annular structure of external layers of the body we expect that the stiffness should be smaller in the longitudinal direction respect to the orthogonal direction. Another possibility is that the discrepancy comes from the above mentioned effects of mutations on the development of the worm.

We note that the radius of *lon*-2 mutants in [38] is about 25% smaller respect to the wild type. In our model for every modification in S the radius cannot become smaller than the radius of the unpressurized shell, which corresponds to a decrease in the radius of about 20%. In [38] the size of the wild type worm is smaller than what we assumed in deriving the model parameters here (13 μm *vs* 25 μm), however this cannot explain the discrepancy because the relative change in radius becomes smaller as the radius of the shell decreases. The discrepancy could be explained by a fluctuation in p/E, since the relative change in radius grows with p/E, or also by the previously mentioned effects in the development of the worm that we have neglected.

In Fig. 3.7C-D we compare theoretical predictions on shell stiffness and bulk modulus with experimental data from [38, 44]. The measurements are in quantitative agreement with theoretical predictions. Moreover, the model predicts that a bulk modulus measured in *lon*-2 mutants should show a significant difference respect to the wild type.

In the literature experiments on the mechanical response of *C. elegans* have led to conflicting interpretations [38, 44]. On the one hand, the shell stiffness is found to depend on the properties of the cuticle [38] ; on the other hand, measurements of the bulk modulus seem invariant with respect to mutations in the cuticle [44]. Our analysis shows that mutations in the cuticle should affect the mechanical response of the nematode both in the response to indentation experiments and in the bulk modulus. Our model suggests that in [44] no effect of mutations in the cuticle has been found to affect the bulk modulus only because of the type of genes that have been investigated.

3.3 Discussion

A fundamental step toward the understanding of the sense of touch is to discover the molecular basis of the single channel gating mechanism. In principle the model described in Chapter 2 could be used to investigate this aspect since different hypothesis on the molecular basis result in different predictions on the neural current. However, because of the mean field approximation used, the model entangles effects of single channel and population properties. For instance the symmetry in the neural response could be a property of the single channel or be realized at the population level. In order to investigate single channel properties a description beyond mean field of the stimulus acting on the channels is needed. In this Chapter we discussed some preliminary work aiming to obtain this beyond mean field prediction.

The worm body is described as a pressurized elastic cylindrical shell. Parameters of the elastic model were inferred using experimental data on the deformation profile and the force-displacement relation in stiff worms. The model were validated by the prediction of the values of the bulk modulus and the internal pressure, which are both in agreement with independent experimental measurements. We found that the deformation field produced by a prescribed force depends strongly on the internal pressure of the worm. Conversely, worms with different internal pressure have similar deformation fields when the indentation is fixed. This observation is consistent with experimental

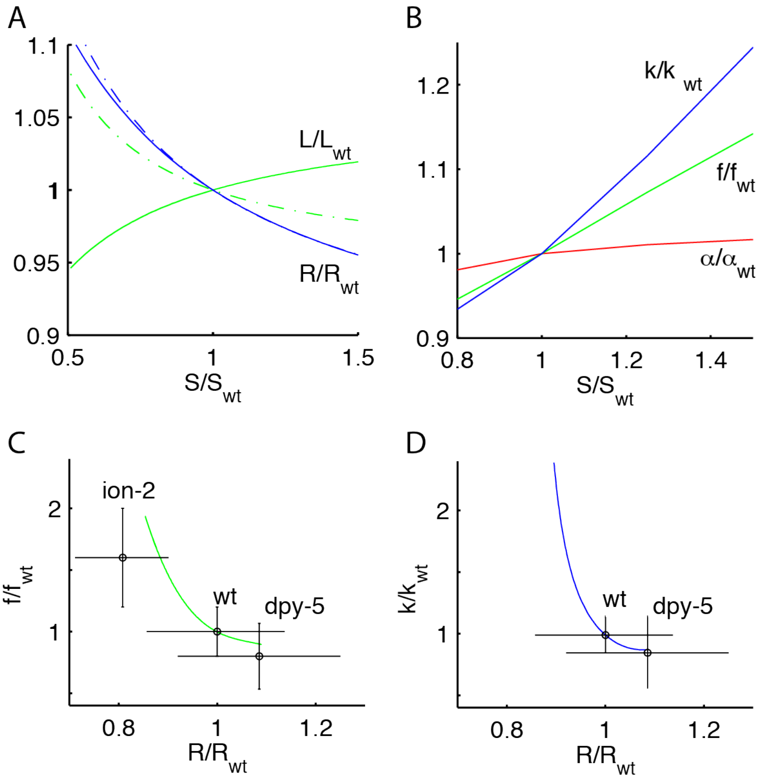

Figure 3.7: Changes in the nematode mechanical properties with respect to the wild type, which are caused by mutations in the cuticle. Mutations in the cuticle are represented in the model through changes in the value of the stretching stiffness S with respect to the wild type S_{wt}. **(A)** As S increases, the geometry of the pressurized cylinder is modified: the length increases and the radius decreases (continuous lines). The prediction with the shell closed on the lateral sides is different (dash dotted line), in particular the length of the cylinder is an increasing function of S. **(B)** Effects on the mechanical response of the cylinder due to a modification of S. As S increases the bulk modulus k (blu line) and the coefficients f (green line) and α (red line) of the force-indentation relation increase. **(C-D)** Comparison of theoretical predictions for f and k as a function of the radius of the shell with experimental measurements [38, 44]. Since in [44], the radius of the mutants was not indicated, we used the values in [38]. The theory predicts that *Ion*-2 mutants should have a bulk modulus significantly different respect to that of the wild type.

observations described in Chapter 1 about soft and stiff worms and the dependence of the response on the indentation depth rather than the applied force. Based on our analysis we predict a more general joint dependence of the response on the internal pressure and the indentation. This prediction could be tested by measuring the neural response of touch receptor neurons in worms.

The analysis performed here is also relevant to understand the mechanics of *C. elegans* body. In particular, a question that have been longly debated in the field regards which factors shape the stiffness of the nematode body. Here we showed that the stiffness of *C. elegans* body is dominated by the internal pressure and the coefficient of the bending term in the elastic energy is small. We also discussed the effects of mutations in the cuticle on the mechanical response and predict how they should affect the bulk modulus in a way that is experimentally observable. The main results that lend to experimental verification are the dependencies of the force-indentation relation and the deformation profile on the size of the indenter and on the way the nematode is glued on the plate of the experimental set-up.

The future direction of this research is to use the description of the mechanical response of the worm body to make predictions on the neural current produced in indentation experiments, this will provide a general method to differentiate between different molecular structures and understand which describes the gating of ionic channels. A long term goal of this research is the study of other types of touch receptor neurons that show the same dynamical response, such as Meissner corpuscles in mammalian skin or campaniform sensilla in Drosophila. The proposed mechanism highlighted the fundamental elements for fast adapting and symmetric dynamics and is compatible with several molecular embodiments so it could be applied in different conditions.

CHAPTER 4

Complete coverage of space favors modularity of the grid system

4.1 Neural basis of spatial representation

Animals are able to orient them self and navigate in an environment. Tolman [46] suggested that this ability resides on an internal "cognitive maps" that flexibly represent the overall spatial relationships between landmarks in the environment. The research on the neural basis of such map started in the 70s with the discovery of Place Cells by O'Keef [47]. He was looking at the neural activity of single neurons in the rat hippocampus while the animal was moving freely in a confined environment where food was scattered everywhere. He found that the single cell activity is related to the spatial position of the animal. In particular each neuron is active in a specific place of the environment (Fig. 4.1); the preferential location is randomly associated in different neurons. Since the spatial position of the animal can be decoded by looking at the population activity of these neurons, the system forms neural representation of space. In the last forty years research in this field led to the discovery of different components of this neural map such as head direction cells [48, 49], border cells [50], speed cells [51]. The research described in the next Chapter focuses on one particular type of neurons called grid cells [52]; in the following Section we give a detailed description of these neurons.

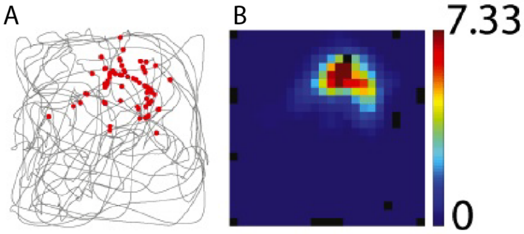

Figure 4.1: Spatial activity of place cells in the rat hippocampus. (**A**) Trajectories (black lines) followed by rat free to move in a square environment and the positions at which a single neuron was active (red dots). (**B**) Firing field as a function of the animal position. The activity of a neuron is localized in a specific place of the environment.

Grid cells have been uncovered in the main input to hippocampus, a structure known as the medial entorhinal cortex (MEC) [52]. They respond when the animal occupies one of the vertices of a triangular grid tessellating space (Fig. 4.2). Locally within MEC, grid cells share the same orientation and periodicity, but vary randomly in phase [52]. The spatial period of the grid increases along the dorso-ventral axis of the MEC [52, 53, 54].

Grid cells are organized in modules – the grids of cells within a module are clustered around a discrete period [53, 54], and share similar orientations and ellipticities while varying in spatial phase[54]. Experimentally, there is a power-law relation between the periodicities of different modules.

It is believed that grid fields provide relatively rigid coordinates on space based partly on self-motion and partly on environmental cues [55]. This raised the questions of how the grid code could be read by the brain and which might be the advantage of this peculiar structure.

A functional rationale for this organization has been given in [56], where it has been shown that the triangular structure of the grids could be explained by assuming that the system minimizes the number of neurons required to encode location with a given resolution. We ask :

Why is the grid system modular in the first place?

Here, following [56], we will regard the grid system as providing a hierarchical code for location where smaller periods provide precision, larger periods resolve ambiguity, and each module must separately cover the range over which the grid should operate. We will show that variability in the period, orientation and ellipticity effectively randomizes the relative phases of firing fields, and eventually leads to failure of spatial coverage. Larger variability entails a smaller physical range that can be covered without gaps. Hence, optimizing spatial coverage gives a functional argument for reduced variability and for the observed comodularity of the grid cells. Our arguments also predict a scaling law that relates the number of neurons in a grid module and its period. In particular, we predict that more neurons are required at small grid scales than at larger ones. Any grid coding or decoding scheme will require complete coverage, so the results of the analysis do not depend on details of a particular coding scheme and apply generally.

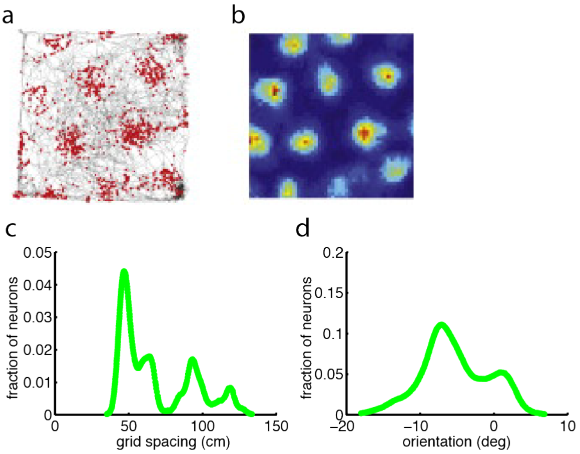

Figure 4.2: Structure of grid cells in the rat medial entorhinal cortex. (**a**) Activity of a single grid cells (colored dots) superimposed to the trajectories followed by the rat (black lines) and its firing field as a function of position (**b**). Fraction of grid cells with a given period (**c**) and orientation (**d**).

4.2 A model of grid cell activity

Grid cells [52] have circular firing fields with diameter ℓ, arranged in a regular triangular grid with period λ (Fig. 4.3). The grid activity is also characterized by its phase ϕ, i.e. a shift with respect to a reference point, and an orientation, i.e. an angular displacement θ with respect to a reference direction. Grid patterns can present approximately isosceles, rather than equilateral, triangles (Fig. 3 of [54]; also see [53, 50]). The aspect ratio of these triangles is quantified through an "ellipticity" parameter ϵ, defined below. The firing fields of grid cells form smooth lumps, but after thresholding for noise, we can regard them as being active inside a localized region and inactive outside. For the purpose of analyzing coverage of space, we will treat the activity as being uniform inside the active region. Noise and firing inhomogeneity inside the active region can only degrade the uniformity of coverage relative to this model. Thus, we will be able to use it to derive bounds on how well a given grid architecture can cover space.

The activity of grid cells with the above properties can be expressed mathematically as

$$a(\mathbf{x}) = \sum_{n,m\in\mathbb{Z}} \chi\left(\frac{2|\phi + R(\theta)\,[n\mathbf{v} + m\mathbf{u})] - \mathbf{x}|}{\ell}\right) , \tag{4.1}$$

where $\mathbf{x}$ is the vector locating the position of the animal in two dimensions, $\mathbf{v} = \lambda_1(\cos(\beta), \sin(\beta))$ and $\mathbf{u} = \lambda_2(1, 0)$ are the elementary vectors that generate the grid, λ_2 and λ_1 are the lengths of these two vectors, and n and m are integers indexing the different vertices of the grid. $R(\theta)$ is an overall rotation of the grid by an angle θ and the angle β describes the relative rotation of the grid basis vector $\mathbf{v}$ relative to $\mathbf{u}$. The activity of an equilateral, unrotated triangular grid has $\lambda_1 = \lambda_2 = \lambda$, $\beta = \pi/3$ and $\theta = 0$. The set of the six vertices defined by the triplet $\mathbf{u}$, $\mathbf{v}$, $\mathbf{u} - \mathbf{v}$ and their opposite vectors forms an hexagon that can be inscribed into an ellipse centered at the origin. We assume that transformations of the grids are such that one of the axes of ellipses remains parallel to the direction of the vector $\mathbf{u}$. As derived in Appendix A.1 this corresponds to grids made of isosceles triangles with $\lambda_1 \cos(\beta) = \lambda_2/2$ and $\cos(\beta) = 1/\sqrt{1 + 3\epsilon^2}$, in which ϵ is the ellipticity of the ellipse, defined as the ratio between its two axes [54], $\epsilon = 1$ corresponds to a grid with equilateral triangles. (We checked that our broad conclusions also hold for more general transformations that correspond generally to non-isosceles deformations of grids, see Appendix A.1.) Finally, since we want to simply analyze whether a neuron is active or not at a given point (as opposed to the strength of activity), we take the function $\chi = 1$ when its argument is < 1 and 0 otherwise.

Within a module, grid cells with similar grid spacing have similar orientation, ellipticity and firing field size [54]. However, there is variability. We quantified the variability using experimental data reported in [54]. For each animal in this dataset we fit the distribution of grid spacing and orientation using a different Gaussian for each module (details in Appendix A.2). We find roughly constant standard deviations for grid spacing (λ) and orientation (θ) across modules of $\sigma_\lambda \sim 6$ cm and $\sigma_\theta \sim 0.03$ rad. The standard deviation of ellipticity is harder to estimate because of limitations of the data, and so we will treat it as a free parameter. Across animals, the ratio of grid spacing of consecutive modules is 1.42 ± 0.17 [54]. Furthermore, the ratio between firing field width and grid spacing for each neuron is $\sim 1.63 \pm 0.035$, i.e. grid cells with different periods look like globally rescaled versions of one another [57]. We will incorporate these facts into our analysis. Assuming that there are 10 grid modules, and that the smallest one has a period of about 40cm, the ratio σ_λ/λ changes from 0.01 to 0.15.

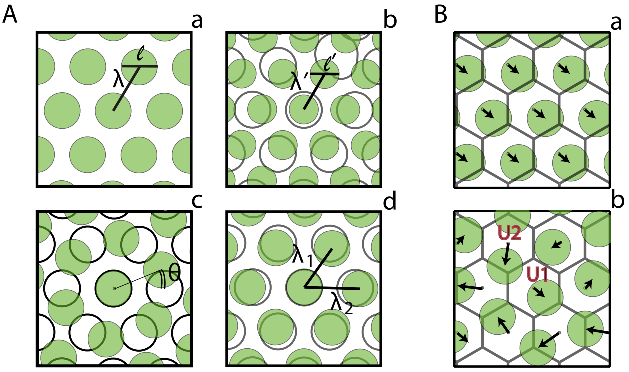

Figure 4.3: Deformations in grid parameters induce dephasing. (**A**) Spatial activity of a grid cell and its possible deformations: regular grid (**a**), dilation (**b**), rotation (**c**) and ellipticity transformation (**d**). The activity after transformation (green) is superimposed on the reference activity (black circumferences). (**B**) Using a set of grid parameters we divide the space into unit cells represented by black hexagons. A neuron with the same set of grid parameters (**a**) has constant relative phase (black arrows) in each unit cell. A neuron with different grid parameters (**b**) has different phases in different unit cells, e.g. here the center of the unit cell is covered by a firing field in U1 but not in U2.

4.3 Dephasing and decorrelation of neuronal activity

In order to cover an environment with grid cells, there has to be at least one active neuron at each point. If grid cells in a module differ only in their phase, perfect periodicity implies that once a unit cell is covered, all of space is covered. Below, we show that this is not longer true if the characteristics of the grid geometries within a module are variable.

The grid cells in a module will have an average orientation (θ), ellipticity (ϵ) and period (λ). Starting with a lattice with these parameters, we divide the plane into unit cells defined as the locus of points in space that are closer to each lattice point than to any of the other lattice points. For each unit cell K we define the relative phase ϕ^K of a particular grid as the vector connecting the center of the unit cell to the center of the closest firing field, as shown in Fig. 4.3. If the grid parameters are different from those of the average grid, the relative phase changes from one unit cell to the other (a phenomenon that we call "dephasing"). Because of dephasing, if the firing field of a neuron covers the center of a unit cell $U1$ it may not cover the center of another unit cell $U2$ (see Fig. 4.3).

To quantify the effect described above, we compute the correlation coefficient between the number of neurons that are active at the center of two unit cells. Consider a set of neurons whose grid parameters are drawn from Gaussian distributions with mean period λ, orientation θ, and ellipticity $\epsilon = 1$ and corresponding standard deviations σ_λ, σ_θ and σ_ϵ. We compute the correlation between the numbers of neurons $n(x)$ and $n(y)$ active at different points x and y, by averaging over statistical realizations (Fig. 4.4). When there is no variance in the grid parameters between neurons, the correlation is independent of separation, and equal to one. Equivalently, the number of neurons with a certain relative phase is the same for all unit cells. When we introduce variance in the orientation, period and ellipticity, the correlation decreases rapidly with separation. The smallest grids in the entorhinal cortex have periods λ in the range $10 - 40$ cm. Fig. 4.4

then shows that that the correlation length will be in the meter scale, well within the behavioral range of a few tens of meter where the grid system is expected to support spatial behavior, based on studies of rat homing ranges[58, 59, 60].

Figs. 4.4A,B,C show that the correlation between the number of active neurons at two separated points declines systematically with separation in the grid lattice. We characterize this decline in terms of a *correlation length* $\mathcal{L}$, defined as the distance at which the correlation drops to $1/e$. Appendix A.3 shows that our results for scaling relations do not depend on the specific choice of this threshold. The correlation length decreases with the variance in the orientation, ellipticity and periods of the grid cells. For different values of σ_λ/λ, σ_ϵ and σ_θ we measure the correlation length (Fig. 4.4D,E,F). A numerical analysis of these results shows that the correlation length decreases with variability in the grid parameters and the qualitative behaviour is the same for σ_θ, σ_λ/λ and σ_ϵ. In particular, when only one of the three variances, say σ_θ, is varied, while the other two are fixed, $\mathcal{L}$ is a monotonically decreasing function that behaves as λ/σ_θ when $\sigma_\theta \gg \sigma_\lambda/\lambda$, σ_ϵ and as $\lambda/\left(\sigma_\theta + \text{constant}\right)$ when $\sigma_\theta \ll \sigma_\lambda/\lambda$, σ_ϵ, with a constant that depends on σ_λ/λ and σ_ϵ.

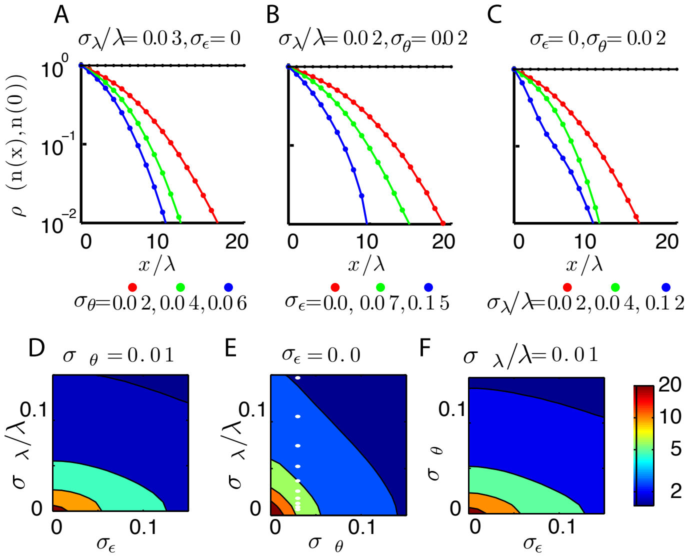

Figure 4.4: Variability induces decorrelation in grid cells activity. The correlation coefficient of the number of neurons active at the center of two unit cells along the line $\vec{x} = n\lambda(1, 0)$ in the grid lattice with $n \in \{0, 1, \ldots\}$ for different standard deviations of the period, orientation and ellipticity. In the plots $x = |\vec{x}|$. In each plot of the first row there are three colors representing different values of one of the variances (orientation (**A**), period (**B**), ellipticity (**C**)) while the other two are fixed. Larger variances lead to a more rapid decrease in the correlation as a function of separation. (See Appendix A.3 for a discussion of the bump in the blue line in panel C.) The correlation length depends on three variances which we varied in pairs obtaining contour plots for fixed variance in ellipticity (**D**), orientation (**E**) and period (**F**). The white points in panel (**D**) correspond to the average variance in orientation σ_θ and period σ_λ in the modules measured in[54]. Here we assumed 10 modules with constant variances and extrapolated the values of σ_λ/λ assuming a smallest scale of 40cm and a constant ratio between scale of 1.42. In the simulations the mean ratio of the grid period and firing field size is $\lambda/\ell = 1.63$, the mean grid orientation angle is $\theta = 0$, and the mean grid shows equilateral triangles (ϵ=1). Here and in the following figures, the 95% confidence interval error bars are smaller than the size of the dots representing each data point.

4.4 Coverage drives modularity

In order to cover an environment with a set of grid cells, there has to be at least one active neuron at every point. Above, we defined a correlation length $\mathcal{L}$ that characterizes the scale of distance beyond which the numbers of active neurons become approximately independent. In terms of this scale, a region of size R can be thought of as being composed of $R^2/\mathcal{L}^2$ regions where the probabilities of coverage are roughly independent of each other. If each of these is covered with probability p, the probability P of covering the whole environment is

$$\log(P) = \gamma \frac{R^2}{\mathcal{L}^2} \log(p)\,, \tag{4.2}$$

where γ is a constant that depends on the geometry of the system. The covering probability P of the whole environment depends on variability since the correlation length $\mathcal{L}$ does. To test this analytical estimate, we numerically analyzed the covering probability of a circular environment of radius R by N neurons whose periods and orientations are drawn from Gaussians with means λ, θ, $\epsilon = 1$, standard deviations σ_λ, σ_θ, σ_ϵ, and uniformly distributed phases. We then checked if every point in the environment is covered by at least one grid cell and we averaged over realizations. The results confirm our analytical estimate Eq. (4.2) for the covering probability P (Fig. 4.5), with a proportionality constant $\gamma = 0.804$.

Within a single volume of side $\mathcal{L}$, the correlation between the number of active neurons $n(x)$ and $n(y)$ approaches one if $|x-y|/\mathcal{L} \ll 1$ and decreases continuously as the distance increases. We numerically investigated the dependence of p, the probability of covering a correlation volume of linear size $\mathcal{L}$, on the probability of covering a unit cell p_{uc}; results are shown in Appendix A.4. As seen in Fig. 2, over a range of orientation, period and ellipticity variances that includes the experimentally measured values, the correlation length lies in the range, $\mathcal{L}/\lambda \lesssim 20$. We carried out a numerical fit within this range, and found that the probability p is well described by

$$\log(p) = \mathcal{K}\left(\mathcal{L}/\lambda\right) \log(p_{uc})\,, \quad \mathcal{K}\left(x\right) = c_1 + c_2 \log(x)\,, \tag{4.3}$$

where $c_1 = 0.73$, $c_2 = 13$ and p_{uc} is the covering probability of a unit cell. Combining the Eqs. (4.2) and (4.3), we obtain for the probability of covering the environment:

$$\log(P) = \gamma \frac{R^2}{\mathcal{L}^2} \mathcal{K}\left(\mathcal{L}/\lambda\right) \log(p_{uc})\,. \tag{4.4}$$

We tested this formula as follows. For a given number of neurons N we measured p_{uc} through numerical simulation, and then used the formulae for $\mathcal{K}$ and γ from above to predict the coverage probability P. We then numerically computed P through repeated simulations and found the agreement shown in Fig. 4.5.

Fig. 4.5 and Eq. (4.4) show that the covering probability of a region increases with the correlation length. In this sense, a set of grid cells with a larger correlation length is more efficient, because with the same number of neurons, and hence a fixed probability, p_{uc}, of covering the unit cell, it will have fewer gaps. Since the correlation length decreases with the standard deviations of orientation, ellipticity and period increase, we conclude that coverage drives modularity – grid cells in a period module should also have similar orientations and ellipticities as observed experimentally [54]. We have checked that the same conclusion, i.e. coverage drives modularity, also holds for grids that are non-equilateral on average, as detailed in Appendix A.1.

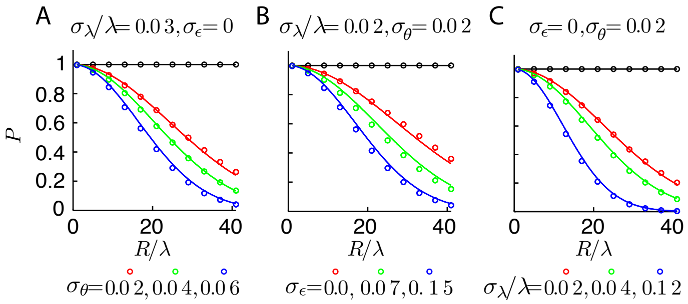

Figure 4.5: Covering probability decreases with variance and environment size. Covering probability of a circular environment of radius R is computed for environments of different size and different variances for orientations, ellipticity and grid period. As in Fig. 4.4, in each plot there are three colors representing different values of one of the variances (orientation (**A**), period (**B**), ellipticity (**C**)) while the other two are fixed. The covering probability decreases as variances increase. Results of the numerical simulation (colored circles) match theoretical predictions (continuous line) obtained by Eq. (4.4). Simulation parameters are as in Fig. 4.4 with $N = 30$ neurons in the module.

4.5 Gaps decline exponentially with the number of neurons

We showed above that the probability of covering a range R is given by equation (4.4) where the factor p_{uc}, i.e. probability of covering a unit cell, contains the dependence on the number of neurons. Given the experimental evidence that phases of grid cells are randomly distributed [52], the covering probability of a unit cell can be directly computed.

Let us write

$$p_{uc} = 1 - \exp\left(\mathcal{F}\left(N\right)\right) , \tag{4.5}$$

where $\exp\left(\mathcal{F}\right)$ is the probability of having at least one gap, i.e. of *not* covering the unit cell. The functional form of $\mathcal{F}$ can be computed analytically in one dimension:

$$\mathcal{F}_{1D}\left(N\right) = \alpha_{1D} N + \beta_{1D} \log(N) + \gamma_{1D} , \tag{4.6}$$

$$\alpha_{1D} = -\gamma_{1D} = \log\left(1 - \frac{\ell}{\lambda}\right) , \quad \beta_{1D} = 1 , \tag{4.7}$$

as shown in [61] (see also Appendix A.5). Here, ℓ and λ are the grid field width and the grid period respectively. Eqs. (4.5) and (4.7) show that the probability of having a gap declines exponentially in the number of neurons. In fact, this will be true for a grid system in any number of dimensions as shown by the following general argument. Imagine first that N neurons cover a unit cell of a d-dimensional grid, leaving one gap. Suppose we add an additional neuron which has a random phase. There is some probability $h < 1$ that it will fail to overlap the gap. If we add Q additional neurons independently, the probability that they all miss the gap is h^Q. Because of this, the probability that the gap persists will decline exponentially with the number of added neurons. In detail, there is some probability of partial coverage with each additional neuron and this leads to subleading terms of $O(\log N)$ and $O(1)$ in (4.6).

Thus, when the number of neurons participating in a two-dimensional grid module is large, we expect that $p_{uc} \sim 1 - \exp\left(\alpha_{2D} N\right)$, where $\alpha_{2D} < 0$ is a factor that does not depend on N. In the opposite limit, when N is smaller than the area of the unit cell divided by the area of the firing field, coverage cannot be achieved at all and hence $p_{uc} = 0$. We confirmed these expectations numerically for the two dimensional case (Fig. 4.6). As in one dimension, the parameter α only depends on the ratio of the grid field width (ℓ) and the grid period (λ). This is because α controls the probability of gaps in covering a unit cell with grid fields, whose respective sizes are λ and l. Dimensional analysis then shows that the dimensionless quantity α can only depend on a ratio of the two parameters λ and ℓ which both have dimensions of length.

Putting everything together, the probability of covering a two dimensional circular region with a radius R is estimated to be

$$\log(P) = \gamma \frac{R^2}{\mathcal{L}^2} \mathcal{K}\left(\mathcal{L}/\lambda\right) \log(1 - e^{\mathcal{F}(N)}), \tag{4.8}$$

as confirmed by numerical simulation (Figs. 4.5, 4.6). Thus we find that the probability of gaps in coverage of a unit cell declines exponentially in the number of neurons in a module. However, the probability of gaps in coverage of a range R increases exponentially as $(R/\mathcal{L})^2 \mathcal{K}\left(\mathcal{L}/\lambda\right)$ where $\mathcal{L}$ is a correlation length which decreases as the variance in a module increases. In the next section, we balance these effects against each other to estimate the number of neurons required to cover space in modules of different mean periods given the measured variability.

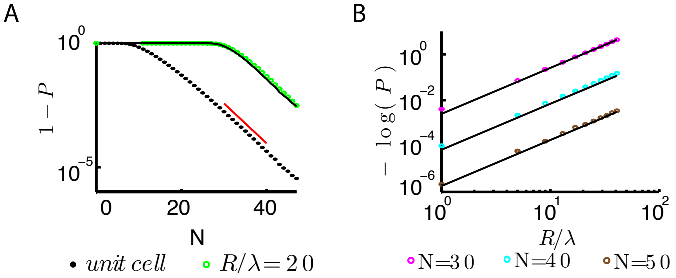

Figure 4.6: Covering probability increases with the number of neurons. (**A**) The probability $1 - P$ of having gaps is computed numerically for a unit cell (black dots). This result is used to predict through Eq. (4.8) the probability of having gaps for an environment of size $R/\lambda = 20$ (black line), the prediction matches the numerical simulations (green dots.) The function $1 - P$ declines exponentially with N and is asymptotic to $\exp(-0.4N + 5.5)$ (red line). (**B**) Covering probability computed numerically for different environment size R and number of neurons N. Results of the simulations (colored dots) match theoretical predictions (black lines) obtained with Eq. (4.8). Simulations parameter are λ/ℓ =1.63, $\sigma_\theta = 0.04$, $\sigma_\lambda/\lambda = 0.08$, $\sigma_\epsilon = 0$.

4.6 Prediction: smaller period modules need more neurons

Eq. (4.8) describes a relation between the number of neurons (N_i) and the parameters of the i-th module. Since the different modules vary systematically in their period, this relation predicts an associated variation in the number of neurons.

Assume that an animal encodes position within a region of size R^2 that is common to all the modules, and that the probability of covering space is the same at all scales. As we showed above, the probability of gaps in coverage declines exponentially with the number of neurons, and the coefficient in the exponent depends on the ratio ℓ/λ between the grid field width and the period. It is established experimentally that this ratio is fixed among modules [53, 54]. Thus we can evaluate the predicted fraction of neurons in a given module, $N_i / \sum_i N_i$, where the denominator is a sum over modules, and N_i is obtained by inverting Eq. (4.8).

The results of this prediction and a comparison with the extant experimental data are shown in Fig. 4.7. The theoretical predictions are given for a variety of assumed ranges and coverage probabilities, with the grid periods and variabilities fixed from experimental data. Qualitatively, the theory predicts for any choice of parameters that the number of neurons should decline with the period of the module, as also suggested by the data.

The experiments of [54] measured responses from 4-5 modules in recordings spanning up to 50% of the dorsoventral extent of mEC, with a smallest grid period of about 40cm and a ratio of 1.42 between consecutive scales. This suggests that there should be about 10 modules in total in the rat grid system with a maximum period of about $10m$. We fit the theoretical predictions to the data of [54] and find that a range of a few tens of meters can indeed be covered with a high coverage probability. Within the range of parameters that allows this coverage in our model, we predict a decrease of about $50 - 70\%$ in the number of neurons between the first and tenth module (Fig. 4.7). Given the experimental uncertainties and possible biases in recording from harder-to-reach modules with larger periods, our fits to the existing data should be treated with caution. Nevertheless, our theory robustly states that the fraction of neurons should decline with the period of the grid module. Ongoing progress in making large-scale recordings from deeper regions of the brain will enable more stringent tests of our theory.

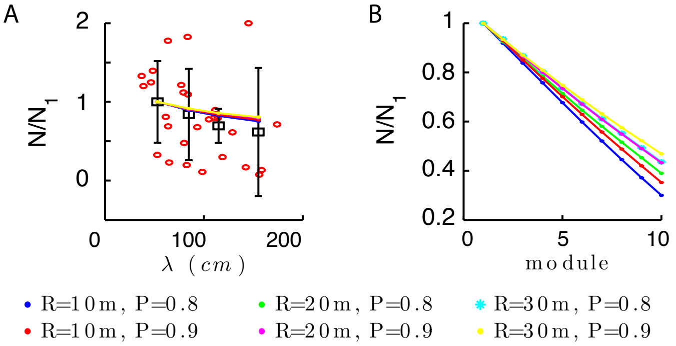

Figure 4.7: Fraction of neurons required for coverage decreases with the spatial period. (**A**) We used published data from 8 different rats and inferred the fraction of recorded neurons as a function of the spatial period (red circles represent the fraction of neurons in individual modules of individual animals) [54]. We divided the data according to the spatial period into four different modules using k–means clustering and obtain periods λ =53 cm, 85 cm, 115 cm, 155 cm. For each module we computed the associated fraction of neurons and plotted the mean and the standard deviation of the fractions of neurons in each module (black squares and lines). The theoretical prediction given by Eq. (4.8) depends on the choice of two unknown parameters, the radius of the environment (R) and the probability of covering P. We plotted the predictions for different combination of these values (colored lines.) Current data are compatible with different values of R and P. (**B**) We extrapolated the fraction of neurons over ten modules for different values of R, P. The theory predict a decrease of $50 - 70\%$ between the first and tenth module. Simulation parameters are $\lambda/\ell = 1.63$, $\sigma_\theta = 0.03$, $\sigma_\epsilon = 0$ and $\sigma_\lambda = 6$cm.

4.7 Discussion

A striking experimental observation about the grid system in the entorhinal cortex is that it is organized in discrete modules that share similar periods, orientations and ellipticities [54]. Given this modular structure, the geometric progression of grid periods can be shown to minimize the number of neurons required to provide a specified spatial resolution [56, 62]. However, why would a modular architecture be necessary in the first place? Here, we have shown that efficient coverage of space favors modularity.

We asked how variability in the periods, orientations and ellipticities within a module would affect the probability of holes in coverage. To carry out this analysis we were only interested in whether a neuron did or did not fire above the noise threshold at a given location – hence we treated the firing fields of grid cells as uniform within a bounded region. Of course, the actual firing rate of grid cells varies smoothly between the center and periphery of the firing field. So an alternative analysis could sum these firing profiles across the grid cell population to assess how variability in the periods, orientations and ellipticities affects the homogeneity of the population firing across space. As in our approach, the key variable would then be the correlation in the expected number of action potentials generated by the population at different sites, characterized by a correlation length as introduced above. Then in a similar manner, the probability of having any given degree of inhomogeneity would be a product over factors determined within each decorrelation volume. Thus, the analysis would be very similar to that reported here, and we would find again that coverage favors modularity.

We chose to analyze coverage because any grid coding scheme, e.g., [63, 64, 65, 62, 66, 56], will require neurons to be active at each point in space. Thus we view our approach as setting a minimal requirement for a functioning grid system for encoding location. Our model predicted that there would be fewer neurons in modules with larger periods and we compared our theory with the actual numbers of neurons recorded across modules. This comparison should be taken with caution because of potential biases in the recording methods, especially for deeper structures in the brains. Some additional evidence for a decrease of neurons with the period of modules stems from the relatively smaller size of the ventral entorhinal cortex (which is enriched in large periods) relative to the dorsal region. Indirect evidence also comes from the larger drifts seen in the activity of grid cells with larger periods [67] : attractor models indeed predict that networks with smaller numbers of neurons will drift more. However, because these lines of evidence are indirect, further data is needed. Comprehensive recordings from many grid modules are challenging because modules of a given period are not strictly localized anatomically, and because ventral regions are harder to record from. But such data will greatly illuminate models of the functional logic of the grid system, and will further test our quantitative predictions.

CHAPTER 5

Theory of feedback controlled brain stimulations for Parkinson's disease

5.1 Introduction

The basal ganglia circuit plays a central role in humans movements. In Parkinson's disease, the death of dopaminergic neurons in the substantia nigra causes movement disorders such as tremor, rigidity, slowness of movement, and postural instability [68, 69]. At the neural level, this degenerative process modifies the activity in the basal ganglia. In ill individuals, the neurons in the subthalamic nucleus show an oscillatory discharge pattern that is coherent at the frequency of the limb tremor [70]. Such activity is suppressed by treatment with the dopamine prodrug, levodopa, and by dopamine agonists [71]. The effect of treatment with these drugs is a reduction in the severity of the symptoms. These observations suggest that the anomalous discharge pattern is correlated to the motor disfunction.

Another strategy to reduce the symptoms associated with Parkinson's disease is deep brain stimulations on the basal ganglia [72, 73, 74]. In deep brain stimulation, electrodes implanted in the brain stimulate neurons in the subthalamic nucleus with electrical impulses at a constant frequency of about 100 Hz. Although the therapy has been shown to be effective in reducing the motor symptoms of the disease, it is far from optimal. In fact, the treatment delivers constant electrical stimulations independent of the state of the patient. Conversely, in brain disorders, and in particular in the case of Parkinson's disease, symptoms are highly variable, depending on factors such as cognitive and motor load and concurrent drug therapy [73]. A feedback control that modifies the stimulation parameters depending on the current state of the neural network would clearly be more appropriate and indeed solutions in this direction have been shown to be more efficient in alleviating parkinsonian motor symptoms than the standard deep brain stimulations [75, 76, 77] but, to the best of our knowledge, no general protocol has been found yet.

In this Chapter we derive a mathematical model that describes the dynamics of the subthalamic nucleus. We ascribe the onset of tremor–related activity in Parkinson's disease to a region of unstable activity in the phase diagram of the neural network. Based on this premise, we show that the main symptoms of the disease are reproduced as a consequence of the degradation of neural stimulation from the striatum and we propose a novel feedback based stimulation protocol to avoid the unstable region, and hence tremor. We also show that our procedure can be implemented with current technology and we finally test the efficiency of the protocol by numerical simulations of the dynamics in the basal ganglia.

5.2 Description of the model

Current evidence mentioned in the Introduction indicates that the death of the dopaminergic cells produces oscillatory neural activity in the basal ganglia and causes the tremor characteristic of Parkinson's disease. A priori, the complete circuit could be involved in the generation of the oscillations. However, experiments on *in vitro* cultures demonstrate that a suitable subcircuit shows spontaneous oscillatory activity analogous to that observed in the basal ganglia in patients affected by Parkinson's disease [78]. The subcircuit is formed by the external globus pallidus and the subthalamic nucleus together with external currents coming from the cortex and from the striatum. Motivated by this experimental observation, we will analyze here the dynamics of that subcircuit and show that its dynamics is indeed sufficient to explain the raise of the anomalous oscillation in the basal ganglia.

Our first goal is to give a microscopic description of the basal ganglia and to derive their effective dynamics. We consider a neural network with N neurons, $N_S = fN$ of which belong to the subthalamic nucleus and $N_G = (1-f)N$ to the external globus pallidus. To each neuron i we associate two continuous variables: the membrane potential $h_i(t)$ and the firing rate $F_i(t) \geq 0$, that are related by

$$F_i(t) = \phi_i(h_i(t)) \,, \tag{5.1}$$

with ϕ_i sigmoidal functions, e.g.

$$\phi_i(x) = \frac{\phi_i^\infty}{1+\exp\left[-g_i(x-h_i^*)\right]} \,. \tag{5.2}$$

The constants g_i measure the amplification of the neural response (g_S =0.3mV^{-1} [79], g_G =0.2mV^{-1} [80]), h_i^* is the activation potential (h_S^* =15 mV [79], h_G^* =10 mV [80]) and ϕ_i^∞ is the maximal firing rate (ϕ_S^∞ =0.5 kHz [81, 82], ϕ_G^∞ =0.1 kHz [80]).

The dynamics of the network is governed by the equation

$$\tau_i \dot{h}_i = -h_i + \sum_{k=1}^{N} R_{ik}\phi_i(h_k) + \eta_i + I_i \,, \tag{5.3}$$

where $\eta_i(t)$ are independent, Gaussian white noises $\langle \eta_i(t)\eta_j(t')\rangle = \Omega_i^2 \delta_{ij}\delta(t-t')$ and I_i are the external currents coming form the striatum (STR) and the cortex (CTX). The time constants τ_i are τ^S =6 ms [81, 82] and τ^G =14 ms [80], respectively. The matrix elements of the synaptic matrix R are Gaussian random variables. We suppose for simplicity the absence of self synapses, i.e. $R_{ii} = 0$. Note though that this biologically motivated assumption could be removed as it becomes irrelevant in the limit of a large number of neurons. The off-diagonal elements of the matrix R are

$$\langle R_{ij}\rangle = \mu_{ij} \,;\; \langle R_{ij}R_{ln}\rangle - \langle R_{ij}\rangle\langle R_{lk}\rangle = \delta_{il}\delta_{jk}\sigma_{ij}^2 \,. \tag{5.4}$$

The mean and the variance take four distinct values depending on the indices i and j belonging either to the subthalamic nucleus or to the external globus pallidus :

$$\begin{aligned}
\mu_{ij} &= m_{SS} \,, & \sigma_{ij} &= \sigma_{SS} \,, & i &= 1,\dots N_S \,,\; j = 1,\dots,N_S \,,\\
\mu_{ij} &= m_{SG} \,, & \sigma_{ij} &= \sigma_{SG} \,, & i &= 1,\dots N_S \,,\; j = 1,\dots,N_G \,,\\
\mu_{ij} &= m_{GS} \,, & \sigma_{ij} &= \sigma_{GS} \,, & i &= 1,\dots N_G \,,\; j = 1,\dots,N_S \,,\\
\mu_{ij} &= m_{GG} \,, & \sigma_{ij} &= \sigma_{GG} \,, & i &= 1,\dots N_G \,,\; j = 1,\dots,N_G .
\end{aligned} \tag{5.5}$$

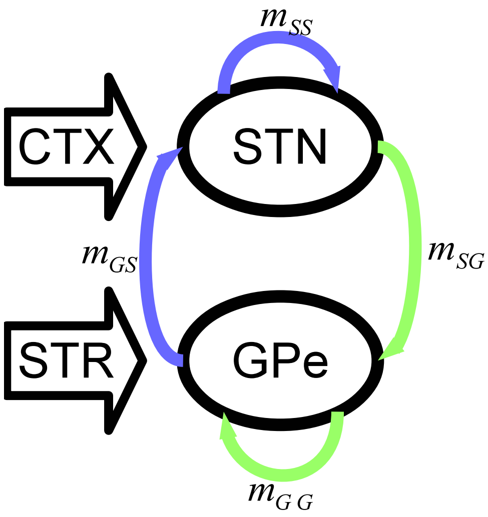

Figure 5.1: Loop within the basal ganglia formed by the subthalamic nucleus (STN) and the external globus pallidus (GPe) with external currents coming from striatum (STR) and cortex (CTX). Green arrows indicate excitatory connections whilst blue arrows denote inhibitory connections. The strength of the connections is controlled by the corresponding parameters m.

A scheme of the relation between these parameters and the neural network is shown in Fig. 5.1.

In the B.1, we show that in the large N limit, the single neuron membrane potential is given by

$$h_i(t) = \bar{h}_{S,G}(t) + \eta_i(t)\,, \tag{5.6}$$

where η_i is the white noise specified above and the mean nucleus membrane potential $\bar{h}_S$ or $\bar{h}_G$ appear in (5.6) depending on the value of the index i specifying the type of neuron. The mean nucleus membrane potentials obey the equations

$$\begin{aligned} \tau_S \dot{\bar{h}}_S + \bar{h}_S &= f m_{SS} \tilde{\phi}_S(\bar{h}_S) + (1-f) m_{SG}\, \tilde{\phi}_G(\bar{h}_G) + I_{CTX}\,, \\ \tau_G \dot{\bar{h}}_G + \bar{h}_G &= f m_{GS} \tilde{\phi}_S(\bar{h}_S) + (1-f) m_{GG}\, \tilde{\phi}_G(\bar{h}_G) + I_{STR}\,, \end{aligned} \tag{5.7}$$

with

$$\tilde{\phi}_{S,G}(x) = \frac{1}{\sqrt{\pi \Omega^2_{S,G}}} \int_{-\infty}^{+\infty} \mathrm{d}z\, \phi_{S,G}(z) \exp\left[-\frac{(z-x)^2}{\Omega^2_{S,G}}\right]\,. \tag{5.8}$$

In the next Section we discuss the dynamics of the system of equations (5.7) and relate it to the observations on the physiology of the basal ganglia in healthy and pathological conditions of Parkinson's disease.

We point out that the result of our microscopical derivation depends on the noise variance Ω. It is only in the limit of small noise, i.e. $\Omega_{S,G} \to 0$, that the mean field equations (5.7) reduce to the effective description previously used in the literature [83, 84, 85]. However, noise does affect the behaviour of the system as the signal to noise ratio measured in the subthalamic nucleus [70] is roughly $\simeq 8$. To reproduce this observation, noise must be included into the equations and we find that the appropriate value of the variance is: $g_S\Omega_S = 0.6$, where g_S is the gain factor defined in (5.2). As we discuss in detail in B.2, this relatively strong level of noise modifies the stability of the system and the network dynamics with respect to the noiseless case.

5.3 Results

5.3.1 Neural network phase diagram: healthy and pathological conditions

In this section we discuss the behaviour of the mean membrane potential given by equations (5.7).

For given values of the external currents $(I_{STR},\, I_{CTX})$, the system (5.7) has a set of equilibrium points: $\tau_S\dot{\bar{h}}_S = \tau_G\dot{\bar{h}}_G = 0$. The stability of each point is given by the corresponding eigenvalue of the Jacobian matrix. Eigenvalues with a negative real part correspond to stable equilibrium points while a positive real part leads to local instability. As showed in [83] the system has either a finite number of stable equilibrium points, corresponding to equilibrium solutions $\left(\bar{h}_G,\, \bar{h}_S\right)$ constant in time (Fig. 5.2), or one unstable equilibrium point. In the latter case, due to the confining properties of equations (5.7), the Poincaré-Bendixson theorem [86] states that a limit cycle and an oscillatory solution (Fig. 5.2) will arise.

An example of the stability of the system as a function of the external currents is shown in the phase diagram of Fig. 5.3. The phase space features two distinct regions: with stable fixed points and with unstable fixed points where limit cycles arise. The position and the size of these regions depends both on the parameters of the network $m_{SS},\, m_{GS},\, m_{SG},\, m_{GG}$ (for an extensive discussion of this point see [83]) and on the noise variance Ω (see B.2).

The basal ganglia activity in patients affected by Parkinson's disease resembles the behaviour found in the unstable region. Indeed, an oscillatory activity is then superimposed (see equation (5.6)) to the single neuron membrane potential. Therefore, we shall posit that the non-pathological dynamics corresponds to external currents driving the system within the stable region. Furthermore, we assume that the death of dopaminergic neurons in the substantia nigra modifies the fluctuations of the external currents in such a way that the dynamics enters the unstable region. We identify this situation as the pathological Parkinson condition. This is analogous to what was proposed in [83] for the case without any noise. An example of transition from healthy to pathological condition is given in Fig. 5.4.

We remark that the network behaviour in the healthy and the pathological condition described here should be understood as background in the dynamics of the brain. The background is accompanied by the local activity induced by time variation of the external currents. It is therefore intuitive that a constant background corresponds to the healthy status and a variable background is harmful to the network functions controlled by the total (background+local) activity.

The scenario above provides an intuition as to the goal of an external feedback stimulation: keep the region of activity of the network (driven by external currents) away from the unstable region of the system. In the next Section we use this principle to design a feedback control system that modifies the position and the size of the unstable region in the phase diagram to avoid anomalous oscillations in the network.

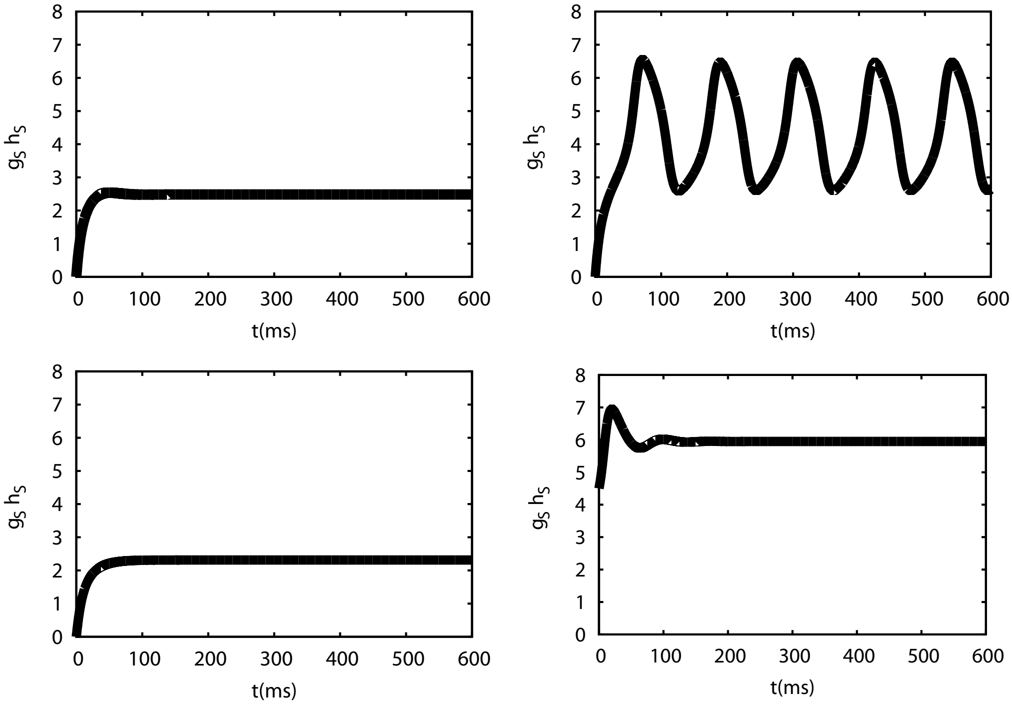

Figure 5.2: Dynamics of the mean subthalamic nucleus membrane potential given by equations (5.7) for different values of the external currents. For external currents $g_S I_{CTX} = 2$ from the cortex and $g_G I_{STR} = -0.5$ from the striatum, the system has one stable equilibrium point that corresponds to constant membrane potential (top left). For $g_S I_{CTX} = 2$ and $g_G I_{STR} = -1.5$ there is one unstable equilibrium point that leads to oscillatory behaviour (top right). In the case $g_S I_{CTX} = 2$ and $g_G I_{STR} = 0.5$ there are two stable equilibrium points (bottom left and right). In solving numerically equations (5.7) we used mean synaptic efficacy $f m_{SS} = 54 mV/kHz$, $(1-f) m_{SG} = 120 mV/kHz$, $f m_{GS} = 80 mV/kHz$ and $(1-f) m_{GG} = 100 mV/kHz$. The noise variance is $g_S \Omega_S = 0.6$, $\Omega_S = \Omega_G$. Initial condition are $\bar{h}_S = \bar{h}_G = 0$ for figures at the top and bottom left while $g_S \bar{h}_S = 5$, $\bar{h}_G = 0$ for the figure at the bottom right.

5.3.2 A feedback system avoids anomalous oscillations

Current technology allows to stimulate and measure simultaneously the activity of a whole group of neurons [76]. Here, based on this possibility, we discuss a feedback stimulation protocol to modify the neural network phase diagram and to avoid the pathological condition identified in the previous paragraph.

The dynamics of the neurons in the network with a feedback system is given by

$$\tau_i \dot{h}_i = -h_i + \sum_{k=1}^{N} R_{ik} \phi_i(h_k) + \eta_i + I_i + H_i \,, \tag{5.9}$$

where H_i represents the external stimulation on neuron i of the circuit due to the feedback control. In standard deep brain stimulations H_i is a sinusoidal function with a frequency that is fixed, independent of the network activity and applied only on neurons of the subthalamic nucleus. In our case we also suppose a uniform external stimulation

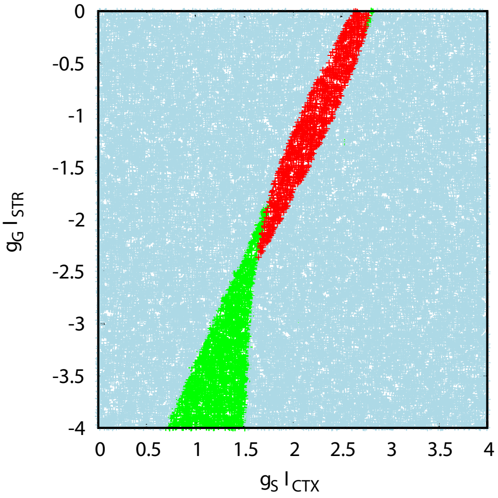

Figure 5.3: Stability of the equilibrium points as a function of the external currents. For every value of $(I_{STR},\ I_{CTX})$, using equations (5.7), we computed the equilibrium points and their stability. As explained in the main text, there are three possible behaviors. Red points correspond to unstable equilibrium that leads to oscillatory field potential for the neurons in the network. The other points are associate to stable (light blue) and bistable (green) equilibrium solutions. Simulation parameters are as in Fig. 5.2.

of the network, *i.e.* $H_i(t) = H(t)$, yet the stimulation will actively depend on the state of the network itself.

Let us discuss a possible implementation of an active feedback stimulation acting only on the subthalamic nucleus. We choose this target because current technology of stimulation and measurements have mostly been developed for that area and the implementation of our results requires just a software update. The uniform feedback $H_i(t) = H(t)$ on the group of neurons will depend only on global observables, e.g. the mean activity or the standard deviation. We can then perform a calculation similar to that outlined above and discussed in detail in the Appendix. The result is the pair of mean field equations

$$\begin{aligned} \tau_S \dot{\bar{h}}_S + \bar{h}_S &= f m_{SS} \tilde{\phi}_S(\bar{h}_S) + (1-f) m_{SG} \tilde{\phi}_G(\bar{h}_G) + I_S + H\,, \\ \tau_S \dot{\bar{h}}_G + \bar{h}_G &= f m_{GS} \tilde{\phi}_S(\bar{h}_S) + (1-f) m_{GG} \tilde{\phi}_G(\bar{h}_G) + I_G\,. \end{aligned} \tag{5.10}$$

The structure of equation (5.10) suggests a control term of the form

$$H = -\alpha \tilde{\phi}_S(\bar{h}_S)\,, \tag{5.11}$$

which gives for the network dynamics

$$\begin{aligned} \tau_S \dot{\bar{h}}_S + \bar{h}_S &= (f m_{SS} - \alpha) \tilde{\phi}_S(\bar{h}_S) + (1-f) m_{SG} \tilde{\phi}_G(\bar{h}_G) + I_S\,, \\ \tau_S \dot{\bar{h}}_G + \bar{h}_G &= f m_{GS} \tilde{\phi}_S(\bar{h}_S) + (1-f) m_{GG} \tilde{\phi}_G(\bar{h}_G) + I_G\,. \end{aligned} \tag{5.12}$$

The rationale for (5.11) is that (5.10) is thus reduced to (5.12), which has the same structure as the mean field equations (5.7). The phase diagram of the system is therefore

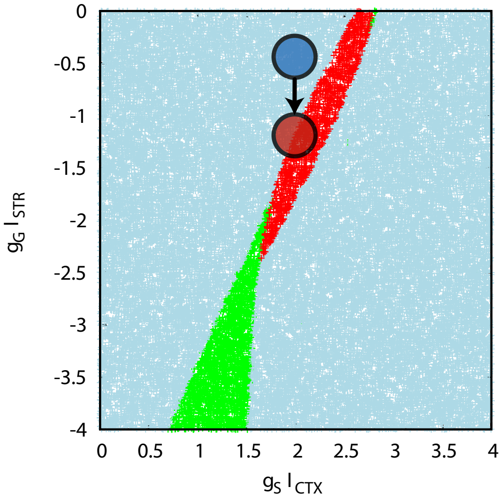

Figure 5.4: Example of transition from healthy to pathological condition represented on the phase diagram of Fig. 5.3. In the healthy state (blue circle) the external currents from the cortex and the striatum fluctuate in a region with stable equilibrium points. A pathological decrease in the current from the striatum, that in Parkinson's disease could be generated by the death of dopaminergic neurons in the substantia nigra, drive the system into an unstable region (red circle) in which spontaneous oscillation in the neural activity arises.

preserved by the control, yet we can modify the connection parameters m by varying α. Tuning the parameter α allows then to keep the physiological region of activity of the external currents away from the unstable region and hence avoid anomalous oscillations in the system. In Fig. 5.5 we show explicitly the effect on the phase diagram that is achieved by modifying α. The correct behaviour of our feedback system can be seen also in the neurons dynamics, as showed in Fig. 5.6.

A possible concern is that in real applications, the region in the subthalamic nucleus that can be stimulated is just a fraction of the network. It is then important to verify that partial stimulation produces a result similar to that found in the effective model. We verified that that is indeed the case by simulating the complete dynamics of a neural network described by equation (5.9) assuming that the feedback term H_i measures and stimulates only a fraction k of neurons in the subthalamic nucleus. Fig. 5.7 confirms that the control system is effective also with the stimulation operating on a limited fraction of neurons.

5.4 Discussion

We have described a simple model that suggests a new protocol for therapeutic deep brain stimulation of the basal ganglia. The main difference with respect to previous work is twofold. First, our systematic formalism allows us to naturally include the effect of noise, which results to affect the dynamics of the system and its stability properties, as seen from the phase diagram in Fig. B.1. Second, our protocol of stimulation is active, meaning that it depends on the state of the network itself. Our stimulation paradigm follows naturally from the model of the neural network that we derived, so it

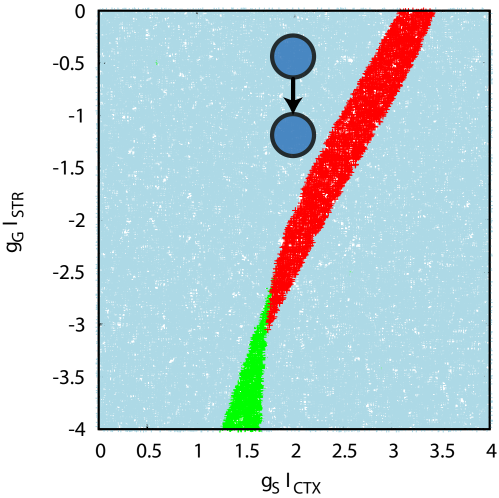

Figure 5.5: Phase diagram of the network with control term $\alpha = 6mV/kHz$. Because of the feedback system the structure is different from that of Fig. 5.4. We point out that the pathological decrease in the current from the striatum does not produce anomalous oscillations. Indeed the external currents continue to fluctuate into a stable region, as showed by the blue circle at the bottom. Simulation parameters are as in Fig. 5.2.

does not need to be determined empirically as in other works [75, 76]. The application that we presented to the stimulation of the subthalamic nucleus gives promising results that would deserve to be tested experimentally. The protocol is based only on the measurement and the stimulation of neural activity in the subthalamic nucleus and therefore fully compatible with existing technology [76].

Furthermore, the performance of the method favorably compares with the standard deep brain stimulations. Indeed, as discussed in [85], the effect of standard deep brain stimulations is to reduce the amplitude of the anomalous oscillations in the unstable region. Conversely, we showed that in our protocol the oscillations vanish completely because the active feedback that we designed allows the network to systematically work in the stable region. Hence, we expect that our protocol should constitute an improvement of standard treatments in controlling Parkinson's related limb tremor, as confirmed already by simulations.

An interesting direction for further improvement of our protocol relates to the parameter α controlling the active feedback (see Eq. (5.11)). Its value depends on the value of the unknown connection parameters and thus in our simulations it was fixed empirically. Moreover, the stable state that is driven by the feedback has in general a different firing field with respect to the healthy conditions. New experiments providing quantitative information on the strength and the variability of the connection parameters and on the firing field in the post-stimulation stable state should permit to better tune the control and further improve the active protocol presented here.

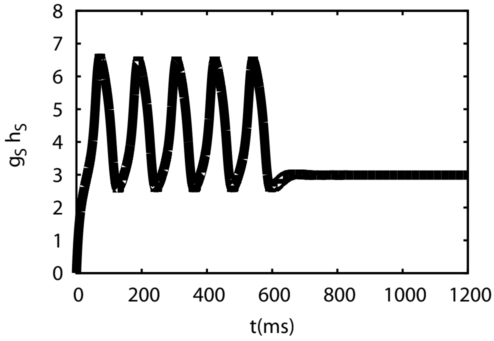

Figure 5.6: The feedback control stops anomalous oscillation in the mean subthalamic nucleus membrane potential. From 0 to $600ms$ there is no feedback system ($\alpha = 0$) and the membrane potential oscillates in time. At 600ms the control is switched on ($\alpha = 6mV/kHz$) and maintained until the end of the simulation at 1200ms, manifestly suppressing oscillations. Parameters in the simulation are as in Fig. 5.2 with $g_S I_{CTX} = 2$, $g_G I_{STR} = -1.5$.

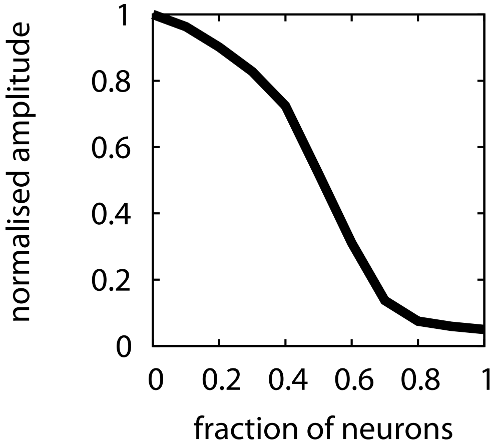

Figure 5.7: Amplitude of anomalous oscillations as a function of the fraction k of neurons in the subthalamic nucleus involved in the measurement and stimulations. The amplitude of the oscillations decreases with k. Simulation parameters are as follows: $g_S \Omega_S = 0.6$, $\Omega_S = \Omega_G$; $g_S I_i = 2$, $g_G I_i = -1.5$; we used 500 neurons both for subthalamic nucleus and the globus pallidus. The connection parameters are $m_{SS} = 0.108mV/kHz$, $m_{SG} = -0.24mV/kHz$, $m_{SS} = 0.16mV/kHz$ and $m_{GG} = -0.2mV/kHz$. Connections are Gaussian distributed around these mean values with variance $\sigma = 0.002mV/kHz$. Because of the scaling (B.9), the resulting mean field parameters are those used in Fig. 5.2. We introduced the control system on a fraction k of neurons in the subthalamic nucleus, which modifies the connection parameters of a value $\alpha = 0.006mV$. The network dynamics was simulated for $25s$. For each k the network shows the same oscillatory activity observed in the mean field system. In the figure we reported the amplitude (defined as the difference between the maximum and the minimum value) of mean neural field potential in the subthalamic nucleus population normalized to its maximum value ($k = 0$).

APPENDIX A

Complete coverage of space favors modularity of the grid system

A.1 Covering probability of non-isosceles grids

In the main text we analyzed the covering probability of the grid system assuming isosceles grids, in this Section we show that our results hold also in the case of general grids.

The triangular lattice defining the spatial activity of a grid cell is determined by linear combinations of two elementary vectors $\mathbf{v}$ and $\mathbf{u}$. The reference frame can be chosen to have the vector $\mathbf{u}$ coinciding with the x-axis, i.e. $\mathbf{u} = \lambda_2(1,0)$ and the vector $\mathbf{v} = \lambda_1(\cos(\beta), \sin(\beta))$, where β is the angle formed by the two elementary vectors (which can be restricted to the first quadrant). The two positive numbers λ_2 and λ_1 are the moduli of the two elementary vectors. The set of the six vertices defined by the triplet $\mathbf{u}$, $\mathbf{v}$, $\mathbf{u} - \mathbf{v}$ and their opposite vectors, forms an hexagon that can be inscribed into an ellipse centered at the origin, whose general equation is $Ax^2 + 2Bxy + Cy^2 = 1$ (see Fig. A.1A). The (inverse squared) length of the two axes of the ellipse is determined by the eigenvalues of the quadratic form and their orthogonal directions are determined by the corresponding eigenvectors.

An alternative parametrization of the ellipse is given by : 1) the direction δ of the axes of the ellipse with respect to the axes of the reference frame ; 2) the ratio ϵ between the length of the two axes (i.e. the ellipticity of the grid as defined in [54]) ; 3) the length $\lambda/\sqrt{\epsilon}$ of the axis parallel to the x-axis when $\delta = 0$ (the other axis has length $\sqrt{\epsilon}\,\lambda$). By requiring that the ellipse pass through the three independent vertices $\mathbf{u}$, $\mathbf{v}$, $\mathbf{u} - \mathbf{v}$, we obtain the relations

$$\lambda_2 = \frac{\lambda}{\sqrt{F_1}}\,; \quad \lambda_1 \sin\beta = \frac{\sqrt{3}}{2}\lambda_2 F_1\,; \quad \lambda_1 \cos\beta = \frac{\lambda_2 F_2}{2}$$
$$F_1 \equiv \epsilon\cos^2\delta + \frac{1}{\epsilon}\sin^2\delta\,; \quad F_2 \equiv 1 - \sqrt{3}\left(\epsilon - \frac{1}{\epsilon}\right)\sin\delta\,\cos\delta\,, \tag{A.1}$$

which provide a general mapping between the free parameters λ, ϵ, δ of the ellipse and the free parameters λ_1, λ_2, β of the vectors $\mathbf{u}$ and $\mathbf{v}$. Ellipses with $\delta = 0$ have axes aligned with the coordinate system. Elementary algebra shows that this condition corresponds to isosceles triangles with $|\mathbf{v}| = |\mathbf{u} - \mathbf{v}|$, i.e. $2\lambda_1\cos\beta = \lambda_2$ or $\cos\beta = 1/\sqrt{1 + 3\epsilon^2}$. The special case of $\epsilon = 1$ fixes $\lambda_1 = \lambda_2 = \lambda$ and $\cos\beta = 1/2$, i.e. corresponds to equilateral triangles. We stress that the direction δ is related only to the deformation of the hexagon defined by the elementary vectors and its variations do no affect the orientation θ of the grid.

We generalize the analysis of the main text to cases where the axes of the ellipse are not aligned with the coordinate system ($\delta \neq 0$), which generally corresponds to scalene triangles. We choose a parametrization where ϵ, δ and λ vary independently. The upshot is that the results presented in the main text still hold. Specifically, for fixed σ_λ/λ and σ_θ we compute the correlation coefficient between the number of neurons that are active at the center of two unit cells, as described in the main text. Fig. A.1B, C illustrates the results of the simulations for different values of σ_ϵ and σ_δ using general grids. As for the other sources of variability, the correlation decreases rapidly with the separation between the two centers and the correlation length decreases as σ_ϵ and σ_δ increase. Finally, Fig. A.1D also shows that the covering probability conforms to the relation (4.2) presented in the main text.

A.2 Fit of variability in the grid parameters

In order to measure variability in grid parameters, we analyzed data from Stensola et al. [54]. For each animal where the distribution of grid parameters is available, we fit the data with a sum of Gaussians. For each module, we used one Gaussian for the period (mean λ, standard deviation σ_λ) and one for the orientation (mean θ, standard deviation σ_θ.) The two standard deviations are roughly constant in the various modules. Indeed, the Pearson correlation coefficient is 0.21 between σ_λ and λ and 0.28 between σ_θ and λ. The standard deviation of the grid period is about 6 cm. Assuming 10 modules and that the smallest is about 40cm, the ratio σ_λ/λ goes from 0.01 to 0.15. The standard deviation of the orientation in a module is about 0.03 rad. In the literature we were not able to find the distribution of ellipticity in the population within a single module. We know that ellipticity also has a modular structure and that across a population (all modules) the mean ellipticity is around 1.16 ± 0.003 [54]. In the analysis we assume a standard deviation in ellipticity in the range 0.01-0.15, i.e. similar to the grid spacing.

A.3 Analysis of the correlation function

In this section we discuss the asymptotic behavior of the Pearson correlation function of the number of neurons active at two spatial points (i.e., the correlation function normalized to 1 for coincident points) at large separations. We show that, as long as there is some variability in the orientation, the correlation function tends to zero; the special case of zero variability in orientation is not relevant to the analysis of the covering probability in the actual grid system.

The number of neurons active at a spatial point $\mathbf{x}$ is given by $n(\mathbf{x}) = \sum_{i=1}^{N} a_i(\mathbf{x})$, where a_i is the spatial activity of the $i-$th neuron given by Eq. (4.1) and N is the number of neurons in the system. We are assuming that grid cells in a module fire independently. Therefore, the correlation function of the number of neurons active at $\mathbf{x}$ and $\mathbf{y}$, $\rho(n(\mathbf{x}), n(\mathbf{y}))$, is equal to the correlation function of the activity of a single generic neuron $a(\mathbf{x})$, averaged over the distribution of grid parameters, $\rho(a(\mathbf{x}), a(\mathbf{y}))$. In what follows we compute the asymptotic value of this correlation function for $|\mathbf{y} - \mathbf{x}|/\lambda \gg 1$.

The mean activity of a single neuron is obtained from Eq. (4.1) by averaging over the

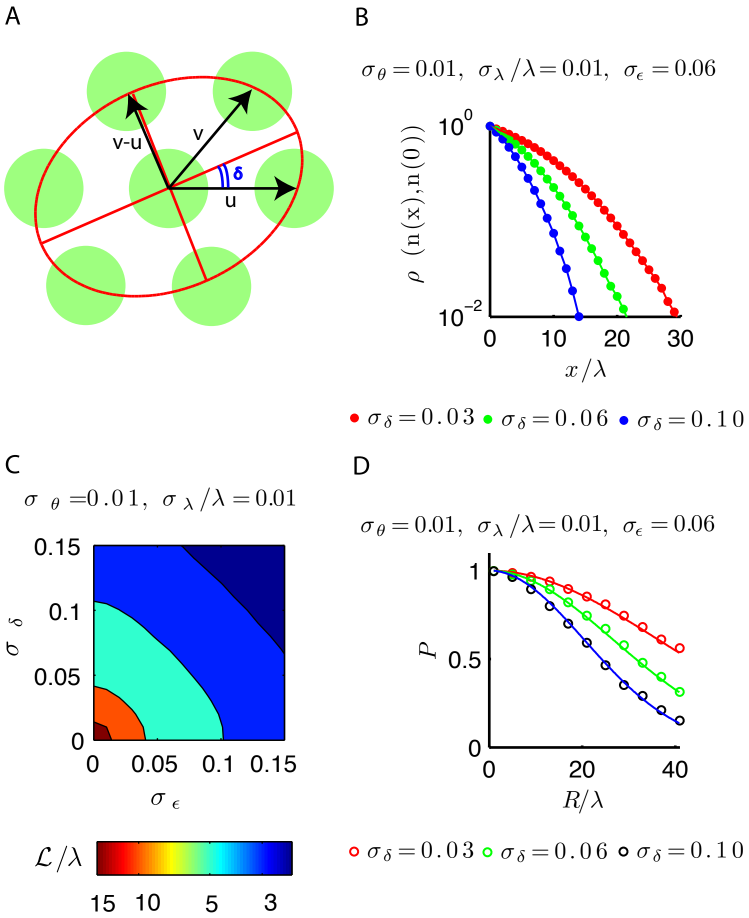

Figure A.1: Variability in ellipticity ϵ and direction δ induces decorrelation and decreases the covering probability. We perform the same analysis as in the main text for the more general case $\delta \neq 0$. (**A**) Representation of the grid activity with $\delta \neq 0$. The six firing fields defined by the triplet **u**, **v**, $\mathbf{u} - \mathbf{v}$ and their opposite vectors (green circles) have centers belonging to an ellipses (curved red line), the ellipse axes (straight red lines) are rotated rotated by an angle δ respect to the vector **u** aligned with the x-axis. (**B**) The Pearson correlation coefficient is computed as in Fig. 4.4. (**C**) Correlation length for different values of σ_ϵ and σ_δ computed as in Fig. 4.4. (**D**) Covering probability computed as in Fig. 4.5. We find that increasing variability reduces the correlation length and decreases the covering probability. Eq. (4.4) correctly describes the covering probability as a function of variance and environment size.

grid parameters. This quantity can be written as

$$\langle a(\mathbf{x})\rangle = \int a(\mathbf{x})\, dP_\theta dP_\lambda dP_\epsilon dP_{\boldsymbol{\phi}} \tag{A.1}$$

$$= \sum_{n,m\in\mathbb{Z}} \int \chi\left(\frac{|\boldsymbol{\phi} + R(\theta)\,[n\mathbf{v} + m\mathbf{u})] - \mathbf{x}|}{\ell/2}\right) dP_\theta dP_\lambda dP_\epsilon dP_{\boldsymbol{\phi}}\,, \tag{A.2}$$

where $dP_{(*)}$ represents the measure related to the grid parameter $(*)$. As discussed in the main text, orientation, period and ellipticity of the grids follow a gaussian distribution whilst the spatial phase is uniformly distribute in a unit cell. To compute the integral, we divide the space into unit cells and consider the center of the cell containing $\mathbf{x}$ as a reference point respect to which we express the phase of the grid $\boldsymbol{\phi}$. Because $\boldsymbol{\phi}$ is uniformly distributed in the unit cell and χ is 1 within the firing field and 0 outside, the integral over $\boldsymbol{\phi}$ is a constant equal to the ratio between the area of a firing field and that of a unit cell, i.e. $\pi/2\sqrt{3}\ (\ell/\lambda)^2$. The remaining integrals are equal to one and we obtain $\langle a(\mathbf{x})\rangle = \pi/2\sqrt{3}\ (\ell/\lambda)^2$.

In order to compute the correlation function we need to determine the quantity

$$\langle a(\mathbf{y})a(\mathbf{x})\rangle = \int a(\mathbf{y})a(\mathbf{x})dP_\theta dP_\lambda dP_\epsilon dP_{\boldsymbol{\phi}}\,, \tag{A.3}$$

that can also be written as

$$\langle a(\mathbf{y})a(\mathbf{x})\rangle = \int P_{\boldsymbol{\phi}}(\mathbf{y},\mathbf{x})dP_{\boldsymbol{\phi}}\,, \quad P_{\boldsymbol{\phi}}(\mathbf{y},\mathbf{x}) = \int a(\mathbf{y})a(\mathbf{x})\, dP_\theta dP_\lambda dP_\epsilon\,, \tag{A.4}$$

where $P_{\boldsymbol{\phi}}(\mathbf{y},\mathbf{x})$ is the joint probability distribution that depends parametrically on $\boldsymbol{\phi}$. The joint probability can be computed as

$$P_{\boldsymbol{\phi}}(\mathbf{y},\mathbf{x}) = P_{\boldsymbol{\phi}}(\mathbf{y}|\mathbf{x})P_{\boldsymbol{\phi}}(\mathbf{x}) \tag{A.5}$$

where $P_{\boldsymbol{\phi}}(\mathbf{y}|\mathbf{x})$ is the conditional probability that a neuron is active at $\mathbf{y}$ if it is active at $\mathbf{x}$ and $P_{\boldsymbol{\phi}}(\mathbf{x})$ is the probability that a neuron is active at $\mathbf{x}$. In order to evaluate the conditional probability we divide space into unit cells using the mean grid parameters. We consider a neuron with $\boldsymbol{\phi} = (0,0)$, i.e. with a firing field centered at the origin, and analyze the evolution of its phase $\boldsymbol{\phi}_n$ in the unit cells centered at $\mathbf{y} = (n\lambda, 0)$, $n = 0,\ 1,\ \ldots$. If the grid cell has the same grid properties of the average grid, its phase will be invariant, i.e. $\boldsymbol{\phi}_n = \boldsymbol{\phi}$. If the grid has the same orientation of the mean grid but different period ($\lambda' \neq \lambda$), the phase will gradually shift along the $x-$axis as n increases but it will always belong to a one dimensional surface with fixed y component equal to ϕ_y. When n increases the phase becomes randomly distributed along the segment $[(n-1/2)\lambda, (n+1/2)\lambda]$ and the probability that the point $\mathbf{y} = (n\lambda, 0)$ is covered given that $\mathbf{x} = (0,0)$ is covered depends on ϕ_y. In particular, a grid that covers the point $\mathbf{x}$ will have an intersection of length $2\sqrt{\ell^2/4 - \phi_y^2}$ between its firing field and the segment $[-1/2\lambda, +1/2\lambda]$. Because of the previous argument, for large n this interval will be uniformly distributed along the segment $[(n-1/2)\lambda, (n+1/2)\lambda]$ so it will cover the point $\mathbf{y}$ with probability

$$P_{\boldsymbol{\phi}}(\mathbf{y}|\mathbf{x}) = \frac{2\sqrt{\ell^2/4 - \phi_y^2}}{\lambda}\,. \tag{A.6}$$

On the other hand, the probability of having a neuron active at $\mathbf{x}$ is

$$P_{\boldsymbol{\phi}}(\mathbf{x}) = \begin{cases} 0 & \text{if } \phi_x^2 + \phi_y^2 > (\ell/2)^2 \\ 1 & \phi_x^2 + \phi_y^2 \leq (\ell/2)^2 \end{cases} \tag{A.7}$$

Combining the previous results we obtain $\langle a(\mathbf{y})a(\mathbf{x})\rangle \to \frac{4\sqrt{3}\ell^3}{9\lambda^3}$. Hence, if the orientation variance is zero the correlation coefficient between two distant points reaches the asymptotic value

$$\rho(a(\infty), a(\mathbf{0})) = \frac{\frac{8\ell}{3\pi\lambda} - \frac{\pi\ell^2}{2\sqrt{3}\lambda^2}}{1 - \frac{\pi\ell^2}{2\sqrt{3}\lambda^2}}\,. \tag{A.8}$$

This has been confirmed numerically in Fig. A.2. The same argument holds if ellipticity variance is present.

On the other hand, if there is variance in the orientation, as n increases the phase of the grid will be randomly distributed in the two-dimensional area of the unit cell centered at $(n\lambda, 0)$. It follows that $\langle a(\mathbf{y})a(\mathbf{x})\rangle \to \langle a(\mathbf{x})\rangle$ and the correlation asymptotically goes to zero as shown in Fig. 4.4.

In the main text we assessed the correlation length of a grid system as the distance at which the correlation in the number of active cells falls below a fixed threshold. The results of the present Section fix a specific range in which this threshold should be chosen. Indeed, for a given ℓ/λ, Eq. (A.8) gives the asymptotic value of the correlation function when no variance in the orientation is present, e.g. in the biological system $\ell/\lambda \approx 1/1.63$ and the asymptotic value of the correlation is about 0.28 (see Fig. A.2B). Because of the effect described above, if the threshold used to define the correlation length is chosen below this value, the correlation length will depend only on the orientation variance. Hence, in order to assess the length scale of correlation that is affected by the variance in all the grid parameters, a threshold slightly above the asymptotic value should be chosen (in the main text we used $1/e$.) This choice is relevant because it captures the dependence of the covering probability on the variance in the grid parameters. In fact, if our definition of the correlation length is used to analyze the covering of a system, the analytical results obtained from our approach are in agreement with direct numerical analysis performed with (see Fig. 4.5) and without (see Fig. A.2D) orientation variance.

A.4 Covering probability of a decorrelation volume

In the main text we showed that within a single volume of side $\mathcal{L}$, the correlation between the number of active neurons $n(\mathbf{x})$ and $n(\mathbf{y})$ approaches one if $|\mathbf{x}-\mathbf{y}|/\mathcal{L} \ll 1$ and decreases continuously as the distance increases. In this Section we derive the functional dependence of p, the probability of covering a decorrelation volume, on its linear size $\mathcal{L}$ and on the probability of covering a unit cell p_{uc}.

We computed numerically the covering probability of a circolar environment of radius R using sets of grid cells characterized by different p_{uc}, results of the simulations are shown in Fig. A.3. For every value of the radius R the logarithm of the covering probability rescaled over $\log(p_{uc})$ does not depend on p_{uc} (Fig. A.3B). It follows that the probability p of covering a decorrelation volume of linear size $\mathcal{L}$ can be expressed as

$$\log(p) = \mathcal{K}\,\log(p_{uc})\,, \tag{A.1}$$

where $\mathcal{K}$ is a function that depends only on $\mathcal{L}/\lambda$ for dimensional reasons.

Over a range of grid variances that includes the experimentally measured values, we found that $\mathcal{L}/\lambda \lesssim 20$ (Fig. 2 of the main text). In this range, we found numerically that $\mathcal{K}(x) = c_1 + c_2\log(x)$ ($c_1 = 0.73$, $c_2 = 13$) gives a good description of the data (see Fig. A.3C) .

A.5 Covering probability of a unit cell

We discuss the covering probability of a unit cell in one dimension. We take each grid cell to be active in intervals of length ℓ, regularly spaced with centers at distance λ apart. A unit cell is given by an interval of length λ. The covering probability of a unit cell by N grid cells is analogous of that of covering a region of length λ by N intervals of length ℓ

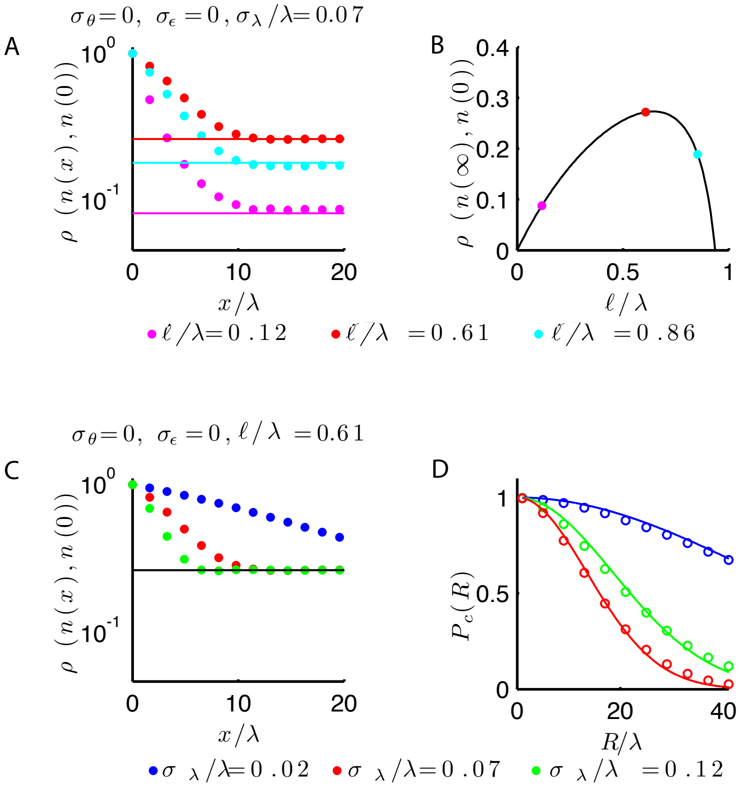

Figure A.2: The correlation length depends on the behavior above the asymptotic value of the correlation. (**A**) When there is no variance in grid orientations, the correlation function between the number of active cells at two locations, $\rho(n(x), n(0))$, approaches a nonzero asymptotic value that depends on ℓ/λ. The solid lines indicate the theoretical prediction of the asymptotic values from Eq. (A.8). (**B**) The asymptotic value of the correlation in the absence of orientation variance is predicted by Eq. (A.8) (black line). Representative values corresponding to the three curves in panel **A** are marked by the colored dots. Note that there is a maximum value in the asymptotic correlation as a function of l/λ. (**C**) The correlation decreases faster when the variance in the period increases. (**D**) Numerical simulations (colored dots) determine the covering probability of the environment for the different variances in the grid parameters and environment sizes. The numerics are accurately predicted by Eq. (4.8) of the main text (solid lines) in which the correlation length for a grid system was assessed as the distance at which ρ in panel **C** decreased to $1/e$. This threshold is always larger than the asymptotic value of the correlation (see main text).

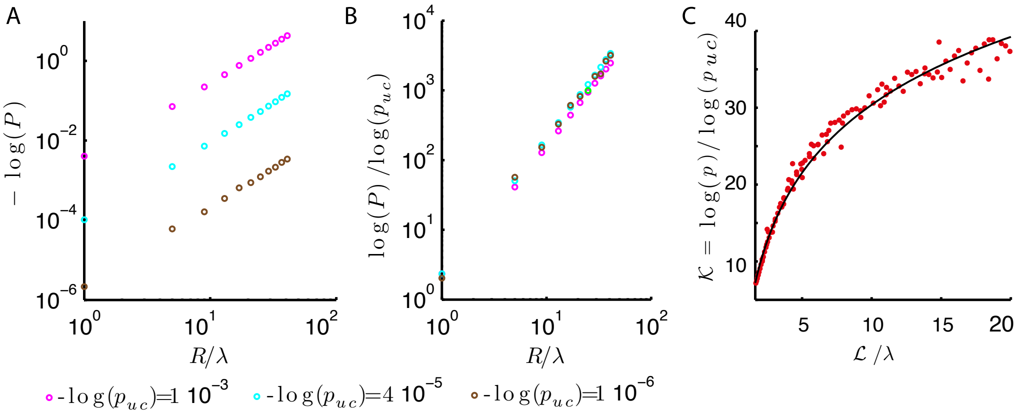

Figure A.3: Covering probability of a decorrelation volume of linear size $\mathcal{L}$. (**A**) Covering probability P of a circular environment of linear size R computed numerically for different environment size and covering probability of the unit cell p_{uc}. The different values of p_{uc} have been obtained using sets of grid cells made of a different number of neurons, as discussed in the main text. (**B**) Results of panel (**A**) collapse on a common curve when their logarithm is rescaled over $\log(p_{uc})$, justifying the functional form introduced in Eq. A.1. (**C**) Numerical covering probability p of a decorrelation volume of linear size $\mathcal{L}$ have been used to obtain an empirical description of the function $\mathcal{K}(\mathcal{L}/\lambda)$ described in Eq. A.1 (red dots). The best fit (black line) is given by the function $\mathcal{K}(x) = 0.73 + 13\log(x)$. Simulations parameters are λ/ℓ =1.63, $\sigma_\theta = 0.04$, $\sigma_\epsilon = 0$. In panels (**A**-**B**) we fixed $\sigma_\lambda/\lambda = 0.08$ whilst the number of neurons N is 30 (magenta), 40 (light blue), 50 (brown). In panel (**C**) we fixed $N = 30$ and σ_λ/λ has been varied to span the different values of $\mathcal{L}$ observed in the biological system as described in Fig 4.4E of the main text.

with periodic boundary conditions on the region. This probability distribution has been computed analytically in [61] and is

$$P\left(N, \frac{\ell}{\lambda}\right) = \sum_{k=0}^{N} (-1)^k \binom{N}{k} f(k)\,, \tag{A.1}$$

where $f(k) = (1 - k\ell/\lambda)^{N-1}$ if $k\ell < \lambda$ and $f(k) = 0$ otherwise. For large N this relation reduces to the result used in the main text $P = 1 - N\,(1 - \ell/\lambda)^{N-1}$.

The proof of (A.1) is presented below for the sake of completeness. Because we have periodic boundary conditions on the region to be covered, we can regard it as a circle of unit length and we can take the intervals of length $\zeta = \ell/\lambda$ to be arcs on this circle. The arcs are labelled by their order of occurrence in the anti-clockwise direction around the circle, starting by convention from the north pole. The arcs are identified by their initial position ; there is a gap after the r-th arc if the distance between the initial positions of the r-th and the $r+1$-th arcs is larger than the size of the arcs. For convenience, we rigidly translate all the arcs so that the first one is positioned at the north pole – this convention does not affect the probability of coverage.

Consider N random arcs of length ζ on the circle. Draw k arbitrary arcs from this set (say $(r_1, r_2, \ldots r_k)$, with $k \leq N$). Let $f(k)$ be the probability that each arc in this randomly selected subset is followed by a gap, irrespective of the state (followed by a gap or not) of all the other arcs. From the $f(k)$'s, the probability (A.1) of leaving *no* gaps is computed as follows. First, let $Q(n_g, n_u)$ be the probability that n_g prescribed arcs are each followed by a gap and n_u prescribed arcs are each not followed by a gap, with the rest of the N arcs in unspecified states. Then, $Q(n_g, 1) = f(n_g) - f(n_g + 1)$ because $f(n_g)$ includes the probability that the extra arc might be gapped or ungapped, while $f(n_g + 1)$ subtracts the probability that the extra arc is in fact gapped. By a similar reasoning we obtain $Q(n_g, 2) = Q(n_g, 1) - Q(n_g + 1, 1)$ and so on recursively up to $n_g + n_u = N$. Simple algebra shows then that the probability of leaving no gaps is

$$P\left(N, \frac{\ell}{\lambda}\right) = Q(0, N) = \sum_{k=0}^{N} (-1)^k \binom{N}{k} f(k)\,. \tag{A.2}$$

The formula (A.2) leaves us to determine the expression of $f(k)$, which is done as follows. When an arc, say r, is followed by a gap, we rigidly shift backward (clockwise) all the following arcs up to the last (N-th) by an amount ζ . Because the r-th arc is followed by a gap, the state of all the arcs other than r is not affected by this backward shift and we are left with a final region of size ζ that does not contain any initial position of the arcs (see Fig. A.4). Note that whether the N-th arc is gapped or ungapped before this shift corresponds to whether or not the last arc partially overlaps with the final region of size ζ. The probability of distributing $N - 1$ initial positions of the arcs (other than the first one fixed at the origin) in a region of size $1 - \zeta$ gives $f(1) = (1 - \zeta)^{N-1}$. The reasoning for $f(2)$ is similar. If the two prescribed gapped arcs are r_1 and $r_2 > r_1$, we first shift backward by ζ all the arcs following r_1 and then again by ζ those following r_2. We are then left with a final unoccupied region of size 2ζ. The crucial point is that the state of all the arcs other than r_1 and r_2 is again unaffected. We can then compute $f(2) = (1 - 2\zeta)^{N-1}$ as the probability of distributing $N - 1$ initial positions of the arcs in the available region of size $1 - 2\zeta$. Generalizing the reasoning to k arcs gives the expression $f(k) = (1 - k\zeta)^{N-1}$, provided the total length of the arcs is smaller than the

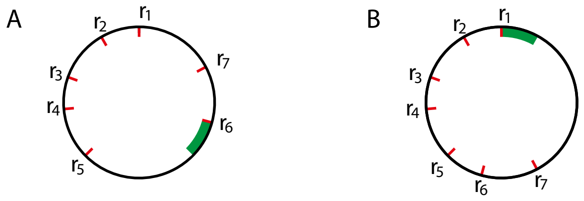

Figure A.4: Shift of the arcs following the gap affects only the covering of the arc that is followed by the gap. (**A**) Circle of unit length with seven arcs of which only the initial position has been represented (red lines at angle r_k). Each arc has length $\zeta = 1/4$ and the 5-th arc is followed by a gap (green region). (**B**) the 6-th and 7-th arc have been rotated clockwise by an angle $\pi/2$ that corresponds to an arc of length ζ. The rotation shifts the gap to the region before the first arc and does not affect the state of the 6-th and 7-th arc.

length of the circumference, i.e. $k\zeta \leq 1$, otherwise $f(k) = 0$. That completes the proof and yields Eq. (A.1).

APPENDIX B

Theory of feedback controlled brain stimulations for Parkinson's disease

B.1 Derivation of the mean field equations

In this Section we derive the mean field equations (5.7). Using the Martin-Siggia-Rose formalism [87] we write the microscopic dynamics given by equation (5.3) in a functional form

$$Z_R(x,\hat{x}) = \int \mathrm{D}h\,\mathrm{D}\hat{h}\, e^{L_0(h,\hat{h})+L_R(h,\hat{h})+J(h)+K(x,\hat{x},h,\hat{h})}\,. \tag{B.1}$$

Here, the various terms at the exponential read as follows:

$$K(x,\hat{x},h,\hat{h}) = \int \mathrm{d}t \sum_{k=1}^{N} \left(\hat{x}_k(t)h_k(t) + x_k(t)\hat{h}_k(t)\right)\,, \tag{B.2}$$

the free Lagrangian is

$$L_0(h,\hat{h}) = \int \mathrm{d}t \sum_{k=1}^{N} \left[-\frac{\Omega_k}{2}\hat{h}_k(t)\hat{h}_k(t) - i\hat{h}_k(t)\left(\tau_k \dot{h}_k(t) + h_k(t) + I_k(t)\right)\right], \tag{B.3}$$

the coupling term is

$$L_R(h,\hat{h}) = \int \mathrm{d}t \sum_{j\neq k=1}^{N} i\hat{h}_j(t)R_{jk}\phi_j(h_k(t))\,, \tag{B.4}$$

and

$$J = \frac{1}{2}\sum_{k=1}^{N}\frac{1}{\tau_k}\int \mathrm{d}t - \frac{1}{2}\int \mathrm{d}t \sum_{j=1}^{N} R_{jj}\phi_j'(h_j(t)) = \frac{1}{2}\sum_{k=1}^{N}\frac{1}{\tau_k}\int \mathrm{d}t\,. \tag{B.5}$$

The J term is due to the the Jacobian of the transformation and ensures that $Z_R(0,0) = 1$.

The average of (B.1) over the realizations of the synaptic matrix gives

$$[Z_R] = \int \mathrm{D}h\mathrm{D}\hat{h} e^{L_0+J+K} \int \mathrm{D}R \exp\left[-\frac{1}{2}\left(\sum_{j\neq k=1}^{N} \frac{(R_{jk}-\mu_{jk})^2}{\sigma_{jk}^2}\right) \right.$$
$$\left. + i\int \mathrm{d}t \sum_{j\neq k=1}^{N} \hat{h}_j(t)R_{jk}\phi_j(h_k(t))\right], \tag{B.6}$$

where

$$\mathrm{D}R = \prod_{j\neq k=1}^{N} \frac{\mathrm{d}R_{jk}}{\sqrt{2\pi\sigma_k^2}}\,. \tag{B.7}$$

Performing the Gaussian integral we obtain

$$\begin{aligned}[Z_R] = \int \mathrm{D}h\mathrm{D}\hat{h}\exp\Bigg[& L_0 + J + K + i\int \mathrm{d}t \sum_{j\neq k=1}^{N} \hat{h}_j(t)\mu_{jk}\phi_j(h_k(t)) \\ & -\frac{1}{2}\int \mathrm{d}t\mathrm{d}t' \sum_{j\neq k=1}^{N} \hat{h}_j(t)\hat{h}_j(t')\sigma_{jk}^2\phi_j(h_k(t))\phi_j(h_k(t'))\Bigg]\,. \end{aligned} \tag{B.8}$$

To perform the mean field limit of the model, the scaling with N of the connection parameters must be specified. In the neural network that we model, the connections from one nucleus to another are either excitatory or inhibitory. A necessary condition to preserve the identity of neurons is that the mean to noise ratio for individual neurons be sufficiently high, so that changes of sign are rare. In other words, we require $\sigma < |m|$ when $N \to \infty$, which leads to a scaling of the form

$$\mu = \frac{m}{N}\,, \qquad \sigma = \frac{s}{N^\beta}\,, \quad \beta \geq 1\,. \tag{B.9}$$

It follows that in the limit $N \gg 1$ the quadratic contribution to the action due to terms in $\hat{h}$ tends to vanish. This is a general property stemming from the condition $\beta \geq 1$.

The dynamics of two effective neurons is

$$\begin{aligned} \tau_S\dot{h}_S + h_S &= fm_{SS}\bar{F}_S + (1-f)m_{SG}\bar{F}_G + I_{CTX} + \eta_S\,, \\ \tau_G\dot{h}_G + h_G &= fm_{GS}\bar{F}_S + (1-f)m_{GG}\bar{F}_G + I_{STR} + \eta_G\,, \end{aligned} \tag{B.10}$$

with the self-consistency conditions

$$\bar{F}_S(t) = \langle\phi_S(h_S(t))\rangle\,, \quad \bar{F}_G(t) = \langle\phi_G(h_G(t))\rangle\,, \tag{B.11}$$

where $\langle\dots\rangle$ denotes the average over the independent Gaussian white noises η_S and η_G

$$\begin{aligned} &\langle\eta_S\rangle = \langle\eta_G\rangle = 0\,, \quad \langle\eta_S(t)\eta_S(t')\rangle = \Omega_S^2\delta(t-t')\,, \\ &\langle\eta_G(t)\eta_G(t')\rangle = \Omega_G^2\delta(t-t')\,, \quad \langle\eta_S(t)\eta_G(t')\rangle = 0\,. \end{aligned} \tag{B.12}$$

Averaging the effective neurons equations, we obtain

$$\begin{aligned} \tau_S\dot{h}_S + h_S &= fm_{SS}\bar{F}_S + (1-f)m_{SG}\bar{F}_G + I_{CTX}\,, \\ \tau_G\dot{h}_G + h_G &= fm_{GS}\bar{F}_S + (1-f)m_{GG}\bar{F}_G + I_{STR}\,. \end{aligned} \tag{B.13}$$

Since the effective potentials h_S and h_G are Gaussian processes, we have

$$\bar{F}_{S,G}(t) = \langle\phi_{S,G}(h_{S,G}(t))\rangle = \int_{-\infty}^{+\infty} \mathrm{d}z\,\phi(z)\frac{1}{\sqrt{2\pi\langle\langle h_{S,G}(t)^2\rangle\rangle}}e^{\left[-\frac{1}{2}\frac{\left(z-\bar{h}_{S,G}(t)\right)^2}{\langle\langle h_{S,G}(t)^2\rangle\rangle}\right]}\,, \tag{B.14}$$

where $\langle\langle h_{S,G}(t)^2\rangle\rangle$ denotes the variance and satisfies

$$\tau_{S,G}\frac{d}{dt}\langle\langle h^2_{S,G}(t)\rangle\rangle + 2\langle\langle h^2_{S,G}(t)\rangle\rangle = \Omega^2_{S,G}\,. \tag{B.15}$$

For times $t \gg \tau_{S,G}$, the variance $\langle\langle h^2_{S,G}(t)\rangle\rangle = \frac{\Omega^2_{S,G}}{2}$ and equations (B.13) give the mean field equations used in the main part of the text. Note finally that in random matrix theory it is common to assume $\beta = 1/2$. Such scaling leads to a chaotic regime depending on the variance σ [88]. Such a regime does not appear in our model due to the different scaling that the identity of neurons imposes.

B.2 Noise dependency of the phase diagram

As we pointed out in the main text, the microscopic derivations of the mean field equations gives an explicit dependence on the noise variance $\Omega_{S,G}$. In this Section we discuss the importance of this aspect for the network dynamics.

In the main text we remarked that, for a given value of the external currents (I_{STR}, I_{CTX}), the equilibrium behaviour of the membrane potential is given by the solution of the system $\tau_S\dot{\bar{h}}_S = \tau_G\dot{\bar{h}}_G = 0$, i.e.

$$\begin{cases} -\bar{h}_S + f m_{SS}\tilde{\phi}_S(\bar{h}_S) + (1-f)m_{SG}\tilde{\phi}_G(\bar{h}_G) + I_{CTX} & = 0\,, \\ -\bar{h}_G + f m_{GS}\tilde{\phi}_S(\bar{h}_S) + (1-f)m_{GG}\tilde{\phi}_G(\bar{h}_G) + I_{STR} & = 0\,. \end{cases} \tag{B.1}$$

The functions

$$\tilde{\phi}_{S,G}(x) = \frac{1}{\sqrt{\pi\Omega^2_{S,G}}}\int_{-\infty}^{+\infty} \mathrm{d}z\,\phi_{S,G}(z)\exp\left[-\frac{(z-x)^2}{\Omega^2_{S,G}}\right] \tag{B.2}$$

are smeared out versions of the single neuron response function that parametrically depends on the noise variance $\Omega_{S,G}$. The stability of each solution of equation (B.1) is given by the eigenvalues of the relative Jacobian matrix. Since the Jacobian matrix depends on the noise variance $\Omega_{S,G}$, the stability of the equilibrium points for a given value of the external currents (I_{STR}, I_{CTX}) does depend on the noise variance. This is explicitly confirmed by numerical simulations shown in Fig. B.1.

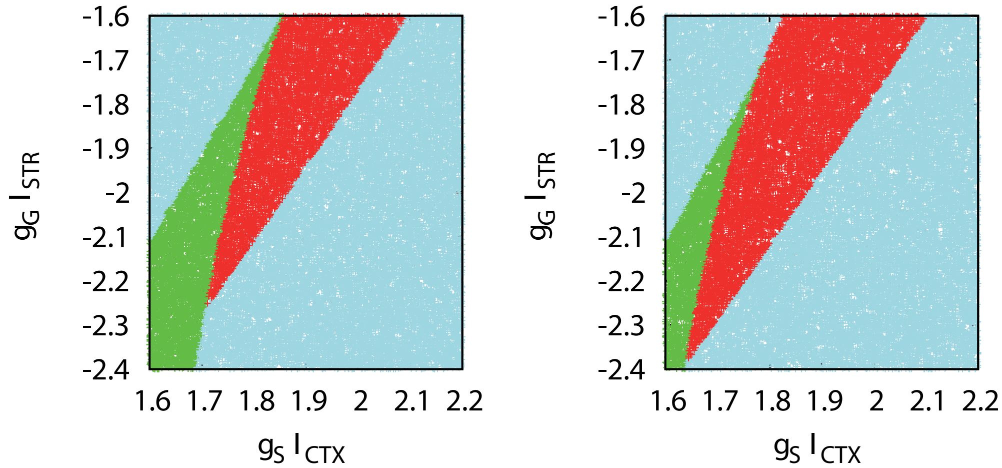

Figure B.1: Dependency of the phase diagram on the noise variance. The stability of the system is computed for the cases without noise (left) and with noise (right, $g_S\Omega_S = 0.6$) using the technique explained in Fig. 5.3. For fixed values of the external currents the noise modifies the stability of the system. Here for the case $g_S\Omega_S = 0$ ($g_S\Omega_S = 0.6$) the area covered is 54% (59%) stable, 32% (19%) bistable and 14% (22%) unstable. Hence noise increases the unstable region at the expense of the bistable region. The parameters in the simulations are as in Fig. 5.2. The colour code is: green (bistable), light blue (stable) and red (unstable).

Bibliography

[1] Victoria E Abraira and David D Ginty. The sensory neurons of touch. *Neuron*, 79(4):618–39, aug 2013.

[2] Ellen A Lumpkin, Kara L Marshall, and Aislyn M Nelson. The cell biology of touch. *The Journal of cell biology*, 191(2):237–48, oct 2010.

[3] Shana L Geffeney and Miriam B Goodman. How we feel: ion channel partnerships that detect mechanical inputs and give rise to touch and pain perception. *Neuron*, 74(4):609–19, may 2012.

[4] M. Mendelson and W. R. Loewenstein. Mechanisms of Receptor Adaptation. *Science*, 144(3618):554–555, may 1964.

[5] W R Loewenstein and M Mendelson. Components of receptor adaptation in a pacinian corpuscle. *The Journal of physiology*, 177:377–97, apr 1965.

[6] W R Loewenstein and R Skalak. Mechanical transmission in a Pacinian corpuscle. An analysis and a theory. *The Journal of physiology*, 182(2):346–78, jan 1966.

[7] Amanda Zimmerman, Ling Bai, and David D Ginty. The gentle touch receptors of mammalian skin. *Science (New York, N.Y.)*, 346(6212):950–4, nov 2014.

[8] M. B. Goodman. Mechanosensation. *WormBook*, 2006.

[9] Robert O'Hagan, Martin Chalfie, and Miriam B Goodman. The MEC-4 DEG/ENaC channel of Caenorhabditis elegans touch receptor neurons transduces mechanical signals. *Nature neuroscience*, 8(1):43–50, jan 2005.

[10] Juan G Cueva, Atticus Mulholland, and Miriam B Goodman. Nanoscale organization of the MEC-4 DEG/ENaC sensory mechanotransduction channel in Caenorhabditis elegans touch receptor neurons. *The Journal of neuroscience : the official journal of the Society for Neuroscience*, 27(51):14089–98, dec 2007.

[11] M B Goodman, D H Hall, L Avery, and S R Lockery. Active currents regulate sensitivity and dynamic range in C. elegans neurons. *Neuron*, 20(4):763–72, apr 1998.

[12] Sean M Maguire, Christopher M Clark, John Nunnari, Jennifer K Pirri, and Mark J Alkema. The C. elegans touch response facilitates escape from predacious fungi. *Current biology : CB*, 21(15):1326–30, aug 2011.

[13] Christopher J Cronin, Jane E Mendel, Saleem Mukhtar, Young-Mee Kim, Robert C Stirbl, Jehoshua Bruck, and Paul W Sternberg. An automated system for measuring parameters of nematode sinusoidal movement. *BMC genetics*, 6:5, jan 2005.

[14] Theodore H Lindsay, Tod R Thiele, and Shawn R Lockery. Optogenetic analysis of synaptic transmission in the central nervous system of the nematode Caenorhabditis elegans. *Nature communications*, 2:306, jan 2011.

[15] Christopher Fang-Yen, Matthieu Wyart, Julie Xie, Risa Kawai, Tom Kodger, Sway Chen, Quan Wen, and Aravinthan D T Samuel. Biomechanical analysis of gait adaptation in the nematode Caenorhabditis elegans. *Proceedings of the National Academy of Sciences of the United States of America*, 107(47):20323–8, nov 2010.

[16] E.M. Lifshitz L.D. Landau. *Theory of Elasticity (Volume 7 of A Course of Theoretical Physics).* Pergamon Press, 1970.

[17] T. Krauthammer E. Ventsel. *Thin Plates and Shells: Theory, Analysis and Applications*. Marcel Dekker, New York, 2001.

[18] Y. Pomeau B. Audoly. *Elasticity and Geometry*. Oxford University Press, 2010.

[19] Theriot J Phillips RB, Kondev J. *Physical Biology of the Cell*. Garland Science, New York, 2009.

[20] R. M. Christensen. *Theory of Viscoelasticity*. Dover Publications, 1971.

[21] Gutierrez-Lemini D. *Engineering Viscoelasticity*. Springer, New York, 2014.

[22] Brandon E Johnson, Austin L Brown, and Miriam B Goodman. Pressure-polishing pipettes for improved patch-clamp recording. *Journal of visualized experiments : JoVE*, (20):e964, jan 2008.

[23] Dominic Vella, Amin Ajdari, Ashkan Vaziri, and Arezki Boudaoud. The indentation of pressurized elastic shells: from polymeric capsules to yeast cells. *Journal of the Royal Society, Interface / the Royal Society*, 9(68):448–55, mar 2012.

[24] Eric D Tytell, Chia-Yu Hsu, Thelma L Williams, Avis H Cohen, and Lisa J Fauci. Interactions between internal forces, body stiffness, and fluid environment in a neuromechanical model of lamprey swimming. *Proceedings of the National Academy of Sciences of the United States of America*, 107(46):19832–7, nov 2010.

[25] Jóhanna Arnadóttir, Robert O'Hagan, Yushu Chen, Miriam B Goodman, and Martin Chalfie. The DEG/ENaC protein MEC-10 regulates the transduction channel complex in Caenorhabditis elegans touch receptor neurons. *The Journal of neuroscience : the official journal of the Society for Neuroscience*, 31(35):12695–704, aug 2011.

[26] Shana L Geffeney, Juan G Cueva, Dominique A Glauser, Joseph C Doll, Tim Hau-Chen Lee, Misty Montoya, Snetu Karania, Arman M Garakani, Beth L Pruitt, and Miriam B Goodman. DEG/ENaC but not TRP channels are the major mechano-electrical transduction channels in a C. elegans nociceptor. *Neuron*, 71(5):845–57, sep 2011.

[27] Wei Li, Lijun Kang, Beverly J Piggott, Zhaoyang Feng, and X Z Shawn Xu. The neural circuits and sensory channels mediating harsh touch sensation in Caenorhabditis elegans. *Nature communications*, 2:315, jan 2011.

[28] Zhiqiang Yan, Wei Zhang, Ye He, David Gorczyca, Yang Xiang, Li E Cheng, Shan Meltzer, Lily Yeh Jan, and Yuh Nung Jan. Drosophila NOMPC is a mechanotransduction channel subunit for gentle-touch sensation. *Nature*, 493(7431):221–5, jan 2013.

[29] Patrick Delmas, Jizhe Hao, and Lise Rodat-Despoix. Molecular mechanisms of mechanotransduction in mammalian sensory neurons. *Nature reviews. Neuroscience*, 12(3):139–53, mar 2011.

[30] Lesley Emtage, Guoqiang Gu, Erika Hartwieg, and Martin Chalfie. Extracellular proteins organize the mechanosensory channel complex in C. elegans touch receptor neurons. *Neuron*, 44(5):795–807, dec 2004.

[31] Xin Liang, Johnson Madrid, Roland Gärtner, Jean-Marc Verbavatz, Christoph Schiklenk, Michaela Wilsch-Bräuninger, Aliona Bogdanova, Florian Stenger, Axel Voigt, and Jonathon Howard. A NOMPC-dependent membrane-microtubule connector

is a candidate for the gating spring in fly mechanoreceptors. *Current biology : CB*, 23(9):755–63, may 2013.

[32] Wei Zhang, Li E Cheng, Maike Kittelmann, Jiefu Li, Maja Petkovic, Tong Cheng, Peng Jin, Zhenhao Guo, Martin C Göpfert, Lily Yeh Jan, and Yuh Nung Jan. Ankyrin Repeats Convey Force to Gate the NOMPC Mechanotransduction Channel. *Cell*, 162(6):1391–403, sep 2015.

[33] J Howard and A J Hudspeth. Compliance of the hair bundle associated with gating of mechanoelectrical transduction channels in the bullfrog's saccular hair cell. *Neuron*, 1(3):189–99, may 1988.

[34] Jessica Waguespack, Felipe T Salles, Bechara Kachar, and Anthony J Ricci. Stepwise morphological and functional maturation of mechanotransduction in rat outer hair cells. *The Journal of neuroscience : the official journal of the Society for Neuroscience*, 27(50):13890–902, dec 2007.

[35] Lorraine Pawson, Laura T Prestia, Greer K Mahoney, Burak Güçlü, Philip J Cox, and Adam K Pack. GABAergic/glutamatergic-glial/neuronal interaction contributes to rapid adaptation in pacinian corpuscles. *The Journal of neuroscience : the official journal of the Society for Neuroscience*, 29(9):2695–705, mar 2009.

[36] Samata Katta, Michael Krieg, and Miriam B Goodman. Feeling Force: Physical and Physiological Principles Enabling Sensory Mechanotransduction. *Annual review of cell and developmental biology*, 31:347–71, nov 2015.

[37] Martin Chalfie. Neurosensory mechanotransduction. *Nature reviews. Molecular cell biology*, 10(1):44–52, jan 2009.

[38] Sung-Jin Park, Miriam B Goodman, and Beth L Pruitt. Analysis of nematode mechanics by piezoresistive displacement clamp. *Proceedings of the National Academy of Sciences of the United States of America*, 104(44):17376–81, oct 2007.

[39] J. E. Harris and H. D. Crofton. Structure and function in the nematodes: Internal pressure and cuticular structure in ascaris. *Journal of Experimental Biology*, (34):116–130, 1957.

[40] Burnett DS. *Finite Element Analysis: From Concepts to Applications*. Reading MA, Addison-Wesley, 1987.

[41] Code-aster open source-general fea software.

[42] K. Johnson. *Contact Mechanics*. Cambridge University Press, 1987.

[43] M. Backholm, W. S. Ryu, and K. Dalnoki-Veress. Viscoelastic properties of the nematode caenorhabditis elegans, a self-similar, shear-thinning worm. *Proceedings of the National Academy of Sciences of the United States of America*, (110):4528–4533, 2013.

[44] W. Gilpin, S. Uppaluri, and C. P. Brangwynne. Worms under pressure: Bulk mechanical properties of c. elegans are independent of the cuticle. *Biophysical journal*, (108):1887–1898, 2015.

[45] D. Vella, A. Ajdari, A. Vaziri, and A. Boudaoud. Indentation of ellipsoidal and cylindrical elastic shells. *Physical review letters*, (109), 2012.

[46] Edward Chace Tolman. Cognitive maps in rats and men. *Psychological review*, 55(4):189–208, July 1948.

[47] J. Dostrovsky J. O'Keefe. The hippocampus as a spatial map. preliminary evidence from unit activity in the freely-moving rat. *Brain Research*, 34(1):171–175, November 1971.

[48] JS Taube, Muller RU, and Ranck JB Jr. Head-direction cells recorded from the postsubiculum in freely moving rats. i. description and quantitative analysis. *J. Neurosci.*, 10, 1990.

[49] JS Taube, RU Muller, and JB Ranck. Head-direction cells recorded from the post-subiculum in freely moving rats. ii. effects of environmental manipulations. *J. Neurosci.*, 10, 1990.

[50] Trygve Solstad, Charlotte N Boccara, Emilio Kropff, May-Britt Moser, and Edvard I Moser. Representation of geometric borders in the entorhinal cortex. *Science (New York, N.Y.)*, 322(5909):1865–8, December 2008.

[51] Speed cells in the medial entorhinal cortex. Kropff, e and carmichael, j.e.and moser m.band moser, e.i. *Nature*, 523, 2015.

[52] Torkel Hafting, Marianne Fyhn, Sturla Molden, May-Britt Moser, and Edvard I Moser. Microstructure of a spatial map in the entorhinal cortex. *Nature*, 436(7052):801–6, August 2005.

[53] Caswell Barry, Robin Hayman, Neil Burgess, and Kathryn J Jeffery. Experience-dependent rescaling of entorhinal grids. *Nature neuroscience*, 10(6):682–4, June 2007.

[54] Hanne Stensola, Tor Stensola, Trygve Solstad, Kristian Froland, May-Britt Moser, and Edvard I. Moser. The entorhinal grid map is discretized. *Nature*, 492(7427):72–78, December 2012.

[55] Edvard I Moser, Emilio Kropff, and May-britt Moser. Place cells, grid cells, and the brain's spatial representation system. *Annual review of neuroscience*, 31:69–89, January 2008.

[56] Xue-xin Wei, Jason Prentice, and Vijay Balasubramanian. A principle of economy predicts the functional architecture of grid cells. *eLife*, page e08362, 2015. Also see arXiv preprint arXiv:1304.0031 "The sense of place: grid cells in the brain and the transcendental number e".

[57] Lisa M Giocomo, Syed a Hussaini, Fan Zheng, Eric R Kandel, May-Britt Moser, and Edvard I Moser. Grid cells use HCN1 channels for spatial scaling. *Cell*, 147(5):1159–70, November 2011.

[58] David E Davis, John T Emlen, and Allen W Stokes. Studies on home range in the brown rat. *Journal of Mammalogy*, pages 207–225, 1948.

[59] Suzanne E Braun. Home range and activity patterns of the giant kangaroo rat, dipodomys ingens. *Journal of Mammalogy*, 66(1):1–12, 1985.

[60] Norman A Slade and Robert K Swihart. Home range indices for the hispid cotton rat (sigmodon hispidus) in northeastern kansas. *Journal of Mammalogy*, 64(4):580–590, 1983.

[61] W. L. Stevens. Solution to a geometrical problem in probability. *Ann. Eugenics*, 9(4):315–320, 1939.

[62] Alexander Mathis, Andreas VM Herz, and Martin Stemmler. Optimal population codes for space: Grid cells outperform place cells. *Neural Computation*, 24(9):2280–2317, 2012.

[63] Ila Rani Fiete, Yoram Burak, and Ted Brookings. What grid cells convey about rat location. *The Journal of neuroscience : the official journal of the Society for Neuroscience*, 28(27):6858–71, July 2008.

[64] Yoram Burak and Ila R Fiete. Accurate path integration in continuous attractor network models of grid cells. *PLoS computational biology*, 5(2):e1000291, February 2009.

[65] Sameet Sreenivasan and Ila R Fiete. Grid cells generate an analog error-correcting code for singularly precise neural computation. *Nature Publishing Group*, 14(10):1330–1337, 2011.

[66] Martin Stemmler, Alexander Mathis, and Andreas VM Herz. Decoding the pop-

ulation activity of grid cells for spatial localization and goal-directed navigation. *bioRxiv*, 06 2015.

[67] Kiah Hardcastle, Surya Ganguli, and Lisa M. Giocomo. Environmental boundaries as an error correction mechanism for grid cells. *Neuron*, 86(3):827–839, 2015.

[68] J. Jankovic. Parkinson's disease: clinical features and diagnosis. *Journal of Neurology, Neurosurgery & Psychiatry*, 79(4):368–376, April 2008.

[69] S.M. van Rooden, F. Colas, P. Martinez-Martin, M. Visser, D. Verbaan, J. Marinus, Kok J.N. Chaudhuri, R.K., and J.J. van Hilten. Clinical subtypes of parkinsons disease. *Mov. Disord.*, 26(51–58), 2011.

[70] R Levy, W D Hutchison, a M Lozano, and J O Dostrovsky. High-frequency synchronization of neuronal activity in the subthalamic nucleus of parkinsonian patients with limb tremor. *The Journal of neuroscience : the official journal of the Society for Neuroscience*, 20(20):7766–75, October 2000.

[71] P. Brown, A. Oliviero, and P. Mazzone. Dopamine dependency of oscillations between subthalamic nucleus and pallidum in parkinson's disease. *J. Neurosci.*, 21, 2001.

[72] M. Hariz. Twenty-five years of deep brain stimulation: celebrations and apprehensions. *Mov. Disord*, 21:930–933, 2012.

[73] Bronstein JM, Tagliati M, Alterman RL, and et al. Deep brain stimulation for parkinson disease: An expert consensus and review of key issues. *Archives of Neurology*, 68(2):165, 2011.

[74] F.M. Weaver, M. Follett, K. ans Stern, K. Hur, C. Harris, Jr. Marks, W.J., J. Rothlind, O. Sagher, D. Reda, and C.S. Moy. Csp 468 study group. bilateral deep brain stimulation vs best medical therapy for patients with advanced parkinson disease: a randomized controlled trial. *JAMA*, 301, 2009.

[75] B. Rosin, M. Slovik, R. Mitelman, and et al. Closed–loop deep brain stimulation is superior in ameliorating parkinsonism. *Neuron*, 72, 2011.

[76] S. Little, A. Pogosyan, S. Neal, and et al. Adaptive deep brain stimulation in advanced parkinson disease. *Annals of neurology*, 74, 2013.

[77] Alberto Priori, Guglielmo Foffani, Lorenzo Rossi, and Sara Marceglia. Adaptive deep brain stimulation (aDBS) controlled by local field potential oscillations. *Experimental neurology*, 245:77–86, July 2013.

[78] D Plenz and S T Kital. A basal ganglia pacemaker formed by the subthalamic nucleus and external globus pallidus. *Nature*, 400(6745):677–82, August 1999.

[79] H. Nakanishi, H. Kita, and S. Kitai. Electrical membrane properties of rat subthalamic neurons in an in vitro slice preparation. *Brain Res.*, 437, 1987.

[80] A. Nambu and R. Llinas. Electrophysiology of globus pallidus neurons in vitro. *J. Neurophysiol.*, 72, 1994.

[81] H. Kita, H. Chang, and S. Kitai. The morphology of intracellularly labeled rat subthalamic neurons: a light microscope analysis. *J. Comp. Neurol.*, 215, 1983.

[82] S. Afsharpour. Light microscopic analysis of golgi-impregnated rat subthalamic neurons. *J. Comp. Neurol.*, 236, 1985.

[83] Andrew Gillies, David Willshaw, and Zhaoping Li. Subthalamic-pallidal interactions are critical in determining normal and abnormal functioning of the basal ganglia. *Proceedings. Biological sciences / The Royal Society*, 269(1491):545–51, March 2002.

[84] Andrew Gillies and David Willshaw. Models of the subthalamic nucleus. The importance of intranuclear connectivity. *Medical engineering & physics*, 26(9):723–32, November 2004.

[85] Julien Modolo, J Henry, and Anne Beuter. Dynamics of the subthalamo-pallidal complex in Parkinson's disease during deep brain stimulation. *Journal of biological physics*, 34(3-4):251–66, August 2008.

[86] S. Strogatz. *Nonlinear Dynamics and Chaos (with applications to physics, biology, chemistry and engineering).* Perseus Books, 2006.

[87] P. Martin, E. Siggia, and H. Rose. Statistical dynamics of classical systems. *Phys. Rev. A*, 8, 1973.

[88] H. Sompolinsky, A. Crisanti, and H. Sommers. Chaos in random neural networks. *Phys. Rev. Lett.*, 61, 1988.